RESONANCE-BASED MEMS TEMPERATURE SENSORS FOR TEMPERATURE COMPENSATION OF MEMS CAPACITIVE ACCELEROMETER

A THESIS SUBMITTED TO
THE GRADUATE SCHOOL OF NATURAL AND APPLIED SCIENCES
OF
MIDDLE EAST TECHNICAL UNIVERSITY

BY

GÜLŞAH DEMİRHAN

IN PARTIAL FULFILLMENT OF THE REQUIREMENTS
FOR
THE DEGREE OF MASTER OF SCIENCE
IN
ELECTRICAL AND ELECTRONICS ENGINEERING

FEBRUARY 2016

Approval of the thesis:

RESONANCE-BASED MEMS TEMPERATURE SENSORS FOR TEMPERATURE COMPENSATION OF MEMS CAPACITIVE ACCELEROMETER

submitted by **GÜLŞAH DEMİRHAN** in partial fulfillment of the requirements for the degree of **Master of Science in Electrical and Electronics Engineering Department**, **Middle East Technical University** by,

Prof. Dr. Gülbin Dural Ünver _____
Dean, Graduate School of **Natural and Applied Sciences**

Prof. Dr. Gönül Turhan Sayan _____
Head of Department, **Electrical and Electronics Eng.**

Prof. Dr. Tayfun Akın _____
Supervisor, **Electrical and Electronics Eng. Dept., METU**

Examining Committee Members

Prof. Dr. Tayfun Akın _____
Electrical and Electronics Eng. Dept., METU

Prof. Dr. Cengiz Beşikçi _____
Electrical and Electronics Eng. Dept., METU

Prof. Dr. Abdülkadir Erden _____
Mechatronics Eng. Dept., Atılım University

Prof. Dr. Haluk Külah _____
Electrical and Electronics Eng. Dept., METU

Assist. Prof. Dr. Kıvanç Azgın _____
Mechanical Eng. Dept., METU

Date:

I hereby declare that all information in this document has been obtained and presented in accordance with academic rules and ethical conduct. I also declare that, as required by these rules and conduct, I have fully cited and referenced all referenced material and results that are not original to this work.

Name, Surname: Gülşah Demirhan

Signature:

ABSTRACT

RESONANCE-BASED MEMS TEMPERATURE SENSORS FOR TEMPERATURE COMPENSATION OF MEMS CAPACITIVE ACCELEROMETER

Demirhan, Gülşah

M.S., Department of Electrical and Electronics Engineering

Supervisor: Prof. Dr. Tayfun Akın

February 2016, 127 pages

Micro-Electro-Mechanical Systems (MEMS) having capacitive sensing mechanism have been gaining interest as a result of low-cost, small-size, and high-reliability sensors applications. Today micromachined capacitive sensors can be found in different places and various areas ranging from military to industrial applications such as inertial navigation, vibration monitoring, and robotics control. On the other hand, MEMS accelerometers have some drawbacks that restrict them for use in applications that require inertial grade accuracy. One of the most significant disadvantages is the drift in the output of the chip. The drift is caused by many reasons including internal (physical structure, alignment, material type etc.) and external (time, atmospheric pressure, acceleration and temperature) effects. In this thesis, a closed-loop MEMS resonator is designed and fabricated with its readout electronics to compensate the temperature effects of used MEMS capacitive accelerometer. The idea of the proposed study is using the resonator structure as a temperature sensor together with controller circuitry. That is to say, the study consists of two branches; one is PI controller output which would be used as a temperature sensor and the other is preamplifier output which would be used as carrier generator to the accelerometer readout circuitry.

The proposed resonator is analyzed in detail in terms of dynamics, simulation models and theoretical investigations. The implemented resonator is shown to satisfy the estimated performance parameters with measurements conducted using various test setups. The functionality of concept is verified with additional tests. In other words, it is gathered repeatable temperature sensitivity data from both the accelerometer and the resonating temperature sensor. Then, initially the temperature sensitivity of the accelerometer output with the controller output of the resonating accelerometer is compensated. Once the attempt in the first step is succeed, the temperature compensation network is disassembled and the resonator output to the accelerometer package as the carrier signal is fed. This eliminates the need for an external carrier waveform generated by a standard clock generator, which can be one of the dominant noise sources injected into the accelerometer system. After this new interconnection is made, the temperature sensitivity of the accelerometer is measured. By doing that, it is aimed to observe that the temperature sensitivity of the accelerometer is the same as before compensation, while it is driven by the resonator output as the carrier signal. Finally, the compensation network will be re-assembled while still feeding the accelerometer with the output of the resonator, and it is tried to repeat the compensated accelerometer response that was previously observed at the first step.

The best system level test results showed that the temperature sensitivity is improved from -32 mg/°C to -1.6 μg/°C for -35 μg/$\sqrt{Hz}$ noise floor, 16 μg bias instability and 122 dB dynamic range.

Keywords: MEMS resonator, temperature sensor, MEMS capacitive accelerometer, temperature compensation.

ÖZ

MEMS KAPASİTİF İVMEÖLÇERLERİN SICAKLIK DUYARLILIĞININ DÜZELTİLMESİ İÇİN REZONANS TABANLI MEMS SICAKLIK DUYARGALARI

Demirhan, Gülşah

Yüksek Lisans, Elektrik ve Elektronik Mühendisliği Bölümü

Tez Yöneticisi: Prof.Dr. Tayfun Akın

Şubat 2016, 127 sayfa

Kapasitif algılama mekanizmasına sahip olan Mikro-Elektro-Mekanik Sistemler (MEMS) uygulamaları son zamanlarda düşük maliyet, küçük boyut ve yüksek güvenilirlik sonucunda ilgi kazanmaktadır. Bugün mikroişlenmiş kapasitif sensörler birçok askeri, ataletsel navigasyon, titreşim izleme ve robotik kontrolü gibi endüstriyel uygulamalara kadar pek çok alanda ve farklı yerlerde bulabilirsiniz. Öte yandan, MEMS ivmeölçerler atalet dereceli doğruluk gerektiren uygulamalarda kullanım için bazı dezavantajlara sahiptir. En önemli dezavantajlardan biri çip çıktı sürüklenmesidir. Sürüklenmeye dahili (fiziksel yapısı, uyum, malzeme türü vb) ve harici (zaman, atmosferik basınç, ivme ve sıcaklık) etkiler neden olmaktadır. Bu tezde, MEMS kapasitif ivmeölçerin sıcaklık etkilerini telafi etmek için kapalı bir döngüde MEMS rezonatör sensörü elektronik okuma devresi ile birlikte tasarlanmış, üretilmiş ve kullanılmıştır. Önerilen çalışma fikrinde, kontrol devresi ile birlikte rezonatör yapısı bir sıcaklık sensörü olarak kullanmaktadır. Bu çalışma iki bölümden oluşmaktadır; birinci kısımda, rezonatör sıcaklık sensörü olarak kullanılacak ve ikinci kısımda rezonatörün PI denetleyici çıkışı ivmeölçer okuma devresine taşıyıcı üretecektir.

Önerilen rezonatör dinamikleri, simülasyon modelleri ve teorik araştırmalar açısından ayrıntılı olarak incelenmiştir. Uygulanan rezonatör çeşitli test kurulumları kullanılarak yapılan ölçümler ile tahmin edilen performans parametreleri karşılaştırılmıştır. Kavramın işlevselliği ilave testler ile doğrulanmıştır. Kısaca ivmeölçer ve rezonatör olarak tasarlanan sıcaklık sensörü için tekrarlanabilir sıcaklık hassasiyeti verileri toplanmıştır. Ardından, başlangıçta ivmeölçer çıkışının sıcaklık hassasiyeti, rezonatörün kontrolcü çıkışı ile telafi edilmiştir. Birinci aşama girişimi başarılı olduktan sonra, sıcaklık dengeleme ağı sökülmüş ve rezonatör çıktısı ivmeölçer paketine taşıyıcı sinyal olarak beslenmiştir. Bu, ivmeölçer sistemi içine zerkedilmiş başlıca gürültü kaynaklarından biri olabilen standart saat üreteçinin ürettiği dışsal taşıyıcı dalgaformu ihtiyacını ortadan kaldırmıştır. Bu yeni arabağlantı yapıldıktan sonra, ivmeölçer sıcaklık hassasiyeti ölçülmüştür. Böylece, o taşıyıcı sinyali olarak rezonatör çıkışı ile yönetilen ivmeölçer sıcaklık hassasiyetinin daha önce olduğu gibi aynı kaldığını gözlemlemek amaçlanmıştır. Son olarak, ivmeölçer yeniden monte edilerek hala rezonatör çıkışı ile beslenirken ve daha önceki testlerde gözlenen kompanse edilmiş ivmeölçer yanıtı tekrarlanmaya çalışılmıştır.

Elde edilen en iyi sistem seviye sonuçlar gösterir ki -35 µg/$\sqrt{Hz}$ gürültü seviyesi, 16 µg kayma kararsızlığı ve 122 dB dinamik aralık için sıcaklık hassasiyeti -32 mg/°C den -1.6 µg/°C ye iyileştirilmiştir.

Anahtar Kelimeler: MEMS rezonatör, sıcaklık sensörü, MEMS kapasitif ivmeölçer, sıcaklık duyarlılığının azaltılması.

To Mustafa Kemal ATATÜRK

ACKNOWLEDGEMENTS

I would like thank to my supervisor, Prof. Dr. Tayfun Akın for his support, guidance, encouragement and understanding.

I wish all the best and thank to my thesis committee members Prof. Dr. Abdülkadir Erden, Prof. Dr. Haluk Külah, Prof. Dr. Cengiz Beşikçi and Assist. Prof. Dr. Kıvanç Azgın, as well as Prof. Dr. Tayfun Akın, for their valuable discussions and feedback.

I am very thankful to Dr. Said Emre Alper for his valuable contributions and advices. His support and leadership shows a positive attitude and lead my motivation to the success of this study.

I am also very thankful to Dr. M. Mert Torunbalcı for his valuable contributions and advices in every aspect of the life. His support shows a positive attitude on every part of my life. I am very lucky to have such a best friend.I am glad to my colleagues who helped me during my studies even most hopeless times and I am especially very thankful to Yunus Terzioğlu, Hasan Doğan Gavcar, Ferhat Yeşil, Ulaş Aykutlu and Talha Köse for their unique contributions on the development of MEMS resonators as a temperature sensor and readout electronics studies. I would like to thank to every member of METU-MEMS Centre family specially Evren Erdil, Eyüp Can Demir, Oğuzhan Temel, Eren Canga, Başak Kebabçı, Ozan Ertürk, Dr. Özgecan Dervişoğlu, Ebru Uğur Arslan, Evrim Özçakır, Dr. Akın Aydemir, Fatih Aykut Bakırcı, Ali Aytekin, Levent Abat, Taylan Toral, Dr. Ebru Sağıroğlu Topallı, Osman Aydın, Selçuk Keskin, Ahmet Murat Yağcı, Dr. Mustafa Yıldırım, Adem Saraç, Ramazan Çetin, Utku Göreke for a stimulating and fun environment.

And above all, I would like to thank my lovely family members, Beyhan, Anıl Zülfü and Ali Asker Demirhan for everything.

TABLE OF CONTENTS

ABSTRACT v

ÖZ…… vii

ACKNOWLEDGEMENTS x

TABLE OF CONTENTS xi

LIST OF FIGURES xv

FIGURES xv

LIST OF TABLES xxi

CHAPTERS

1 INTRODUCTION 1

1.1 MEMS Accelerometers 3

1.2 Detailed Problem Description 4

1.2.1 Structural Errors 5

1.2.2 External Errors 6

1.3 Temperature Effects on Capacitive MEMS Accelerometers 7

1.4 Literature Review 10

1.5 Motivation of This Thesis and Research Objectives 17

1.6 Organization of Thesis 18

2 RESONATOR THEORY AND MODELING 19

2.1 Dynamics of Resonators 19

2.2 Resonator Design 21

2.2.1 Mechanical Spring Design and Spring Constant Calculation 22

2.2.2 Estimating Mass and Damping Factor 22

2.2.3 Electrostatic Actuation Mechanisms 23
2.2.4 Capacitive Sensing Approach 26
2.3 Micro-Resonators Developed in This Study 28
2.3.1 Analytical Modelling Theory 29
2.3.2 Single Mass H-Shaped Resonators 31
2.3.3 Tuning Fork Resonators 35
2.4 Finite Element Simulations 39
2.5 Implementation of Single Mass and Tuning Fork Type Resonators in the Same Die 52
2.6 Summary 53
3 FABRICATION OF MEMS RESONATORS USING ADVANCED MEMS (*aMEMS*) PROCESS 55
3.1 Fabrication of Sensor Wafer Applying Modified Silicon-On-Glass (M-SOG) Process 56
3.2 Wafer Level Packaging of MEMS Sensor Wafers with SOI Cap Wafers 62
3.3 Fabrication Results 65
3.4 Summary of the Chapter 69
4 READOUT ELECTRONICS FOR MEMS RESONATOR SENSORS 71
4.1 Read-out Electronics 71
4.2 Read-out Controller Design for MEMS Resonators 72
4.2.1 Modulator 73
4.2.2 Low-Pass Filter 73
4.2.3. PI Controller 74
4.3 Open Loop and Close Loop Characteristics of MEMS Resonators 74
4.4 Closed Loop Resonator Simulink Model for Control Electronics 79
4.5 Integration of MEMS Resonator Sensors with Readout Electronics 81

4.6 Summary 85
5 COLLECTED DATA AND TEST RESULTS 87
5.1 Data Collection Methodologies 87
5.1.1 Range of Temperature 88
5.1.2 Acceleration Range 88
5.1.3 Test Duration 88
5.1.4 Number of Samples 88
5.2 Used Techniques for Compensation of Temperature and Acceleration Effects 89
5.2.1 Moving Average Filter 89
5.2.2 Polynomial Curve Fitting 90
5.2.3 Observation of Hysteresis 91
5.2.4 Integration of Compensation by Applying Polynomial Curve Fitting. 93
5.3 MEMS Resonator Sensors Used in the Study and Their Results 94
5.3.1 Functionality Tests of the Designed Resonator Packages 94
5.3.2 Resonance Tests 95
5.3.3 Resonance frequency vs temperature test results: 97
5.3.4 Closed Loop Temperature versus Controller Output Tests with Front End Electronics 101
5.3.5 White Noise Calculation of Functional Resonator Packages 104
5.4 MEMS Accelerometer Sensor Used in the Study and Its Results 106
5.4.1 Characterization of MEMS Accelerometer Sensor 107
5.4.2 Hybrid-Package Preparation, Test PCB and Functionality Tests 108
5.4.3 Temperature Tests of Accelerometer Package 110
5.5 Implementation of Test Setup for the System Level Tests and Results 112

5.5.1 Temperature Compensation of Accelerometer Output by Using Resonator's PI Controller Output Data 114

5.6 Summary 117

6 CONCLUSIONS AND FUTURE WORK 119

REFERENCES 123

LIST OF FIGURES

FIGURES

Figure 1.1: Forecast about the delivery of commercial Micro-electro mechanical systems (MEMS) products in the market in 2012 – 2018 [6]. 2
Figure 1.2: The image showing the raw data converted to filtered data by applying moving average filter method for 5 minutes sampling at 250 Hz. 15
Figure 2.1: A simple micromechanical resonant device where *k* is spring constant, *m* represents proof mass, *c* refers to damping coefficient, and *x* refers the displacement. 19
Figure 2.2: A simple image representing electrostatic actuation mechanism with varying gap approach [40]. 23
Figure 2.3: A simple image representing electrostatic actuation mechanism with the comb drive approach [40]. 25
Figure 2.4: Schematic view of the resonator test setup [40]. 27
Figure 2.5: Picture of the layout of the designed varying overlap type single mass H-shaped resonator with 15 kHz resonance frequency (Design-1) and 45 kHz resonance frequency (Design-2) for temperature compensation. 32
Figure 2.6: Picture of the layout of the designed varying gap type single mass H-shaped resonator with 15 kHz resonance frequency (Design-3) and 45 kHz resonance frequency (Design-4) for temperature compensation. 34
Figure 2.7: Picture of the layout of the designed tuning fork varying overlap type resonator with 15 kHz resonance frequency (Design-5) and 45 kHz resonance frequency (Design-6) for temperature compensation. 36
Figure 2.8: Picture of the layout of the designed tuning fork varying gap type resonator with 15 kHz resonance frequency (Design-7) and 45 kHz resonance frequency (Design-8) for temperature compensation. 38

Figure 2.9: Mode shape simulations of varying overlap area type single mass H-shaped resonator (Design-1): (a) 1st mode: 15.1 kHz, (b) 2nd mode: 53.4 kHz, (c) 3rd mode: 55.8 kHz. 41
Figure 2.10: Mode shape simulations of varying gap area type single mass H-shaped resonator (Design-3): (a) 1st mode: 15.86 kHz, (b) 2nd mode: 50.5 kHz, (c) 3rd mode: 55.8 kHz. 42
Figure 2.11: Mode shape simulations of varying overlap area type single mass H-shaped resonator with the resonance frequency of 45 kHz (Design-2): (a) 1st mode: 42.5 kHz, (b) 2nd mode: 72.3 kHz, (c) 3rd mode: 72.7 kHz. 44
Figure 2.12: Mode shape simulation results of varying gap area type single mass H-shaped resonator with the resonance frequency of 45 kHz (Design-4): (a) 1st mode: 41.5 kHz, (b) 2nd mode: 70 kHz, (c) 3rd mode: 72.3 kHz. 45
Figure 2.13: Mode shape simulation results of varying overlap area type tuning fork resonator (Design-5): (a) 1st mode: 6.5 kHz, (b) 2nd mode: 15 kHz, (c) 3rd mode: 30.2 kHz. 47
Figure 2.14: Mode shape simulation results of 15 kHz varying gap area type tuning fork resonator (Design-7): (a) 1st mode: 6 kHz, (b) 2nd mode: 14.5 kHz, (c) 3rd mode: 30.7 kHz. 48
Figure 2.15: Mode shape simulation results of varying overlap area type tuning fork resonator of the resonance frequency nearly 45 kHz (Design-6): (a) 1st mode: 28.3 kHz, (b) 2nd mode: 45.8 kHz, (c) 3rd mode: 74.5 kHz. 50
Figure 2.16: Mode shape simulation results of varying gap area type tuning fork resonator of nearly 45 kHz (Design-8): (a) 1st mode: 27 kHz, (b) 2nd mode: 44 kHz, (c) 3rd mode: 71.4 kHz. 51
Figure 2.17: The packaged layout of a die including TF and single mass varying overlap and varying gap type resonators. 52
Figure 3.1: Process grades of the glass wafer with the modified SOG process. 58
Figure 3.2: Process path of the SOI sensor wafer with the modified SOG process... 59
Figure 3.3: (continued) 60
Figure 3.4: After the anodic bonding of glass and SOI substrates. 61
Figure 3.5: Fabricated uncapped resonator sensor wafer with the modified SOG process. 61

Figure 3.6: Fabrication steps of packaged resonator. 62
Figure 3.7: (continued) 63
Figure 3.8: (continued) 64
Figure 3.9: SEM pictures of (a) close-up view of folded spring type for Design-1, (b) close-up view of folded spring type for Design-2, and (c) general view of designed springs after the fabrication. 66
Figure 3.10: SEM pictures of different type of fingers (a) close-up view of Design-3, (b) general view of Design-3, (c) general view of Design-1, and (d) close-up view of Design-1 after the fabrication. 67
Figure 3.11: SEM picture of the fabricated sensors (a) Design-3, (b) Design-1, (c) Design-7, (d) Design-6 (e) general view of fabricated sensors in the same die. 68
Figure 3.12: SEM picture of the encapsulated die presenting the details of vertical feedthroughs and via openings [40]. 69
Figure 4.1: "Schematic of the trans-impedance amplifier implemented in this work." [50]. 72
Figure 4.2: The circuit diagram of the modulator used in the thesis [52]. 73
Figure 4.3: The circuit diagram of the PI Controller [52]. 74
Figure 4.4: Simplified block diagram of the resonance test schematic. 75
Figure 4.5: The scheme representing the block diagram of the closed loop resonator controller circuitry. 78
Figure 4.6: The closed loop resonator's step response controller and carrier signal obtained using the realistic SIMULINK model of the resonator control electronics. 80
Figure 4.7: SIMULINK model of the closed loop control electronics for the resonator of Design-5. 80
Figure 4.8: The image of the constructed Spice model for readout electronics simulations of resonator designs. 82
Figure 4.9: The image of the designed glass substrate PCB layout by using L-Edit software, representing the places of the wire bonding (green lines). 83
Figure 4.10: The picture of the fabricated glass substrates with all the components attached to 16-pin package. 84
Figure 4.11: The image of the circuit board prepared for the resonator temperature tests including resonator Design-1 package. 84

Figure 5.1: The raw data collected from both the temperature sensor and controller output of the resonator Design-5. 89
Figure 5.2: The digitally filtered and scaled temperature and controller output data collected from resonator Design-5 plotted over a 2-hour long period. 90
Figure 5.3: The graph showing the Design-8 (0602 ID, 50 kHz tuning fork varying gap type) resonator sensor's polynomial curve fitting temperature versus controller output result. Higher the accuracy of curve fitting, higher the degree of polynomial and designer can decide the accuracy and speed. 91
Figure 5.4: The turn on bias is changed when each time a sensor is started up, whereas the relation between the temperature and the resonator's controller output remains constant. 91
Figure 5.5: The comparison of heating up and cooling down characteristics of the sampling conditions of 100 Hz 2 hours. 92
Figure 5.6: The comparison of cooling down and heating up characteristics of the sampling conditions of 250 Hz 5 minutes for each points. 93
Figure 5.7: The picture showing the resonance test result of the Design-4 (1106 ID, varying gap type sensor in Table 5.1). 96
Figure 5.8: The Tenney Oven in which all the tests are conducted with data acquisition interface, placement of the MEMS sensor inside the temperature controlled oven and control module for controlling the test conditions. 98
Figure 5.9: The image showing the wires which contain the data come out of the hole which is placed left side of the oven and these wires are connected to the computers and power supplies. 99
Figure 5.10: The resonance frequency versus temperature graph results of the Hot Plate and the Tenney Oven for resonator Design-5. For these tests average TCF value is calculated on the hot plate with narrow range as -128 ppm/K. The average TCF value is calculated on the Tenney with broader range as -114 ppm/K. 101
Figure 5.11: The test results of resonator package including Design-7 with its readout circuitry put into the Tenney Oven: (a) Design-7 resonator controller output and TMP-36 sensor output changes at the same plot for 45-minutes data collection; (b) Design-7 resonator controller output vs TMP36 sensors output results in the range minus 20°C to +80°C for different day tests with the same conditions. 103

Figure 5.12: The performance of the resonator Design-7 with temperature range from -20°C to +80°C with an ideal line fit. 104
Figure 5.13: The sample Alavar output for Design-1; 15 kHz varying overlap type resonator sensors and these output is given for 75000 data collected from DAQ. .. 105
Figure 5.14: The C-V characterization results of ACCE sensor which is showing the functional responce: (a) The positive electrode measurement as it can be analyzed the smooth curve and parasitic capacitance of positive electrode (PE) is measured as 109.718 fF; (b)The negative electrode measurement as it can be analyzed from the smooth curve and changes are in logical manner and parasitic capacitance of negative electrode (NE) is measured as 49.795 fF. 107
Figure 5.15: The final view of the prepared AFFRO v1.2 accelerometer package including ACCE sensor..... 109
Figure 5.16: The ACCE single axis accelerometer sensor with the combination of AFFRO v1.2 readout circuitry to perform functionality tests..... 109
Figure 5.17: The ACCE single axis accelerometer sensor output results with temperature change from -20°C to +80°C for collected data set green color represents TMP36 temperature sensor output and blue color represents accelerometer output. 110
Figure 5.18: The ACCE single axis accelerometer sensor output results with temperature change for different test conditions. Set1 is detailed as from -20°C to +80°C with oven open; Set 2 is detailed as from +80°C to room temperature with oven closed; Set 3 is detailed as from -20°C to +80°C with oven open; Set 4 is detailed as from +80°C to room temperature with oven closed; and finally Set 5 is detailed as from -20°C to room temperature with oven closed. 111
Figure 5.19: The performance of the accelerometer sensor with temperature range from -20°C to +80°C including an ideal line fit. 112
Figure 5.20: The image representing (a) The Tenney Oven in which the system level tests are conducted with data acquisition interface and control module for controlling the test conditions, (b) closure view of the placement of the MEMS sensors inside the chamber……113

Figure 5.21: The relation between resonator controller output and accelerometer output including the test duration inside the temperature oven with the range -20°C to +80°C……115
Figure 5.22: Temperature compensation plot of the MEMS accelerometer including both compensated and uncompensated outputs with line fit equations……115
Figure 5.23: Allan deviation plots for the accelerometer used in the scope of thesis study……..117

LIST OF TABLES

TABLES

Table 2.1: Tabulated form of the 8 different resonator design characteristics in the scope of this study. 29
Table 2.2: Design parameters of varying overlap area type single mass H-shaped resonator Design-1 and Design-2. 33
Table 2.3: Design parameters of varying gap area type single mass H-shaped resonator Design-3 and Design-4. 35
Table 2.4: Design parameters of tuning fork varying overlap area type resonator Design-5 and Design-6. 37
Table 2.5: Design parameters of tuning fork varying gap area type resonator Design-7 and Design-8. 39
Table 2.6: Comparison of mode shape simulation results for varying gap and overlap type single mass H-shaped resonators with the resonance frequency of 15 kHz. 40
Table 2.7: Comparison of mode shape simulation results for varying overlap (Design-2) and varying gap (Design-4) and type single mass H-shaped resonators with the resonance frequency of 45 kHz. 43
Table 2.8: Comparison of mode shape simulation results for varying overlap type (Design-5) and varying gap (Design-7) tuning fork (TF) resonators with the resonance frequency of 15 kHz. 46
Table 2.9: Comparison of mode shape simulation results for varying overlap (Design-6) and varying gap (Design-8) type tuning fork (TF) resonators with the resonance frequency of 45 kHz. 49
Table 4.1: The model parameters of the Design-1 type resonator used during the one of the design of the closed loop controller for 10 V_{PM} 79
Table 4.2: The necessary controller values of the resonators for temperature sensing of accelerometers: 81

Table 5.1: The resonance test results of the designed resonators for temperature sensing of accelerometers: 96
Table 5.2: The resonance test results of the Design-5 (ID#1112) resonator with front end electronics for temperature sensing of accelerometers with temperature variations: (Notice tests are constructed at 5Hz span, 1mV peak voltage and 5 second of integration and settling time)..... 97
Table 5.3: The resonance test results of the Design-5 (ID#1112) type resonator with front end electronics for temperature sensing of accelerometers with temperature variations on Tenney Oven: (Notice tests are constructed at 5Hz span, 1mV peak voltage and 5 second of integration and settling time)..... 100
Table 5.4: The tabulated form of the functional sensors' scale factor, random walk and white noise values: 105
Table 5.5: Features of the ACCE accelerometer sensor package. 106
Table 5.6: The comparison results of the ACCE sensor obtained from two different tests in this study……...116

CHAPTER 1

INTRODUCTION

Micro-electro-mechanical systems (MEMS) are defined as the synergistic integration of mechanical and electrical components. The development of the transducers, sensors, and actuators; which are used in various usages such as consumer electronic market towards the automotive and even military electronic products improved with the help of MEMS [1]. The first MEMS technology improvement which have stress-sensitive effects in silicon and germanium termed piezoresistance developed in 1954 [2]. In 1960s Honeywell Research Centre and Bell Lab for the first time introduced the silicon diaphragm pressure sensor and strain gauges. From 1960s to 1970s commercialized pressure sensors and non-planar geometric pressure sensors took place in MEMS market [3]. During the half century, MEMS improved itself in terms of the batch fabrication methods which end with miniaturization of the chips. MEMS devices consist of accelerometers, gyroscopes, microphones, strain gauges, pressure and flow sensor and all have some properties ranging from small to rugged and low-cost [4, 5].

"Today, the MEMS market reaches over 10 Billion dollars per year and estimated to be grown from $12 billion to over $24 billion by 2019" [6]. Figure 1.1 represents the forecast about the delivery of MEMS devices in the market in between 2012 and 2018.

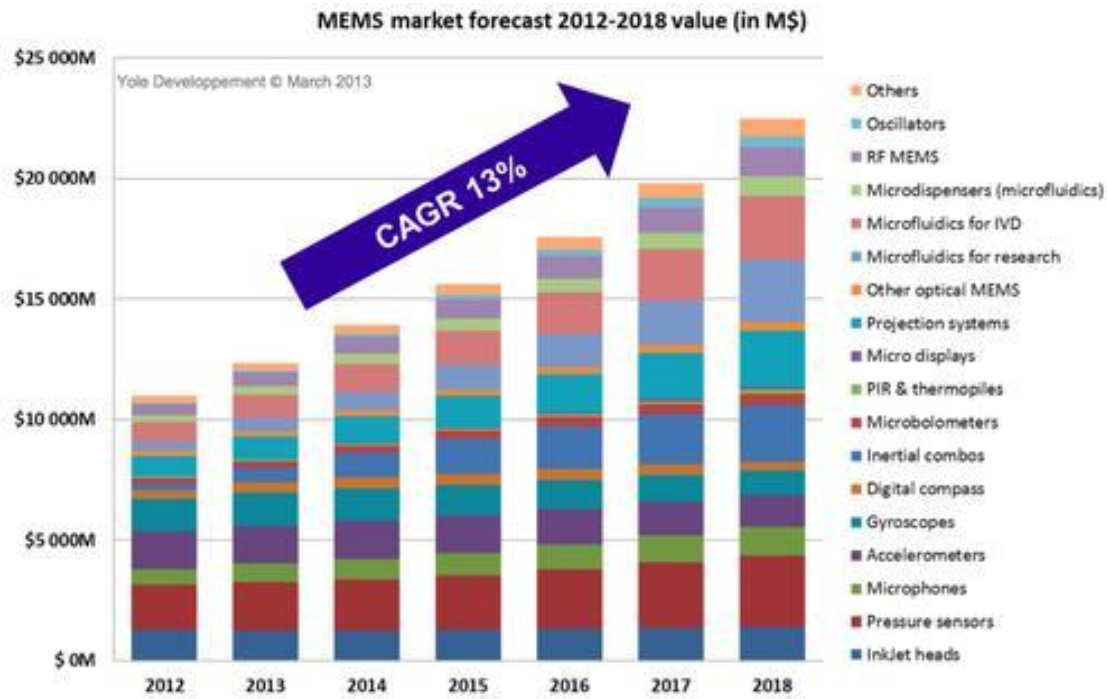

Figure 1.1: Forecast about the delivery of commercial Micro-electro mechanical systems (MEMS) products in the market in 2012 – 2018 [6].

"The importance of MEMS is evident from the fact that so much research is being done in miniaturization of devices, and MEMS is used to replace the conventional bulkier devices. One of the devices, where MEMS started to replace the conventional bulkier devices is accelerometers." [7].

It would be better to mention some application areas and benefits of MEMS accelerometers in order to understand the motivation of this study fully. Understanding the significance of MEMS products and their usage area in various sectors show how the performance requirements of these devices improve is going to verify clearly.

The aim of the study is to improve the micro-machined devices specialized as MEMS capacitive accelerometer chips. The MEMS capacitive accelerometer output is affected adversely by the environmental factors ranging from vibration to temperature. The scope of this work is to overcome drift in a MEMS capacitive accelerometer output data caused by the temperature related variations. Polynomial curve fitting method is used in this study for analog capacitive accelerometers. After presenting

some background knowledge about MEMS accelerometers the research objectives of the study are listed.

The organization of this section is as follows; Section 1.1 introduces briefly MEMS accelerometers in terms of classification, advantages and drawbacks. Section 1.2 provides the detailed problem description. Section 1.3 presents the states of art studies in literature for temperature compensation. Section 1.4 and 1.5 give the motivation of this thesis; research objectives and thesis organization, respectively.

1.1 MEMS Accelerometers

During the late 1940s and 1950s, the piezoelectric accelerometers are grown up. Brüel & Kjær (Denmark), Columbia Research Laboratories (Woodlyn, PA), Endevco (Pasadena, CA), Gulton Manufacturing (Metuchen, NJ), and Kistler Instruments (Buffalo, NY) were pioneering companies [8]. Micro-fabrication techniques ranging from the anisotropic chemical etching of silicon to the bonding techniques developed during the 1960s based on the development of the performance of MEMS products. The first MEMS piezoresistive accelerometer was developed by Roylance and Angell [2]. In this study the accelerometer was fully packed for protecting the whole structure from environmental effects [2]. Then, commercialized piezoresistive accelerometer was presented by Barth et al., in which the silicon fusion bonding technique was applied as the first time. Recent improvements come out of by combination of piezoresistive accelerometer with CMOS including temperature compensation circuitries. “A novel piezoresistive accelerometer was introduced by Allen where in-plane and out-of-plane acceleration measured with the help of a specially designed vertical spring structure.” [2].

Since 1987, MEMS completed the previous stage of technology development and it transferred to the mature stage including the batch production [9]. Nowadays, the capacitive transduction is popular like piezoresistive transduction. As a result, CMOS integrated circuits are used for the amplification and the compensation purposes by either monolithic or hybrid approach.

The MEMS accelerometers are classified by relying on the transduction mechanisms. “The major transduction mechanisms of MEMS accelerometer are listed as capacitive,

piezoresistive, tunneling, resonant and thermal." [10]. For this work, capacitive sensing type MEMS accelerometers are preferred. The working principle of capacitive sensing is like that if there is an external acceleration, the defined mass changes its stationary position to opposite direction of acceleration and the capacitive fingers' gap distances vary which leads to capacitance. The capacitance change is measured by using electronic circuitry. Capacitive sensing transduction method is one of the most common sensing methods among MEMS sensors due to robustness and compatibility with various processes. The main advantage of capacitive systems is the simplicity of mechanism. Also, the capacitive interfaces have high range of application areas including low-cost, low power detection, and high precision inertial devices. Moreover, a lot of benefits are supplied like high sensitivity, good DC response, noise performance, low drift, and low temperature sensitivity; even though the capacitive systems are in lack of electromagnetic interference (EMI) due to high impedance sense nodes. It can be concluded that, it is significant to develop convenient encapsulation technology and shield the accelerometer with its interface circuitry [10].

MEMS products in terms of accelerometers provide some advantages such as lower cost, better compatibility with mass fabrication, smaller space requirement, and higher reliability.

On the other hand, MEMS accelerometers include some disadvantages that restrict them for inertial grade accuracy applications. One of the most significant disadvantages is the drift in the output of the chip. The drift is caused by many reasons including internal and external effects. Notice that although some of the effects are based on the limitations of currently available fabrication process whereas the others are environment related; so they can be improved. All in all, the drifts in capacitive MEMS accelerometer output causes difficulty to be used in navigational applications.

1.2 Detailed Problem Description

The MEMS accelerometer g output's drift is due to many factors which consists both internal structure based errors and external effects to a sensor. The MEMS accelerometers have various types and all have changeable responses and characteristics depending on the design types accordingly.

This part discusses the sources of errors mainly caused by without giving a specific accelerometer designs. The given error sources are taken from the literature. The scope of the work is mainly overcoming the drift error taken from experimental data rather than the theory of the error sources. It is significant to determine the source that causes error in MEMS accelerometers; in terms of operation principles and how they cause the errors.

The error source consists of two classes named structural and environmental [11]. The structural errors are classified as mechanical error, damping effect, and drive mode errors. Similarly, the environment dependent defects are classified as temperature, pressure, linear acceleration, vibration or any other external stimulus that can degrade the behavior of a MEMS accelerometer.

1.2.1 Structural Errors

Because of either the material properties or the used fabrication technology, the structural error sources are essential in a sensor. In process steps there are some limitations, and for that reason the fabrication could not do much for the surface of the sensor. The minimum feature size required by the design is defined as the critical dimension. Besides, the minimum detectable feature size which could be measured repeatedly by any process is defined as resolution.

1.2.1.1 Mechanical Error

Generally, MEMS accelerometers are based on the spring-mass damper equation. The transduction mechanism of resonant type working principles is relied on controlling the resonance frequency which is changing with acceleration of sensors. The working principle is based on the stiffness of springs vibrating about rest position to amount of applied rotation. The spring production is critical and never unique, and imparting non-diagonal stiffness coefficient; which leads to transfer to other orthogonal axis in the existence of applied force. According to literature search it can be concluded that by carefully designing MEMS accelerometers mechanical errors could be reduced [11].

1.2.1.2 Damping Error

Damping error significantly relies on the shape of the spring preferred in a chip, and could be monitored by redesigning the spring dimensions. According to literature

survey this error is not very important, and does not add major error among other factors [11].

1.2.2 External Errors

There are many factors affecting the output of a MEMS accelerometer ranging from temperature to pressure and vibration. However, in the scope of this study just temperature is focused on. The temperature of the MEMS resonator and the MEMS accelerometer changes depending on the environmental conditions. Also, there are other random noises observed in an accelerometer output because of high frequency components that are normally Gaussian in nature and easier to deal. “The noise is classified in two main categories namely deterministic and random.” [12].

1.2.2.1 Deterministic Noise

In this noise type either the data is provided by the manufacturer or sensor is calibrated. The calibration results are problematic due to misalignment in the structure of a sensor [7]. Deterministic noise can be classified with two sub-headings as “bias offset” and “scale factors”.

Bias Offset

This error is basically the subtraction of the desired output value from actual output achieved by a chip. The bias offset is a type of built-in error for MEMS accelerometer sensors which occurs due to fabrication imperfections, mechanical misalignment, or design faults.

Scale Factors

Scale factor is used if the analog sensor voltage is converted to a digital one. Needless to say, the resulting noise is due to quantization of the analog voltage.

1.2.2.2 Random Noise

Although it is possible to predict the deterministic or systematic noise, differently random noise is not be able to desire beforehand, while acquisition of data from a chip. The modelling this random noise in terms of separating the data from this noise is problematic. The theme of compensation is actually understanding this noise and

removing it from sensor data [7]. The random noise can be divided in two categories called high frequency noise and low frequency noise [12].

Noise of High Frequency

This noise is varying very quickly at high frequency. “The most common techniques to remove this type of noise is using low pass filter, wavelet decomposition, moving average filter, median filter or back propagation neural networks.” [12]. Averaging could be preferred to eliminate this noise at significant level.

Noise of Low Frequency

Low frequency noise or long term noise appears gradually with time. This is a co-related noise which has relation with other parameters like change in temperature [12].

1.3 Temperature Effects on Capacitive MEMS Accelerometers

One of the most significant factors that affect the MEMS accelerometer output is the variations in the defined environment temperature. The observations show that all MEMS sensors affected by the variation in temperature. Therefore, the output of the sensor also includes an error.

It is really significant to know how the temperature causes change in the MEMS accelerometer sensor. Fluctuation in the environment temperature causes change in the physical properties of the material that constructs the MEMS structure. It is expected that there may be lots of items that are affected by the temperature change upon a specific design of a chip. Many characteristics ranging from effects on resonant frequency, quality factor to output of MEMS accelerometer, expansion of materials and heating by the sensor packaging; which can be thought common to working principle of all MEMS accelerometer sensors are detailed under this heading.

1.3.1 Temperature Effect on Resonant Frequency

The definition of the Modulus of Elasticity *(E)* of a material is obtained by dividing the stress *(σ)* to strain *(ε)*. Equation 1.2 gives the mathematical expression of modulus of elasticity.

$$E = {}^{\sigma}/_{\varepsilon} \qquad 1.2$$

Similarly, Equation 1.3 represents the expression between modulus of elasticity of a material and its temperature *(T)* [13].

$$E = K_E T E_0 \qquad 1.3$$

where K_E refers to temperature coefficient of silicon material and E_0 refers to temperature coefficient of monocrystalline silicon. Equation 1.4 shows the expression between the resonant frequency *(w)* and the other parameters that in turn is dependent on the variations in temperature [13]. In the Equation 1.4, *W* refers to the stability index, *h* and *L* represents the dimensions of the beam, *A* is the area and *m* refers to the mass of the structure.

$$\mathrm{w} = \sqrt{(4EhW^3 + \pi AL^2\sigma/4) \,/\, (mL^3)} \qquad 1.4$$

As it can be understood from the above discussions the resonant frequency, residual stress and strain are affected from temperature variations.

1.3.2 Effect of Temperature on Q-Factor

"Quality factor is one of the most important parameters; the accuracy and good quality of a resonator is really significant since it further determines the output of a MEMS accelerometer." [14]. The mathematical representation of quality factor is presented in the Equation 1.5.

$$Q = \frac{Total\ Energy}{Energy\ Lost\ in\ One\ Cycle} \qquad 1.5$$

The energy loss is affected by three effects named gas damping, anchor losses and intrinsic losses; respectively. "Gas damping is caused by the air present inside a sensor package and results in loss of energy in a resonator. Anchor loss is caused due to

coupling of resonators with surrounding materials like packaging or substrate. In intrinsic losses, energy is lost due to material properties such as viscosity." [14].

In micro type resonators the most significant factor for energy loss is gas damping and Equation 1.6 represents the expression for quality factor *(Q)* [13].

$$Q = \frac{h\rho wo}{4}\sqrt{\frac{\pi}{2}}\sqrt{\frac{RC}{MT}} \qquad 1.6$$

For the Equation 1.6, quality factor is represented by *Q*, *w* refers to resonance frequency, *ρ* is the density and *h* is the thickness of electrode, C/*R* are molar constants, *M* is mass of gas in moles and *T* is the temperature of a chip.

1.3.3 Temperature Effects on MEMS Resonator's Controller and Accelerometer Outputs

The amplitude of the driving mode of the resonator is relatively dependent on the resonating frequency of resonators. As detailed in the test results chapter, the relation between Q-factor and temperature data are collected from Desing-1 (15 kHz single mass H-shaped varying overlap) type resonators shows that resonance frequency decreases like linearly when temperature is increased. So, the amplitude of the resonator's controller output is affected by the temperature of its material.

1.3.4 Material Expansions

If the temperature of the material which constructs the MEMS accelerometer or resonator varies, it directly results variations in the physical properties of the material. The output voltage (V_o) consists of the multiplication of the input voltage (V_{in}) and fraction of change in capacitance [15]. The mathematical representation for the above definition is given in the Equation 1.7.

$$Vo = \left(\frac{\Delta C}{A}\right) * V_{in} \qquad 1.7$$

In the Equation 1.7, *A* represents the scale factor, ΔC refers to total change in capacitance because of variation in the electrode gap and V_{in} depicts the input voltage.

The ΔC is determined either by variation in the gap between electrodes or by variation in the overlap surface area. It can be concluded that the output of MEMS accelerometer changes indirectly by the expansion of material due to the fact that temperature change causes expansion in the material structure which is the bone for MEMS accelerometer.

1.3.5 Heat of the Sensor Package

Covers or sensor packages are one of the most significant factors that determine the environment temperature inside a chip. Clearly, the heat dissipation amount by a chip directly related with the package selection, and could end in different amount of offset connected to the MEMS accelerometer output. By the selection of convenient package for MEMS accelerometer, the amount of drift added to a sensor because of packaging could be monitored if the heating source is just the sensor itself.

1.4 Literature Review

In the literature review part, the techniques which are preferred in the compensation of temperature are mentioned. The section starts with the literature review of resonators because in the scope of this study designed resonators are used as temperature sensors for compensation of MEMS capacitive accelerometers and then methods of temperature compensation in MEMS structures are given.

1.4.1 Resonators Used as a Temperature Sensor in the Literature

In [16], Si micromechanical resonators have a quality factor and a resonance frequency which is strongly temperature dependent. Si resonating structures' frequency based temperature sensitivity is nearly -30 ppm/ºC or approximately 4000 ppm over a -40 to 85 ºC operating range. On the other hand, quartz is approximately 0.04 ppm in the same temperature range. The resonator quality factor could be thought as an ideal temperature sensor which supplies no additional power, has no time delay and indicates the temperature of the resonator directly. For the study of [16], the resonating structures are packaged in a low pressure for eliminating damping, the turning fork design is selected for minimizing anchor losses. The loss from TED is major and controls the resonator's quality factor and strongly the material properties of the Si beam in terms of thermal expansion, density, heat capacity and thermal conductivity

dependent. In temperature sensing applications, preference is to apply a low-pass filter to the chip signal in order to prevent the effect of noise.

In [17], authors mentioned that the resonance frequency of tuning fork is inversely proportional with size. The temperature drift and fabrication offsets are compensated with a phase locked loop. Electromechanical coupling needs to convert excitation voltage into force; and converts mechanical displacement into signal current. There are 5 different transduction methods. Capacitive transduction is based on electrostatic force and conversion of charge; well suited for micromachining; widely used in MEMS gyroscopes and accelerometers. Piezoelectric transduction used in nearly all commercial devices among the magnetic transduction, piezoresistive sensing, and thermal actuation.

In [18], authors discussed the most significant aspects in terms of resonating material, process technology, type of resonator, mode of vibration, quality of vibration and temperature stability such as a resonating chip is a device with an element vibrating at resonance which varies resonator's output frequency. Single-crystal materials have excellent resonating properties in terms of very high intrinsic Q-factors compared with polycrystalline silicon. Q factor is one of the very significant parameter which affects the stability and the resolution and depends on different damping mechanisms such as imbalances, viscous and acoustic radiation losses.

In terms of design considerations, the vibrating element must have a sufficient input parameter selectivity and sensitivity of the resonance frequency. Increased structure stiffness increases the resonance frequency whereas the temperature sensitivity of the resonance frequency should be low. Mode coupling is a problem, which may arise when the resonator is operated in a closed-loop configuration, and it is best avoided by selecting a mode and design with as few and weak resonance frequencies as possible in the vicinity of the wanted mode. There are basically 4 dominant parameters (the resonator material, vibration mode, thermal expansion coefficient mismatch, excitation and detection types) that affect the sensor temperature sensitivity of the resonance frequency.

“It is the direct coupling between the high mechanical quality of silicon and the resonance vibration of an element that makes it possible to make stable, high resolution and high sensitivity resonant silicon sensors.” [18].

In [19], the design, fabrication, and characterization of temperature sensitive quartz resonators processed using heterogeneous integration techniques for realizing high density, thermal conductance fluctuation limited thermal sensors for infrared imaging and biochemical sensing applications are introduced. In this study, “241 MHz micromachined resonators from Y cut quartz crystal cuts were produced with a temperature sensitivity of 22.162 kHz/°C.”

In [20], authors introduce a new compensation method suitable for micro resonators operated in a closed loop. The method relies on the controlled modulation of the mechanical stiffness of the resonators preferring an additional feedback loop and can be used to compensate for temperature induced frequency drift. In their study they used disk resonator. This study has some advantages. First of all, only an additional feedback loop is required and therefore is adaptable to any resonant sensors featuring excitation and detection elements without structural modifications. Secondly, the temperature-induced frequency drift can be compensated without interrupting a sensor operation. Thirdly, the relative quality factor change of the resonator is extracted via a precise and simple frequency measurement. Finally, the temperature dependences of the excitation and detection elements do not affect the precision.

1.4.2 Methods for Temperature Compensation of a MEMS Structures

There are mainly two methods for achieving thermal compensation; by circuitry design in terms of hardware or by processing the data, after acquisition from a chip output. In comparison, the processing of the data is slower than the hardware compensation. On the other hand, in some cases it is impossible to use the hardware compensation, and the signal processing is the just one applicable option. Although the designer has the opportunity to make changes in the circuitry which eliminates for drifts imparted to the chip by temperature results; due to the lack of many design considerations and sensors internal characteristics it is not always possible. In such cases the temperature

compensation is just possible by processing the data coming from the sensor output. As a first step hardware compensation is considered [7].

1.4.2.1 Temperature Compensation by Hardware Design

In the hardware design concepts, there are different ways to compensate the drift mainly caused by the temperature.

Using Temperature Control Device

In [13], the over correction of temperature could be obtained by introducing a temperature control device. The functionality of the developed system is to adjust the temperature of a chip at an optimal value of temperature. A thermo-electric cooler is applied for temperature variation of a chip and the temperature feedback is preferred as input to the cooler maintaining the temperature at a previously defined grade. By using this method temperature is compensated without applying any change in the actual circuitry of a chip. "The advantage is that the chip circuitry and temperature circuitry could be designed separately, which leads ease and flexibility in the design." [7].

Controlling the Oscillators Using PTAT

Alternatively, the effects of temperature could be compensated by preferring this technique. Zhang et. al. [21] integrated an on-chip circuitry which utilizes PTAT (Proportional to Absolute Temperature) current to overcome for the temperature drift. "This current controls oscillators, and lag in the frequency of oscillators due to rise in temperature is compensated by the PTAT current and is valid for a wide range of temperature." [21]. It is obviously understood that, any property of the circuitry which is linearly dependent on the temperature could be preferred as a feedback to the chip circuitry.

Similarly, in [22], authors present a resonating structure with self-temperature sensing technique applying a pair of harmonically related c-modes in a dual c-mode oscillator. In this study 1st order temperature coefficient is -96.3 ppm/ºC and range is from -60 ppm/ºC to 150 ppm/ºC. In [23], the study shows that thermoelastic damping is important in MEMS resonant sensors and it is also an important loss mechanism. Finally, in [24], authors measure the temperature performance of the 480µmx120µm

block resonating structure operating at the 66,7MHz mode in the range of 20-100ºC; and the TCF is -40 ppm/ºC.

Applying Temperature Variable Gain Circuitry

CTAT current refers to Complementary to Absolute Temperature current and could be applied for overcoming of temperature drift in MEMS capacitive sensors. "A linear relation is found between CTAT current and temperature change in a gyroscope thus paving the way for temperature calibration." [25]. "Yin et. al. preferred a capacitive MEMS gyroscope for eliminating temperature drift by making design changes in the readout circuitry applying CTAT." [7].

Applying Frequency Synthesizer for Core Temperature

The resonance frequency of a motor mode depends on the temperature of a resonating structure [13, 27]. "The difference between the resonance frequencies of two oscillators that have different oscillation coefficients could be applied to analyze the temperature at which they are oscillating." [28]. Chiu et. al. modified this property in order to read the exact core temperature of a MEMS structure. In [28] the temperature compensation is obtained by using FPGA based frequency synthesizer. "The difference in the frequencies monitors the core temperature of the sensor, and hence is used to declare the defects of temperature." [28].

In the scope of this thesis study just temperature compensation by signal processing is selected; so there is no selection between any of the above mentioned hardware techniques because in this study real-time temperature compensation is not intended; so they are just given for information.

1.4.2.2 Temperature Compensation by Signal Processing

This method is convenient when there is no way to apply hardware changes. The methods under signal processing are detailed in the following paragraphs.

Applying Kalman Filter Method

In [12, 29, and 30], for the drift compensation Kalman filter is used in real time. In [31, 32], Kalman filter is used for temperature compensation technique. In the study of [31], two step methods are used for compensation as a first step temperature compensation is performed by different techniques and then Kalman filter is used. The

working principle of Kalman filtering is as the predictor is processing the data and eliminating the jumps and noise, and tries to maintain on the actual data path; which is the error to be compensated itself.

Applying Moving Average Filter Method

The high frequency noise in the data is filtered by applying the moving average method and notice that it is not just for temperature compensation. Figure 1.2 represents the high frequency noise can be filtered from the raw data to achieve the characteristics of the data in the scope of this study in terms of temperature output for 5 minutes sampling rate at 250 Hz frequency.

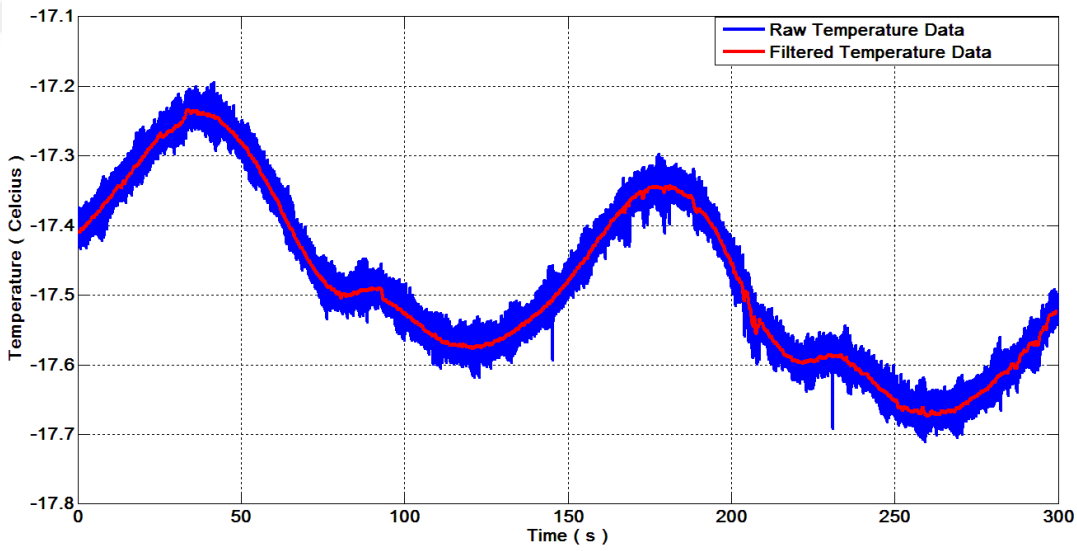

Figure 1.2: The image showing the raw data converted to filtered data by applying moving average filter method for 5 minutes sampling at 250 Hz.

Notice that for this study the moving average filter method is applied in each analysis since the high frequency noise makes impossible to analyze the characteristics of data in the raw form. Last but not least, in the hysteresis analyses it is required to get very fine plots and it is not possible without this method.

Applying Wavelet Decomposition

"The wavelet decomposition technique is applied for extracting information from a noisy or high frequency data." [29]. It is a one of the powerful techniques to process

information about low frequency pattern of any data. In [29], authors applied this method to extract the drift trend and use data itself as a drift model. Due to the four step filtering named as median filter, wavelet decomposition, autoregressive modeling and Kalman filtering, this process is difficult and simpler other techniques are selected for use in real time applications.

Applying Polynomial Curve Fitting (CF)

Polynomial Curve Fitting is one of the most applicable methods preferred for temperature compensation [13, 31, 33 and 34]. In [31], they "reported 16 times improvement in the bias instability (27°/sec to 1.4°/sec) by using CF for temperature compensation and Kalman filtering for other factors." In [34], comparison of CF and other methods evident that CF is inferior to compensation by neural network.

In this work, polynomial curve fitting is selected because of the simplicity and easy processing.

Applying Linear Curves

This method is the derived form of the polynomial CF method. It is useful when the system is higher order and nonlinear. The complex characteristics of polynomials could be decreased by dividing the temperature range regions to first order multiple polynomials rather than the one high order polynomial [13]. By doing this difficulty of the system is eliminated and system gets linear.

Applying Back Propagation (BP) Neural Networks (NN)

Another commonly applied technique for temperature compensation is using back propagation neural networks method [13, 33 and 34]. In [33], it is mentioned that "neural networks could be applied for temperature compensation and the results of compensation are comparable to the results achieved by CF method." In other words, NN can be used alternatively for temperature compensation issues.

Applying Temperature Coefficient of Resonance Frequency

The resonance frequency of a material in a MEMS structure is depend on the temperature [27, 35]. If designer prefers to use resonant frequency coefficient in the structure which is linearly changing with the variation in the temperature then temperature compensation can be obtained by basically using that coefficient. On the

other hand, this method has its limitations in terms of choice of materials and convenient environment of a sensor.

1.5 Motivation of This Thesis and Research Objectives

In all MEMS structures ranging from gyroscopes to accelerometers, the drift in the output of a sensor prevents the usage in inertial grades and unfortunately the other goods are compensated by this effect. Although the structural errors are mostly fabrication limited and are inevitable; environmental and other parameters caused errors on the other hand, can be compensated by applying some signal processing methodologies. By doing this, MEMS structures become more accurate to be used for navigational applications.

One of the most important factors that cause the MEMS output device to drift with time is the variation in temperature of a sensor [36, 37]. MEMS systems in terms of resonating structures require mechanical movement for the operation and the heating causes changes in the output of a sensor. Similar to MEMS structures in the literatures, the used accelerometer sensors designed and fabricated at METU MEMS Center also affected by temperature, and to solve the problem different types of silicon resonators are designed and fabricated. The scope of this study is the elimination of temperature effects by monitoring the actuation voltage of the resonator's PI controller output; also, using the resonator's resonance frequency and amplitude for accelerometer circuitry for carrier generation purposes. By doing this self-oscillatory resonating structure is obtained and it will be integrated to any MEMS sensor; for these study capacitive MEMS accelerometers is specified.

To summarize, the main idea of this master thesis is using the resonator structure as a temperature sensor together with controller circuitry. That is to say, this study consists of two branches; one is PI controller output which would be used as a temperature sensor and the other is preamplifier output which would generate carrier and that would be feed to the accelerometer readout circuitry so need for function generator (external source) for carrier generation purposes are eliminated.

Notice that this study emphasizes the how overcoming of effects and drifts caused by temperature in the output of a MEMS accelerometer. The research objectives of this study are both design and fabrication of the different actuation mechanisms for low and high resonance frequencies as a temperature sensor; and also, carrier generation and feed part to analog accelerometer package.

1.6 Organization of Thesis

The organization of this section is like that, Chapter 1 supports the detailed knowledge of compensation requirements, literature review, detailed problem review and why capacitive MEMS accelerometers are used.

Chapter 2 gives the details of resonator sensor design; which consists of the resonator dynamics, formulations, design criterions and FEM simulations.

Chapter 3 summarizes the fabrication details. This chapter includes the fabrication and wafer level packaging steps of the chip based on the advanced MEMS process and the fabrication results are discussed in terms of the comparison of the designed and measured parameters of the resonators.

Chapter 4 mentions the design of controller electronics for MEMS resonators for the temperature compensation ranging from describing the front end electronics, presenting each blocks one by one, including the SIMULINK model and simulation results to giving tabulated form of the PI controller values for all 8 different resonator designs and describing the glass substrates which is designed to integrate the resonators with the readout electronics.

Chapter 5 provides the data and results that are obtained after implementing the temperature compensation for every sensor including all the study achieved and done step by step ranging from functionality test to block tests and compensation procedures.

Chapter 6 summarizes the results and provides conclusions to this study and mentioning the future work that could be done.

CHAPTER 2

RESONATOR THEORY AND MODELING

This section provides the resonator dynamics and express the theoretical model of the resonators worked in this thesis. Section 2.1 begins with the dynamics of resonator. Section 2.2 explains the resonator designs in terms of spring, mass, damping factor calculation, electrostatic actuation, and capacitive sensing. Section 2.3 shows micro-resonators developed in the scope of this work. The verification of mechanical and electrical parameters is carried out in finite element modelling (FEM) simulations in Section 2.4. Section 2.5 explains the implementation of single mass and tuning fork type resonators in the same die. As a final step, Section 2.6 summarizes the chapter.

2.1 Dynamics of Resonators

A simple micromechanical resonator device consists of mass-spring and damper. Figure 2.1 shows a simple micromechanical resonant device where *k* is spring constant, *m* represents proof mass, *c* refers to damping coefficient, and *x* is the displacement.

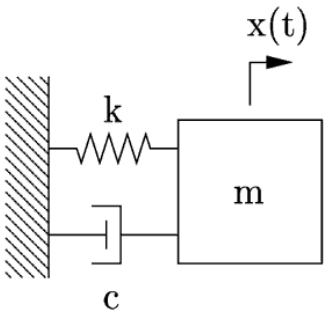

Figure 2.1: A simple micromechanical resonant device where *k* is spring constant, *m* represents proof mass, *c* refers to damping coefficient, and *x* refers the displacement.

In the case, mass is moved by an external force, micromechanical resonator has a resonance frequency where it oscillates and this resonant frequency could be defined as in the Equation 2.1 where *k* represents spring constant and *m* represents the mass.

$$f_r = \frac{1}{2\pi}\sqrt{\frac{k}{m}} \qquad 2.1$$

Micromechanical resonators can be described by using second degree differential equations as in the Equation 2.2; *F* represents the force acting on the system, *x* is defined as the displacement, *k* refers to spring constant, *m* is proof mass, *c* is damping coefficient, and *t* is time.

$$F = m\frac{\partial^2 x}{\partial t^2} + c\frac{\partial x}{\partial t} + kx \qquad 2.2$$

By converting this expression to the frequency domain by using Laplace conversion (Equation 2.3); the applied force and the deflection in terms of the mechanical system parameters and the frequency of the applied force (*w*) can be expressed. By modifying the terms used in the Equation 2.2 under resonance condition; the Equation 2.4 is obtained.

$$F = ms^2X(s) + csX(s) + kX(s) \qquad 2.3$$

$$\frac{X(s)}{F(s)} = \frac{1/m}{s^2 + \frac{wr}{Q}s + wr^2} \qquad 2.4$$

In the Equation 2.4, w_r is the resonant frequency and *Q* refers to the quality factor of the micromechanical resonator. The Equation 2.5 expresses the resonance frequency of a micromachined resonator. Similarly, the Equation 2.6 shows the quality factor of the resonator.

$$w_r = \sqrt{\frac{k}{m}} \qquad 2.5$$

$$Q = \frac{k}{c.w_r} \qquad 2.6$$

If an external force monitors the system at the resonance frequency, the amplitude of the displacement changes fast. The Equation 2.7 depicts the maximum deflection of a MEMS resonator with minimum actuation force. The quality factor (Q) changes with the damping factor (c) that relies on the environment pressure.

$$\frac{X(jw)}{F(jw)} = \frac{1}{j}.\frac{Q}{k} \qquad 2.7$$

As a result, if the resonator is driven at its mechanical resonance frequency, it obtains maximum energy efficiency with minimum actuation force [38]. Therefore, designed resonator structures in the scope of this study are based on these dynamics.

2.2 Resonator Design

MEMS resonator design has some requirements both in mechanical and electrical domain. The mechanical design consists of damping factor, spring constant and mass calculation although the electrical design includes electrostatic actuation mechanism. The analysis of the system is then verified in finite element modelling (FEM) simulations.

Mechanical modelling variables ought to be identified to analysis the mode dynamics of the designed resonators. Fundamentally, analyzed variables are the spring constant, mass and damping factors that are discussed in the Sections 2.2.1 and 2.2.2, respectively.

Electrical modelling of the resonator consists of the electrostatic actuation and capacitive transduction, which are discussed in the Sections 2.2.3 and 2.2.4, respectively.

2.2.1 Mechanical Spring Design and Spring Constant Calculation

The most significant design parameter of the resonating structure is the resonant frequency that exactly depends on the spring constant and mass of the mechanism. That is to say, mechanical spring constants are the major design parameters for determination of the drive mode resonant frequencies. In the scope of this thesis, half and double folded springs are preferred. The advantages of these spring types are providing large displacement without affecting the linearity. The descriptive analysis on the design and spring constant calculations of the half and double folded springs could be found in [38].

2.2.2 Estimating Mass and Damping Factor

Another important mechanical model variable is mass estimation of the non-fixed parts of the system. The mass of the moving parts could be found by applying the simple formula in the Equation 2.8 where ρ is the mass density of the structural material and V is the volume.

$$m = \rho V \qquad 2.8$$

"On the other hand, a fraction of the spring masses ought to be also added to this equation according to Rayleigh energy method to estimate the effective masses for the resonant frequency estimation." [38].

Damping could be described as the dissipation of vibration energy. Four main damping systems in the resonating structures could be listed as air damping, thermo-elastic damping, anchor, and electronic damping. Although, the major damping mechanism at the atmosphere is the air damping; under vacuum, the effect of air damping decreases and other damping sources start major. It is not easy to estimate the damping

factor since it relates with many factors and requires a complex analysis for which descriptive analyses on the damping sources could be found in [38, 40].

2.2.3 Electrostatic Actuation Mechanisms

The working principle is basically that an electrostatic force is generated by a parallel plate capacitor; which consists of two conductive plates and separated with an insulator. With the existence of different bias potentials to the movable and stationary parts of this capacitor, energy is stored because of the charge accumulation between the parallel plates. The stored energy is converted to a current through the displacement. Electrostatic actuation mechanisms could be characterized in two main groups; varying gap and varying overlap area; respectively.

2.2.3.1 Varying Gap

The working principles of varying gap structures are based on the electrostatic actuation that occurs by varying the gap of the capacitor on a fixed overlap area. In other words, the movement is generated along the direction where the gap between the parallel plates decreases while the anti-gap increases. Figure 2.2 represents the electrostatic actuation mechanism with varying gap approach.

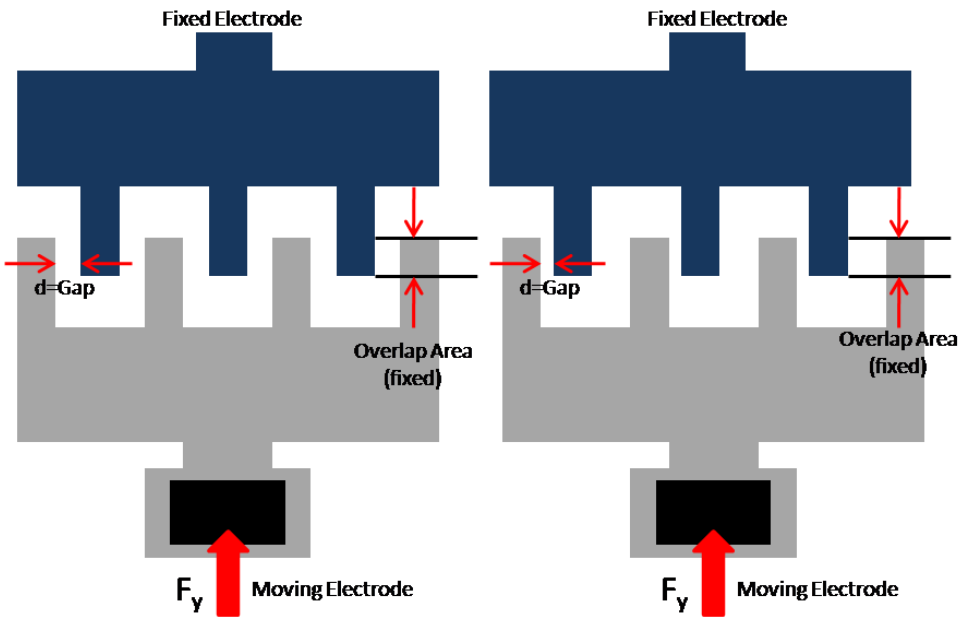

Figure 2.2: A simple image representing electrostatic actuation mechanism with varying gap approach [40].

For this approach, the energy stored for a given voltage (*V*) and the capacitance (*C*) is expressed by the Equation 2.9.

$$W = \frac{1}{2} C V^2 \qquad 2.9$$

Capacitance and overlap area are defined as;

$$C = \mathcal{E}_0 . \mathcal{E}_r . \frac{A}{d} \qquad 2.10$$

$$A = \ell . t \qquad 2.11$$

If *C* is placed into the Equation 2.9, stored energy is found as;

$$W = \frac{\mathcal{E}_0 . \mathcal{E}_r . \ell . t . V^2}{2d} \qquad 2.12$$

The force occurring between the parallel plates could be defined as in the Equation 2.16 where *N* represents the number of comb-drive capacitors, *V* depicts the applied potential, $\mathcal{E}_0$ refers to the permittivity of free air, *t* shows the thickness of comb-drive structures, and *l* is the overlap area. In varying gap type approach higher capacitance sensitivity is provided for detecting small displacements, however, it has non-linear characteristics as can be observed in the Equation 2.16.

$$Fy = \frac{\partial W}{\partial z} = \frac{1}{2} V^2 . \frac{\partial C}{\partial z} \qquad 2.13$$

$$Fy = \frac{1}{2} V^2 . \frac{\partial \frac{(\mathcal{E}_0 . \mathcal{E}_r . \ell . t)}{(d+z)}}{\partial z} \qquad 2.14$$

$$Fy = -\frac{1}{2} . \frac{\mathcal{E}_0 . \mathcal{E}_r . \ell . t . V^2}{(d+z)^2} \qquad 2.15$$

$$Fy = -\frac{1}{2}N\mathcal{E}_0.\mathcal{E}_r.\ell.t.V^2\left(\frac{1}{(d_{gap}-z)^2}-\frac{1}{(d_{antigap}+z)^2}\right) \qquad 2.16$$

Above equations proves that $\frac{\partial C}{\partial z}$ is nonlinear and depends on the voltage and the gap. Therefore, only small displacements are provided with this configuration. Notice in the Equation 2.16, d_{gap} and $d_{antigap}$ refer to gap separation and anti-gap separation; respectively.

2.3.3.2 Varying Overlap Area

The second group consists of the structures with the working principle of electrostatic actuation occurring by varying the overlap area of the capacitor while fixing the capacitive gap. Another name for varying overlap area approach is comb drive. This alternative type of electrostatic actuator consists of many fingers which are actuated by applying a voltage between them. In this configuration, the movement is in the lateral direction and the capacitance changes with the variation of the area of overlap with fixed gap spacing. Figure 2.3 illustrates the electrostatic actuation mechanism with comb-drive approach.

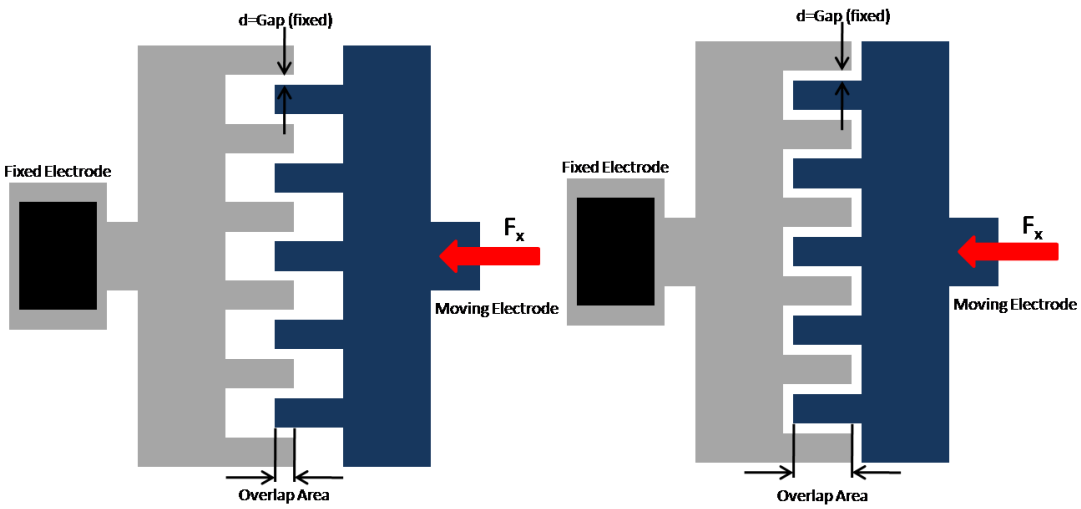

Figure 2.3: A simple image representing electrostatic actuation mechanism with the comb drive approach [40].

The force between the parallel plates could be defined as in the Equation 2.17 where *N* represents the number of comb-drive capacitors; *V* refers to the applied potential, $\mathcal{E}_0$ shows the permittivity of free air, *t* depicts the thickness of comb-drive structures, and *d* refers to the capacitive gap. Force between the plates is expressed by the Equation 2.20.

$$F = \frac{\partial W}{\partial x} = \frac{1}{2}.V^2\frac{\partial C}{\partial x} \qquad 2.17$$

$$C = \frac{\mathcal{E}_0.\mathcal{E}_{r.}t.(\ell + x)}{d} \qquad 2.18$$

$$F = \frac{1}{2}V^2.\frac{\partial(\frac{\mathcal{E}_0.\mathcal{E}_r.t.(\ell + x)}{d})}{\partial x} \qquad 2.19$$

$$F = \frac{1}{2}NV^2.\mathcal{E}_0.\mathcal{E}_r.\frac{t}{d} \qquad 2.20$$

Having solved the equations above, it is seen that $\frac{\partial C}{\partial x}$ is linear and independent from overlap area. Thus, large displacements are obtained in this type of electrostatic actuation.

2.2.4 Capacitive Sensing Approach

The working principle is to refer the physical displacement at the capacitance pairs to a voltage signal. As a first step, the current is achieved, and it is converted to a voltage with the help of readout electronics. The general expression of the current flow through a capacitor is in the Equation 2.26 where V_{PM} depicts the proof mass voltage, *C (t)* refers to the time varying capacitor, and *X* represents the displacement.

$$I_{out}(t) = \frac{\partial Q(t)}{\partial t} \qquad 2.21$$

$$I_{out}(t) = \frac{\partial\big(C(t)V(t)\big)}{\partial t} \qquad 2.22$$

$$I_{out}(t) = C(t)\frac{\partial\big(V(t)\big)}{\partial t} + V(t)\frac{\partial\big(C(t)\big)}{\partial t} \qquad 2.23$$

$$V(t) = V_{DC} + V_{AC}(t) \tag{2.24}$$

$$C(t) = C_0 + X(t)\frac{\partial\big(C(t)\big)}{\partial x} \tag{2.25}$$

$$I_{out}(jw) = V_{PM}\frac{\partial\big(C(t)\big)}{\partial x} jw.X(jw) \tag{2.26}$$

The current coming from the sensor to a voltage signal could be converted by using trans-impedance amplifier (TIA). The TIA is insensitive to the total capacitance caused by the output capacitance of the chip such as wire bonds, pads, and other parasitic capacitances. Figure 2.4 represents the schematic view of the resonator test setup.

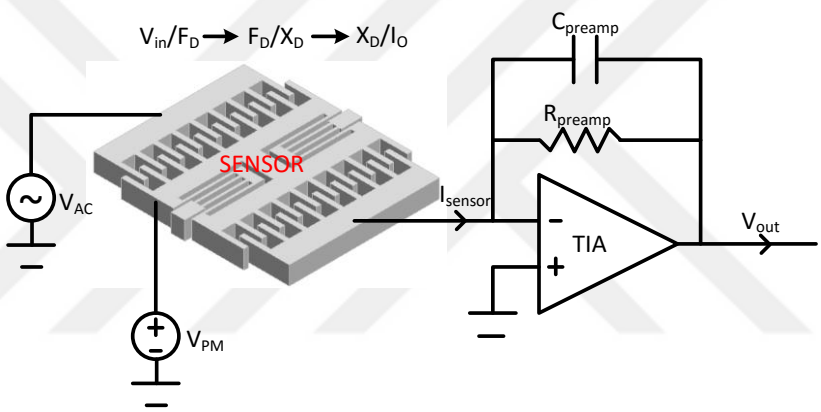

Figure 2.4: Schematic view of the resonator test setup [40].

In the Equation 2.27 shows the overall gain of the system.

$$\left|\frac{V_{out}(s)}{I_{out}(s)}\right| = \frac{R_{preamp}}{1 + sC_{preamp}R_{preamp}} \tag{2.27}$$

- If $sC_{preamp}R_{preamp} \ll 1$, the system is resistive. The current is directly converted to voltage through R_{preamp}. There is no phase difference, but system has higher thermal noise.
- If $sC_{preamp}R_{preamp} \gg 1$, the system is capacitive. The current is directly converted to voltage through the impedance of $\frac{1}{sC_{preamp}}$.

2.3 Micro-Resonators Developed in This Study

The aim of this thesis is to use MEMS resonators in closed loop as oscillators in order to compensate temperature and by combining the resonator's preamplifier output to the accelerometer's carrier generation part. It is aimed because of the fact that in current accelerometer sensors resonance's amplitude changes with the temperature. That is to say, in the scope of this study, it is aimed to use the resonator structure as a temperature sensor together with the controller circuitry. In other words, related study consists of two branches; one is PI controller output which would be used as a temperature sensor and the other is preamplifier output which would generate carrier signal and that would be feed to the accelerometer readout circuitry.

For the above purposes, mainly two types of resonators are designed. First one is, single-mass H-shaped resonators. In this type there were two different actuation mechanism types called varying gap and varying overlap and each of these including resonance frequency of 15 kHz and 45 kHz. Another one is tuning fork (double mass) resonator. By selecting a tuning fork (TF) structure, a high quality factor resonating structure is obtained. Similarly, in this type there were two different types of actuation mechanisms called varying gap and varying overlap and each of these including resonance frequencies of 15 kHz and 45 kHz. To sum up, in this thesis study there are totally 8 different types of designs (Table 2.1). Tuning fork 15 kHz resonator designs are the same with the study as in [40] because this thesis study concept is not fabrication it deals with the concept of the temperature compensation and combining the output of the resonator to the accelerometer. This part describes the design methodologies and variables including the verification of the design with finite element modelling (FEM) simulations.

Table 2.1: Tabulated form of the 8 different resonator design characteristics in the scope of this study.

Design Name	Electrostatic Actuation	Mass Type	Resonance Frequency (kHz)
Design-1	Varying Overlap	Single Mass H-Shaped	15
Design-2	Varying Overlap	Single Mass H-Shaped	45
Design-3	Varying Gap	Single Mass H-Shaped	15
Design-4	Varying Gap	Single Mass H-Shaped	45
Design-5	Varying Overlap	Double Mass (Tuning Fork)	15
Design-6	Varying Overlap	Double Mass (Tuning Fork)	45
Design-7	Varying Gap	Double Mass (Tuning Fork)	15
Design-8	Varying Gap	Double Mass (Tuning Fork)	45

2.3.1 Analytical Modelling Theory

There are many parameters affecting mechanical stiffness like humidity, surface oxidation with time, ionic reactions on the resonator surface, stress induced by the packaging, mechanical fatigue from a long-term operation of resonator and temperature induced changes in the elastic modulus of the resonator materials. Among the others dimensional changes of the resonator structure itself are the most well-known reasons of a resonance frequency and quality factor drift of micro machined resonators. In all the proposed resonating structures current is amplified and transferred to a voltage and a transfer function defined as the division of the output to the input voltage is used to measure the quality factor. The quality factor (Q) could be estimated as given in Equation 2.28 where E represents the energy [54].

$$Q = 2\pi \frac{E_{stored}}{E_{dissipated/cycle}} \qquad 2.28$$

As mentioned in Chapter 1 (Section 1.2.1.2) damping error is majorly based on the shape of the spring used in a chip. In the scope of thesis study folded and half folded spring designs are preferred and spring constant is calculated as in the Equation 2.29 where *N* represents the number of springs; *E* refers to Young's Modulus, t shows the thickness, *W* depicts the width of the structures, and *L* refers to the length of the structures.

$$k = NEt\frac{W^3}{L^3} \qquad 2.29$$

At lower temperatures, thermo-elastic damping (TED) is major energy loss mechanism and the temperature dependence of the total quality factor corresponds to that of the thermoelastic dissipation contribution (TCQ approximately 3.5). However, at a higher temperature, the energy dissipation is controlled by the air damping and for those TCQ is approximately 0.5 [54]. In the scope of this study just air and TED is focused on and temperature dependencies are expressed in Equation 2.30 and 2.31; respectively [54].

$$Q_{air} = C\frac{\sqrt{Tk_b}}{\rho} = C\frac{\sqrt{Tk_b}}{nk_bT} = \frac{1}{\sqrt{T}} \qquad 2.30$$

where ρ is the solid density of the structural material, n is the number density of molecules, T is the temperature, C is a constant involving the surface area that is normal to the direction of the motion, the mode shape of the resonating structures, wall collision effects, etc.; and k_b is the Boltzmann constant. Notice that TCQ_{air} is 0.5 for encapsulated resonators in the pressure limited region [54].

$$Q_{TED} = \left(\frac{f_M^2+f_T^2}{f_M * f_T}\right) * C_p\frac{\rho}{\alpha^2TE} = Q_{TED,freq} * Q_{TED,mat} \qquad 2.31$$

$$f_M = \frac{\beta^2}{2\pi L^2}\sqrt{\frac{EI}{\rho A}} \quad 2.32$$

$$f_T = \frac{\pi k}{2\rho C_p h^2}\sqrt{\frac{EI}{\rho A}} \quad 2.33$$

Where f_M is the mechanical resonant frequency, f_T is the thermal frequency, C_p represents specific heat capacity, ρ is the solid density of the structural material, E is the modulus of elasticity, T is the temperature, β is the mode constant depending on the beam type, A is the area of the cross section, I is the second moment of the inertia, L is the length of the beam, and h is the width of the beam [54].

Furthermore, the change in modulus of elasticity with temperature for Si, TCE is estimated -63.7 ppm/˚C. Besides, Si has an isotropic coefficient of thermal expansion at room temperature of approximately 2.6 ppm/ ˚C and that value relatively increases with increasing temperature. For the detailed information necessary references are given to [54].

When the proposed resonators are operated in an oscillator, the amplitude of the oscillator sine wave output reflects the resonating structure's vibration amplitude. Therefore, a closed loop oscillatory mode readout circuitry is designed (will be investigated in detail in Chapter 4 section 4.3) and that circuitry maintains a constant amplitude of the PI controller output will directly affect the resonator's Q value. Last but not least, it is important to emphasize that mainly the temperature compensation for drift error in the scope of thesis study is taken from experimental data rather than the mathematical modelling theory of error. Therefore, the analytical modelling theory is just given to be aware of the trend.

2.3.2 Single Mass H-Shaped Resonators

Single-mass H-shaped resonators include two different actuation mechanism types called varying gap and varying overlap and each of these including resonance frequency of 15 kHz and 45 kHz. This section presents the design procedures and

parameters of single mass H-shaped resonators. Both varying gap and varying overlap types are designed to observe the difference in terms of temperature sensitivity.

2.3.2.1 Varying Overlap Type Single Mass H-Shaped Resonators

Two different single mass H-shaped resonators are designed using the varying overlap area configuration. The difference originates from the width of the folded springs. There are two different types in order to analyse the effects in low and high resonance frequencies. Figure 2.5 presents the layout of the 15 kHz (Design-1) and 45 kHz (Design-2) types. Moreover, Table 2.2 presents the design parameters for single mass H-shaped micro resonator types.

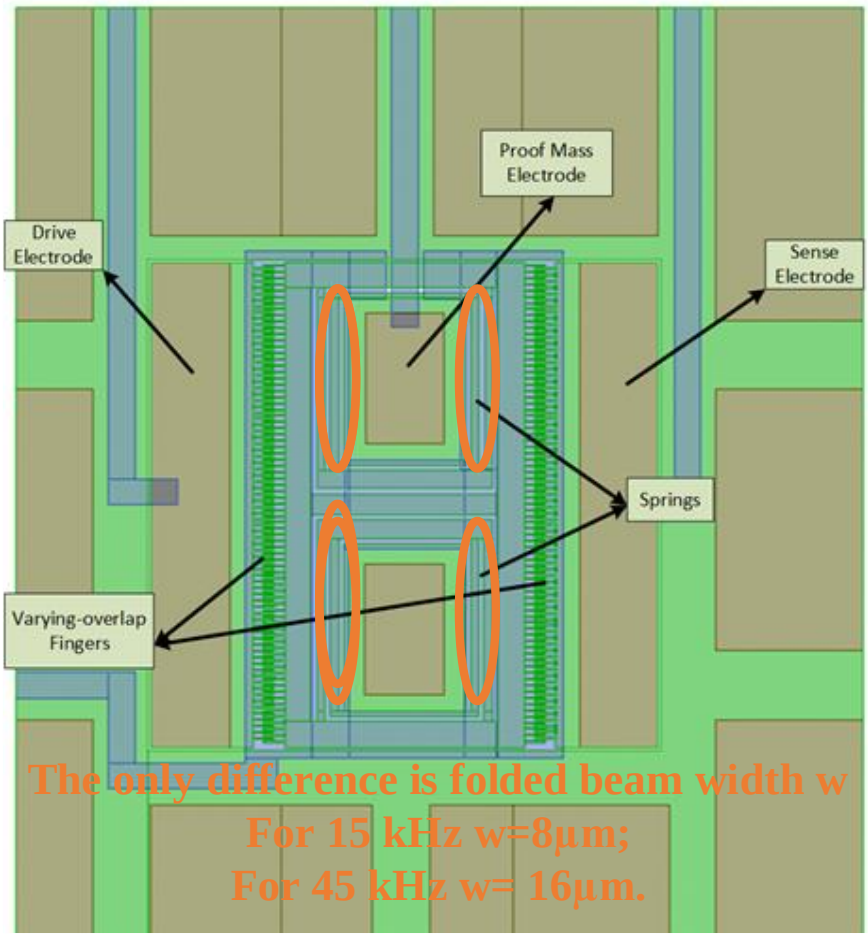

Figure 2.5: Picture of the layout of the designed varying overlap type single mass H-shaped resonator with 15 kHz resonance frequency (Design-1) and 45 kHz resonance frequency (Design-2) for temperature compensation.

Table 2.2: Design parameters of varying overlap area type single mass H-shaped resonator Design-1 and Design-2.

Parameters	Design-1	Design-2
# of capacitive fingers (*N*)	77	77
Finger overlap length (*l*)	20 µm	20 µm
Finger width (*w*)	4 µm	4 µm
Finger gap (*d*)	2 µm	2 µm
Finger thickness (*t*)	35 µm	35 µm
Capacitance (*C*)	4.8 pF	4.8 pF
dC/dx	2.39×10^{-8} F/m	2.39×10^{-8} F/m
Spring Constant (*k*)	189 N/m	1520 N/m
Mass (*m*)	1.311×10^{-9} kg	1.972×10^{-9} kg
Resonance Frequency (f_r)	18 kHz	50 kHz

2.3.2.2 Varying Gap Type Single Mass H-Shaped Resonators

Similar to the varying overlap type designs, two different single mass H-shaped resonators are designed with the varying gap configuration. The difference originates from the width of the folded springs. There are two different types in order to observe the effects in low and high resonance frequencies. Figure 2.6 presents the layout of the 15 kHz (Design-3) and 45 kHz (Design-4) types. Table 2.3 presents the design parameters for single mass H-shaped micro resonator types.

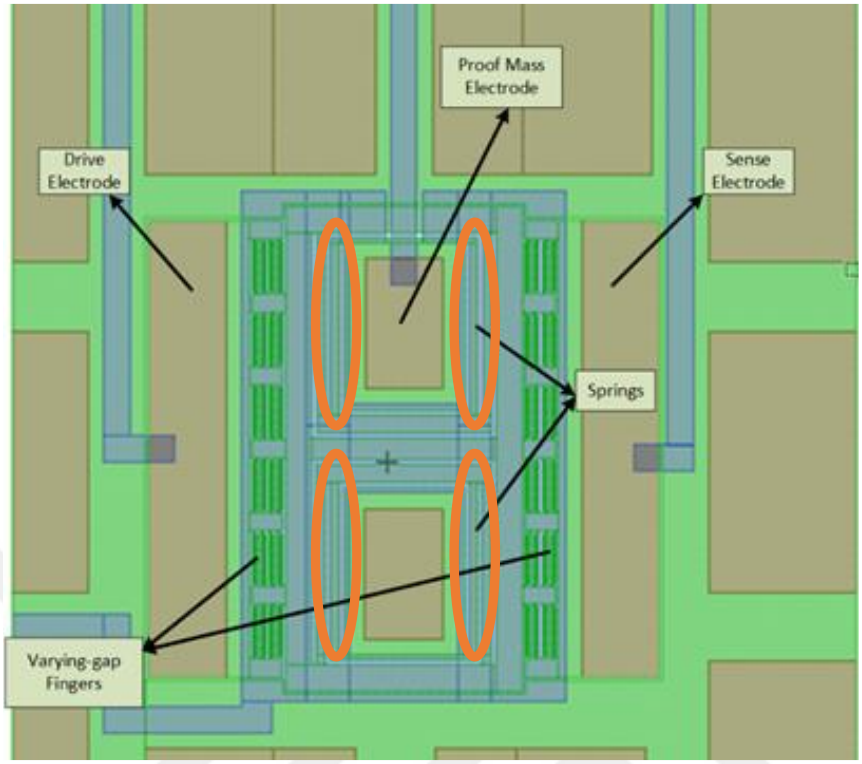

The only difference is folded beam width w
For 15 kHz w=8µm;
For 45 kHz w= 16µm.

Figure 2.6: Picture of the layout of the designed varying gap type single mass H-shaped resonator with 15 kHz resonance frequency (Design-3) and 45 kHz resonance frequency (Design-4) for temperature compensation.

Table 2.3: Design parameters of varying gap area type single mass H-shaped resonator Design-3 and Design-4.

Parameters	Design-3	Design-4
# of capacitive fingers (N)	24	24
Finger overlap length (l)	95 µm	95 µm
Finger width (w)	4 µm	4 µm
Finger gap (d)	2 µm	2 µm
Finger anti-gap ($d_{anti-gap}$)	6 µm	6 µm
Finger thickness (t)	35 µm	35 µm
Capacitance (C) (Gap)	3.5 pF	4.8 pF
dC/dx(Gap)	1.77×10^{-7} F/m	1.77×10^{-7} F/m
Capacitance (C) (Anti-gap)	1.1 pF	1.1 pF
dC/dx(Anti-gap)	1.96×10^{-8} F/m	1.96×10^{-8} F/m
Spring Constant (k)	189 N/m	1520 N/m
Mass (m)	1.311×10^{-9} kg	1.972×10^{-9} kg
Resonance Frequency (f_r)	18 kHz	52 kHz

2.3.3 Tuning Fork Resonators

Tuning fork resonators include two different actuation mechanism types called varying gap and varying overlap and each of these including resonance frequencies of 15 kHz and 45 kHz. This section presents the design procedures and parameters. Both tuning fork varying gap and tuning fork varying overlap types are designed to observe the difference in terms of temperature sensitivity.

2.3.3.1 Varying Overlap Type Double Mass Resonators

Two different double mass type resonant devices are proposed applying the varying overlap area configuration. The difference is coming from the width of the folded springs. There are two different types because of analysing what happens in low and high resonance frequencies. Figure 2.7 presents the layout of the 15 kHz (Design-5) and 45 kHz (Design-6) types. Table 2.4 presents the design parameters for tuning fork varying overlap micro resonator types.

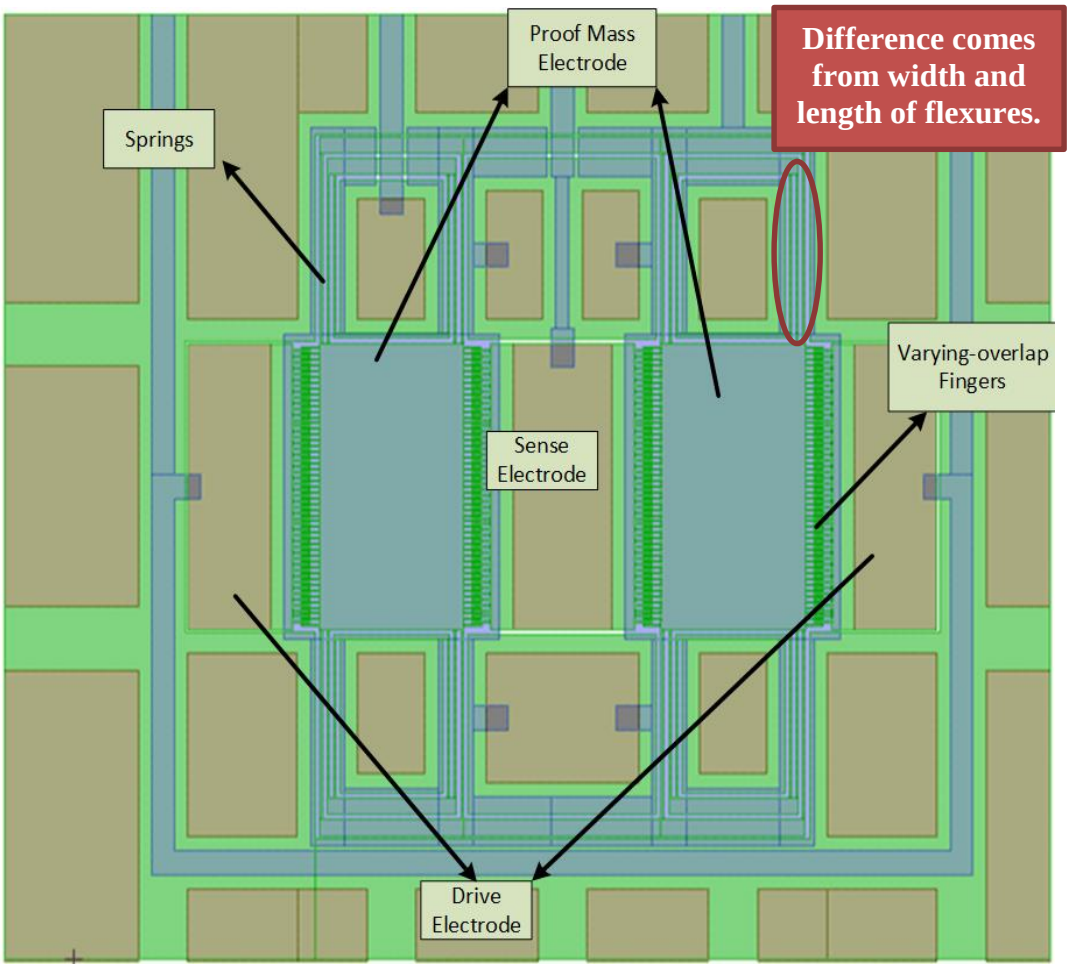

Figure 2.7: Picture of the layout of the designed tuning fork varying overlap type resonator with 15 kHz resonance frequency (Design-5) and 45 kHz resonance frequency (Design-6) for temperature compensation.

Table 2.4: Design parameters of tuning fork varying overlap area type resonator Design-5 and Design-6.

Parameters	Design 5	Design 6
# of capacitive fingers (N)	98	98
Finger overlap length (l)	20 µm	20 µm
Finger width (w)	4 µm	4 µm
Finger gap (d)	2 µm	2 µm
Finger thickness (t)	35 µm	35 µm
Capacitance (C)	6.1 pF	6.1 pF
dC/dx	3.04×10^{-8} F/m	2.39×10^{-8} F/m
Spring Constant (k)	389 N/m	4810 N/m
Mass (m)	3.970×10^{-8} kg	3.970×10^{-8} kg
Resonance Frequency (f_r)	15 kHz	55 kHz

2.3.3.2 Varying Gap Type Tuning Fork Resonators

Two different tuning fork type resonant structures are proposed using the varying overlap area configuration. The difference is due to different length of the folded springs. There are two different types because of analysing what happens in low and high resonance frequencies. Figure 2.8 presents the layout of the 15 kHz (Design-7) and 45 kHz (Design-8) types. Table 2.5 presents the design parameters for tuning fork varying gap micro resonator types.

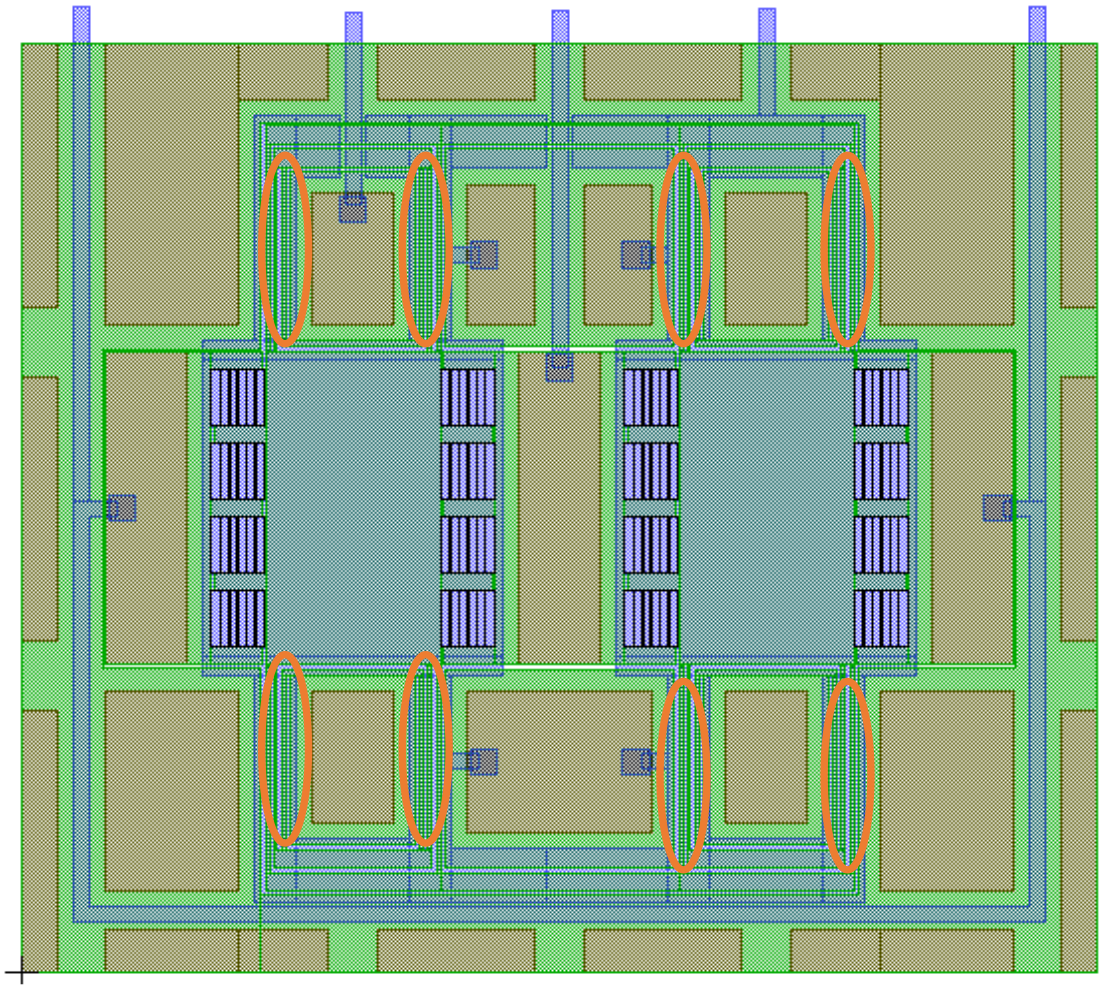

The only difference is folded beam length L
For 15 kHz L= 330 µm;
For 45 kHz L=120 µm.

Figure 2.8: Picture of the layout of the designed tuning fork varying gap type resonator with 15 kHz resonance frequency (Design-7) and 45 kHz resonance frequency (Design-8) for temperature compensation.

Table 2.5: Design parameters of tuning fork varying gap area type resonator Design-7 and Design-8.

Parameters	Design-7	Design-8
# of capacitive fingers (N)	48	48
Finger overlap length (l)	95 μm	95 μm
Finger width (w)	4 μm	4 μm
Finger gap (d)	2 μm	2 μm
Finger anti-gap ($d_{anti-gap}$)	6 μm	6 μm
Finger thickness (t)	35 μm	35 μm
Capacitance (C) (Gap)	7.1 pF	7.1 pF
dC/dx(Gap)	3.53×10^{-7} F/m	3.53×10^{-7} F/m
Capacitance (C) (Anti-gap)	2.4 pF	2.4 pF
dC/dx(Anti-gap)	3.92×10^{-8} F/m	3.92×10^{-8} F/m
Spring Constant (k)	389 N/m	4810 N/m
Mass (m)	4.03×10^{-8} kg	4.03×10^{-8} kg
Resonance Frequency (f_r)	15 kHz	54 Hz

2.4 Finite Element Simulations

Finite-element method (FEM) is one of the numerical techniques for investigating the behavior of the systems. The resonator structures have to be checked by some simulations for verifying if there exists any undesired operational characteristics of the resonant structures that is not foreseen in the design procedure. In this study, FEM simulations are conducted to see the mode shapes and modal frequencies of the MEMS resonators. CoventorWare, is a simulation platform optimized for MEMS devices, and is applied to perform the FEM simulations. Mode shape simulations have been performed for the first 3 modes of the micromachined resonators.

Figure 2.9 and Figure 2.10 represents the 15 kHz single mass H-shaped FEM simulation results for varying overlap area type (Design-1) and varying gap type

(Design-3) resonators; respectively. Table 2.6 presents the comparison of mode shape simulation results for 15 kHz single mass H-shaped varying overlap type (Design-1) and varying gap (Design-3) resonator sensors.

Table 2.6: Comparison of mode shape simulation results for varying gap and overlap type single mass H-shaped resonators with the resonance frequency of 15 kHz.

Modes	**Design-1**	**Design-3**
1st mode	15.1 kHz	15.9 kHz
2nd mode (operation mode)	53.4 kHz	50.5 kHz
3rd mode	55.8 kHz	55.8 kHz

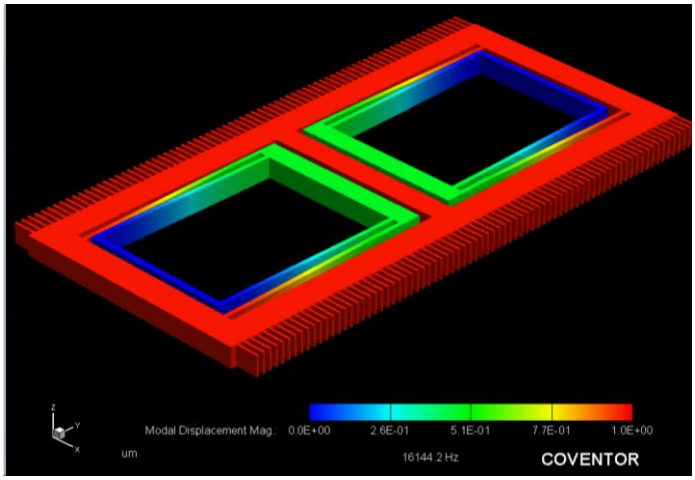

(a)

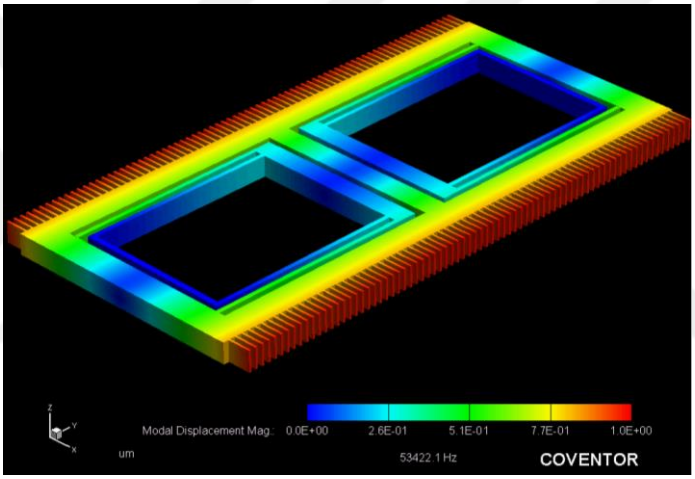

(b)

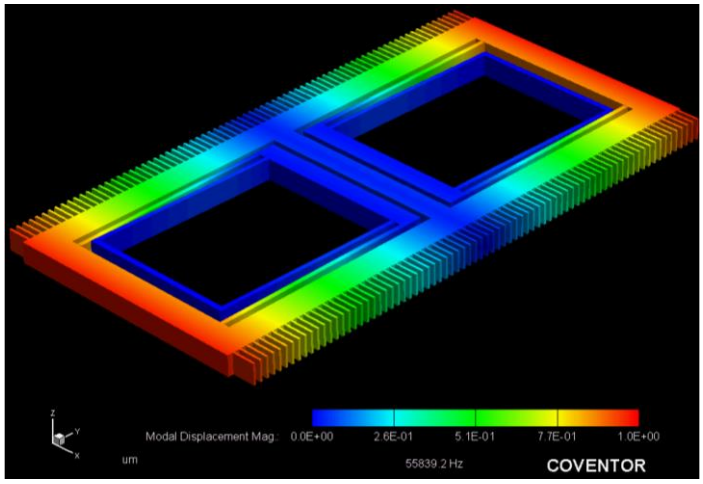

(c)

Figure 2.9: Mode shape simulations of varying overlap area type single mass H-shaped resonator (Design-1): (a) 1st mode: 15.1 kHz, (b) 2nd mode: 53.4 kHz, (c) 3rd mode: 55.8 kHz.

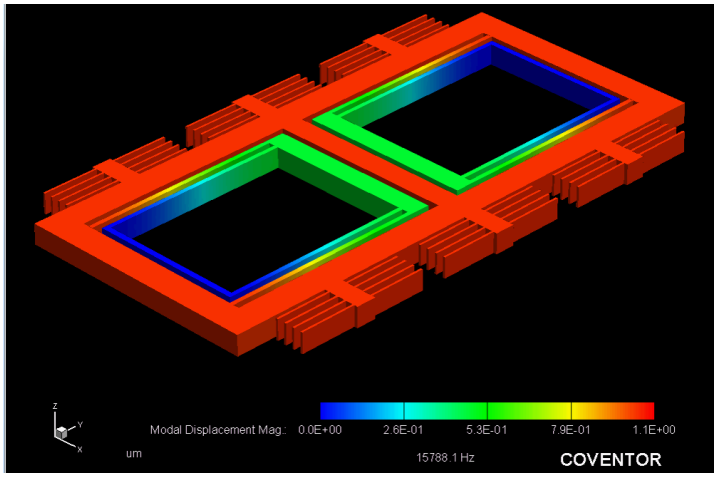

(a)

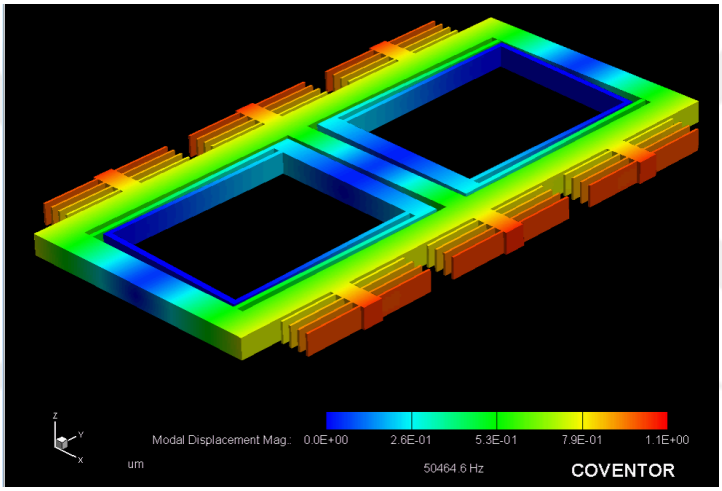

(b)

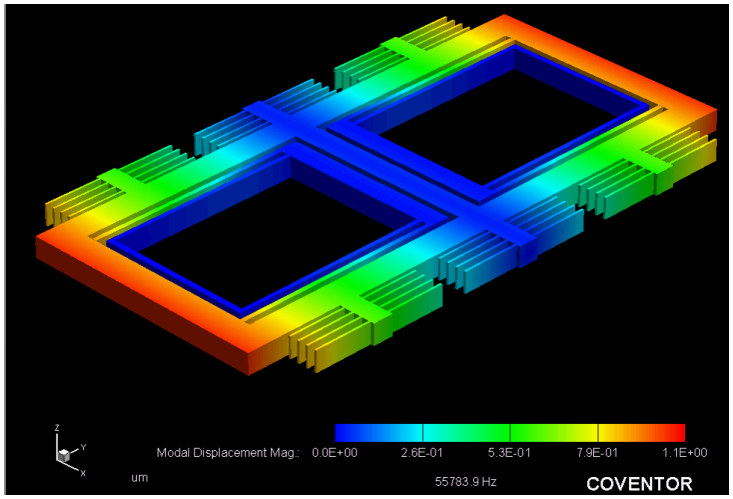

(c)

Figure 2.10: Mode shape simulations of varying gap area type single mass H-shaped resonator (Design-3): (a) 1st mode: 15.86 kHz, (b) 2nd mode: 50.5 kHz, (c) 3rd mode: 55.8 kHz.

Figure 2.11 and Figure 2.12 present the mode shape simulation results for varying overlap area (Design-2) and varying gap (Design-4) type single mass H-shaped resonators with the resonance frequency of 45 kHz. Table 2.7 shows the comparison of mode shape simulation results for varying overlap type (Design-2) and varying gap (Design-4) single mass H-shaped resonators of the resonance frequency of 45 kHz.

Table 2.7: Comparison of mode shape simulation results for varying overlap (Design-2) and varying gap (Design-4) and type single mass H-shaped resonators with the resonance frequency of 45 kHz.

Modes	**Design-2**	**Design-4**
1st mode	42.5 kHz	41.5 kHz
2nd mode (operation mode)	72.3 kHz	70.0 kHz
3rd mode	72.7 kHz	72.3 kHz

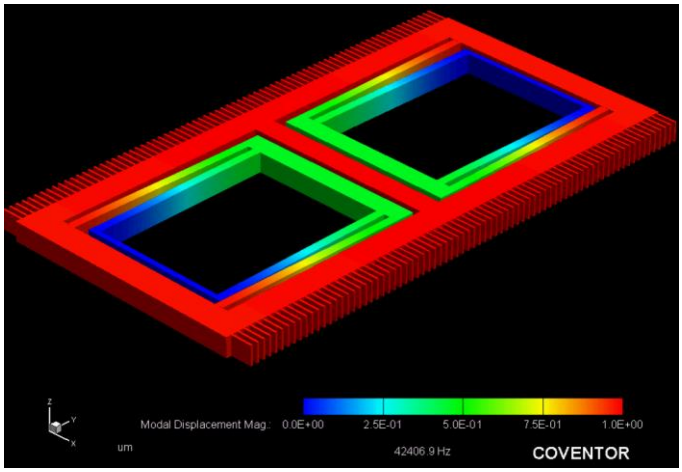

(a)

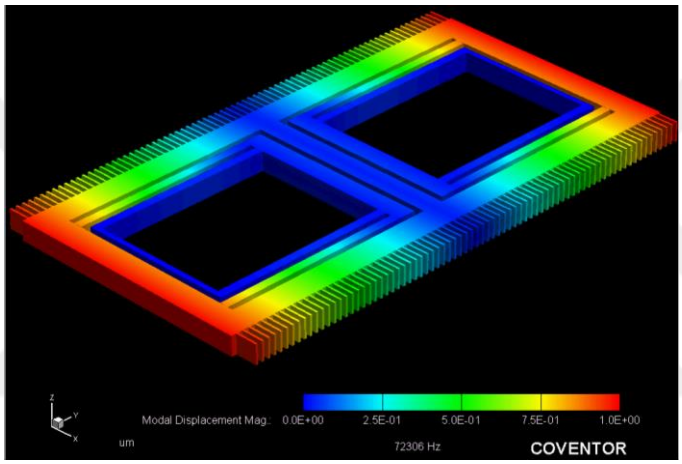

(b)

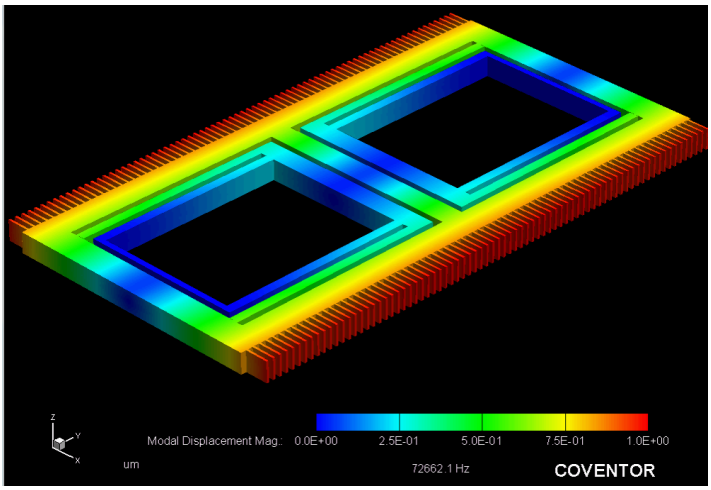

(c)

Figure 2.11: Mode shape simulations of varying overlap area type single mass H-shaped resonator with the resonance frequency of 45 kHz (Design-2): (a) 1st mode: 42.5 kHz, (b) 2nd mode: 72.3 kHz, (c) 3rd mode: 72.7 kHz.

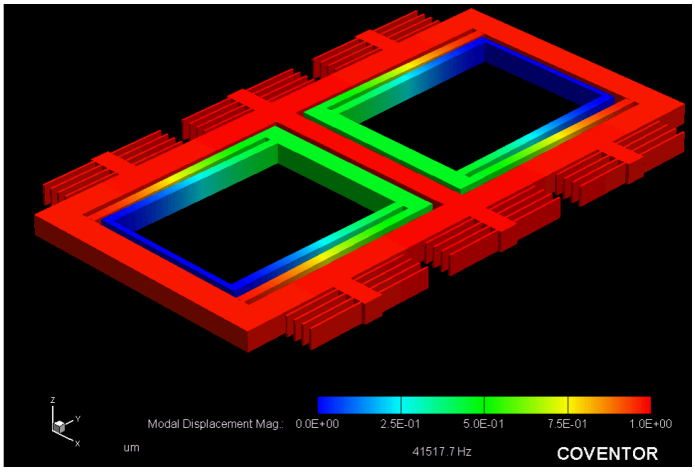

(a)

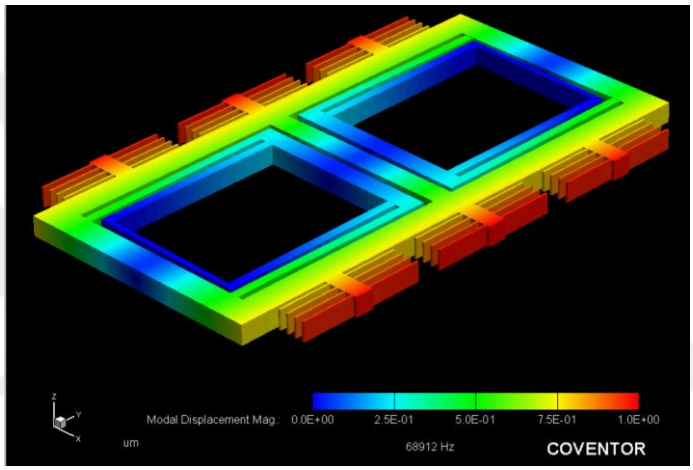

(b)

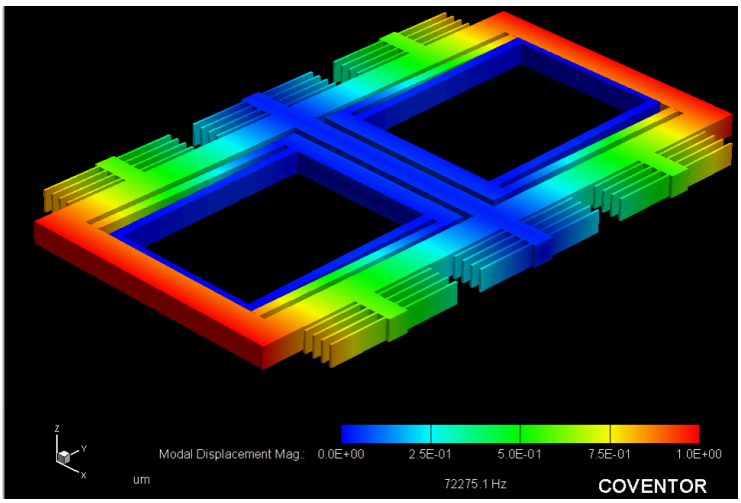

(c)

Figure 2.12: Mode shape simulation results of varying gap area type single mass H-shaped resonator with the resonance frequency of 45 kHz (Design-4): (a) 1st mode: 41.5 kHz, (b) 2nd mode: 70 kHz, (c) 3rd mode: 72.3 kHz.

Figure 2.13 and Figure 2.14 show the FEM simulation result of the 15 kHz TF varying overlap area (Design-5) and TF varying gap (Design-7) type resonators. Table 2.8 presents the comparison of them.

Table 2.8: Comparison of mode shape simulation results for varying overlap type (Design-5) and varying gap (Design-7) tuning fork (TF) resonators with the resonance frequency of 15 kHz.

Modes	**Design-5**	**Design-7**
1st mode	6.5 kHz	6.0 kHz
2nd mode (operation mode)	15.1 kHz	14.5 kHz
3rd mode	30.7 kHz	30.7 kHz

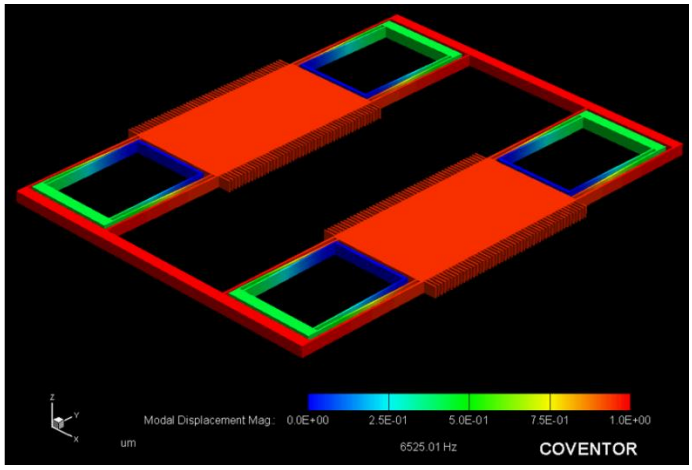

(a)

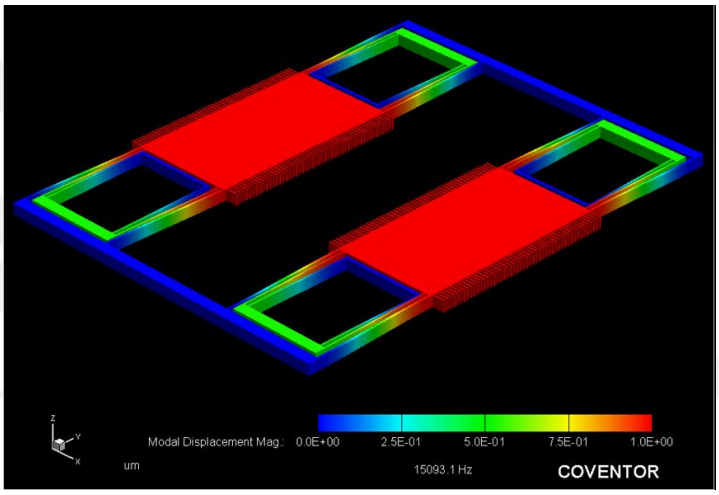

(b)

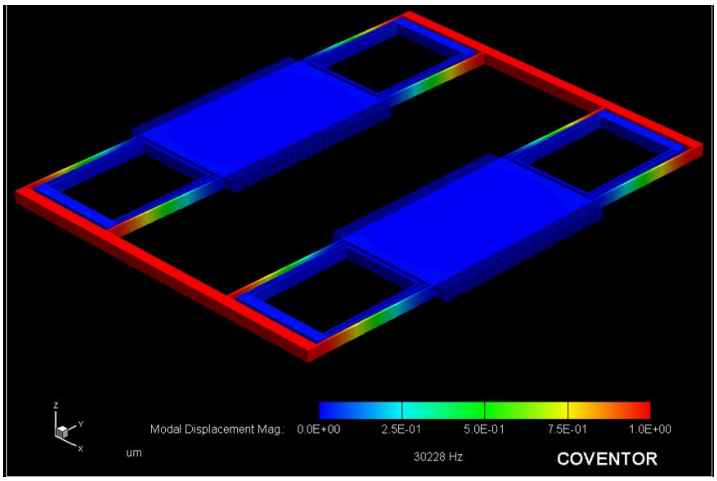

(c)

Figure 2.13: Mode shape simulation results of varying overlap area type tuning fork resonator (Design-5): (a) 1st mode: 6.5 kHz, (b) 2nd mode: 15 kHz, (c) 3rd mode: 30.2 kHz.

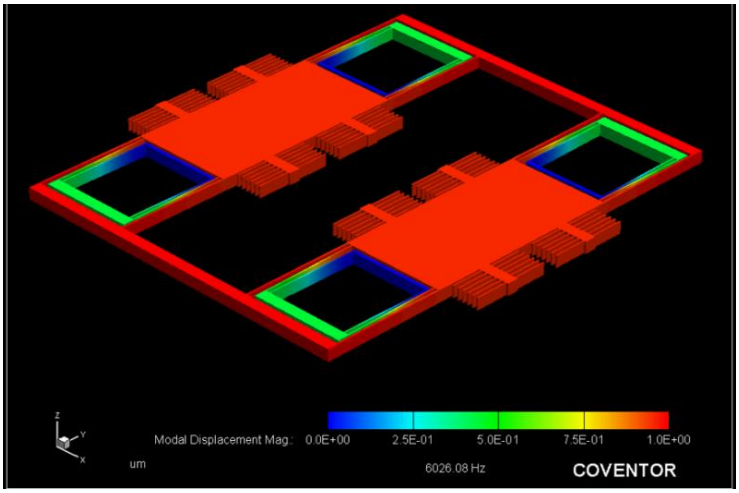

(a)

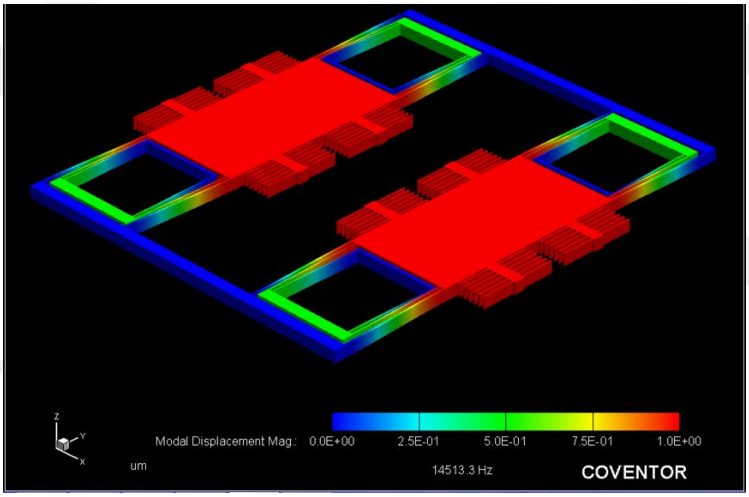

(b)

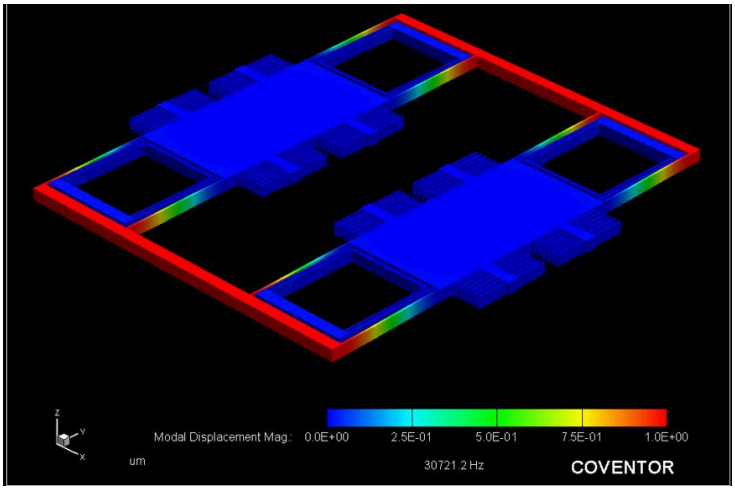

(c)

Figure 2.14: Mode shape simulation results of 15 kHz varying gap area type tuning fork resonator (Design-7): (a) 1st mode: 6 kHz, (b) 2nd mode: 14.5 kHz, (c) 3rd mode: 30.7 kHz.

Figure 2.15 and Figure 2.16 present the mode shape simulation results for varying overlap area (Design-6) and varying gap (Design-8) and type tuning fork resonators with the resonance frequency of nearly 45 kHz. Table 2.9 shows the comparison of mode shape simulation results for varying overlap type (Design-6) and varying gap (Design-8) and tuning fork (TF) resonators of the resonance frequency of 45 kHz.

Table 2.9: Comparison of mode shape simulation results for varying overlap (Design-6) and varying gap (Design-8) type tuning fork (TF) resonators with the resonance frequency of 45 kHz.

Modes	**Design-6**	**Design-8**
1st mode	28.3 kHz	27.0 kHz
2nd mode (operation mode)	45.8 kHz	44.0 kHz
3rd mode	74.5 kHz	71.4 kHz

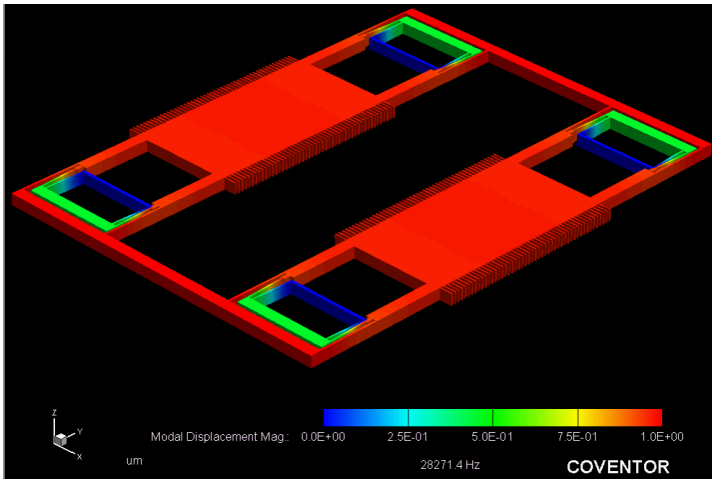

(a)

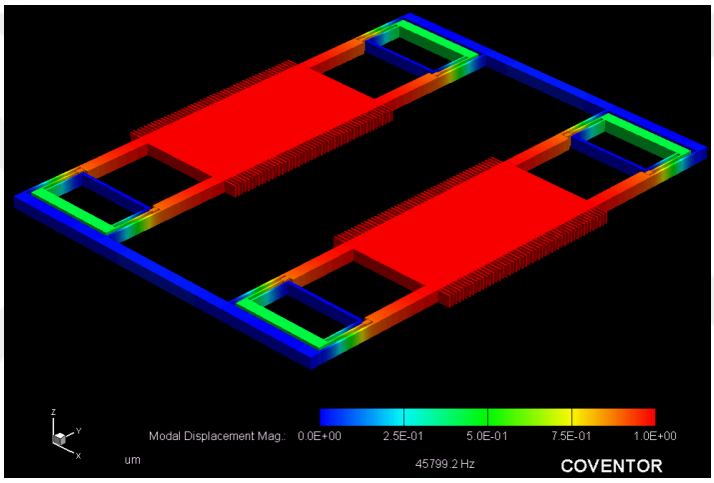

(b)

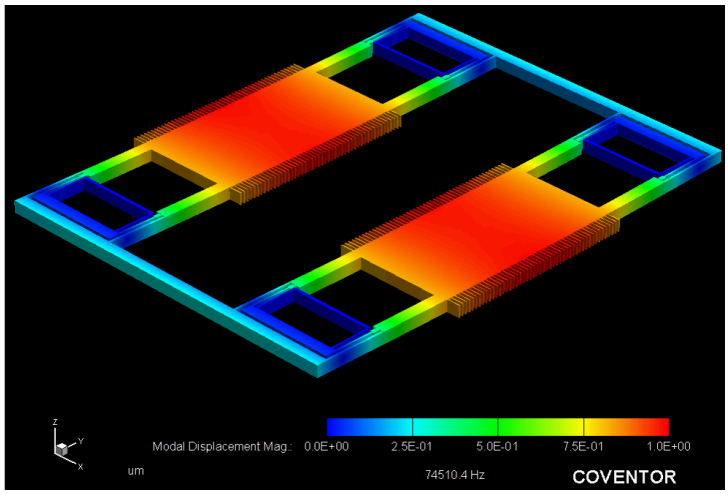

(c)

Figure 2.15: Mode shape simulation results of varying overlap area type tuning fork resonator of the resonance frequency nearly 45 kHz (Design-6): (a) 1st mode: 28.3 kHz, (b) 2nd mode: 45.8 kHz, (c) 3rd mode: 74.5 kHz.

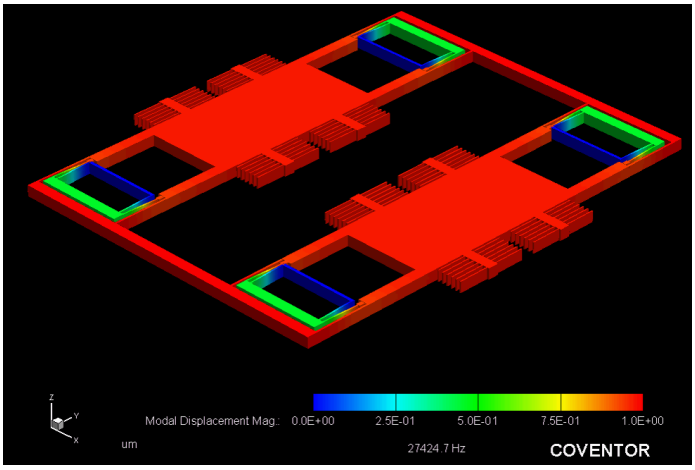

(a)

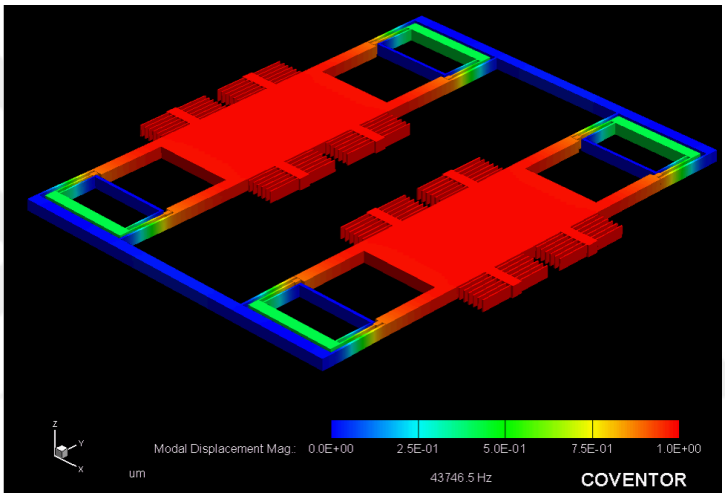

(b)

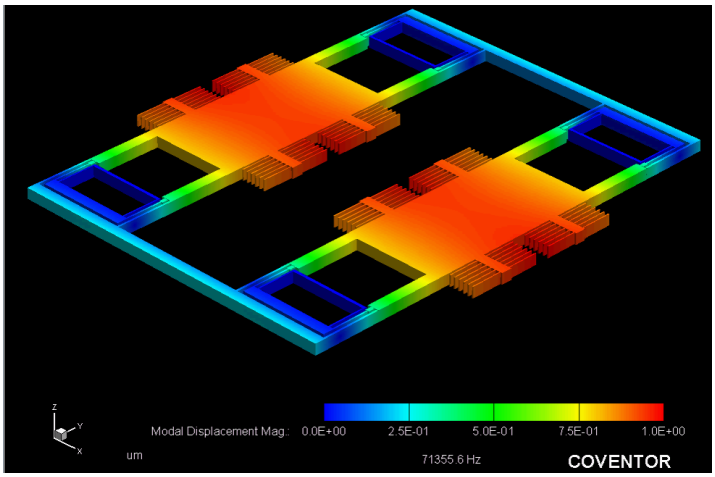

(c)

Figure 2.16: Mode shape simulation results of varying gap area type tuning fork resonator of nearly 45 kHz (Design-8): (a) 1st mode: 27 kHz, (b) 2nd mode: 44 kHz, (c) 3rd mode: 71.4 kHz.

2.5 Implementation of Single Mass and Tuning Fork Type Resonators in the Same Die

The resonator mask set is designed by using the L-Edit Software. In order to make an exact comparison in the same environmental conditions, 4 different resonator designs are implemented in a same die. Figure 2.17 shows the packaged layout of a die including TF and single mass varying overlap and varying gap type resonators. It should be noticed that these designs would be compatible with both anodic and eutectic bonding.

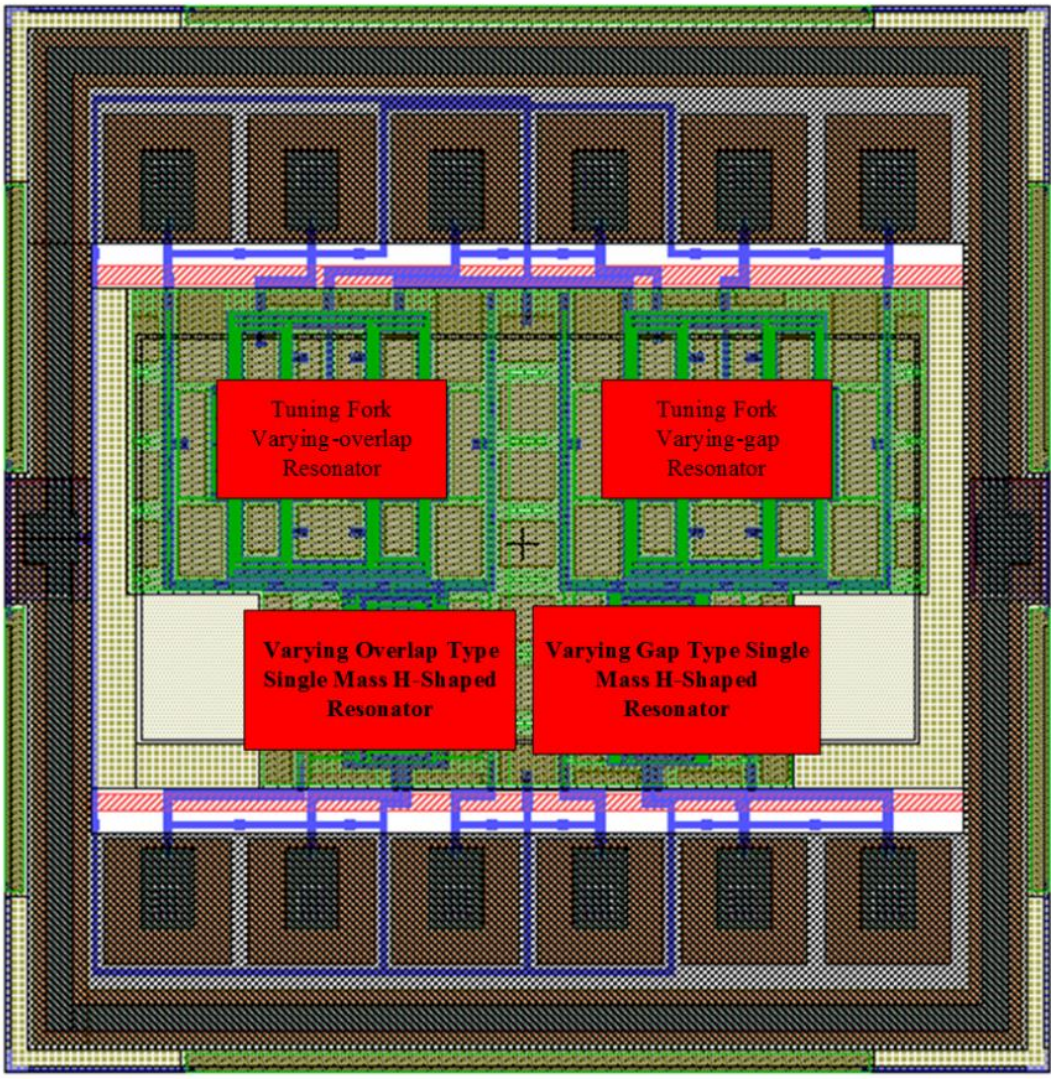

Figure 2.17: The packaged layout of a die including TF and single mass varying overlap and varying gap type resonators.

2.6 Summary

This chapter provides information about the designs of the MEMS resonators studied in this thesis. The chapter starts with the theoretical background including mechanical and electrical design of MEMS resonators followed by the design parameters of single mass H-shaped and TF resonators. These designs are checked with FEM simulations for determining the modes and resonance frequencies of the resonators. In conclusion, all of these structures are integrated in a same die for comparing their performances in the same working environment.

CHAPTER 3

FABRICATION OF MEMS RESONATORS USING ADVANCED MEMS (*aMEMS*) PROCESS

This chapter presents the fabrication of 8 different MEMS resonator designs using two different sensor structures (single mass and tuning fork resonators) with two different actuation mechanisms (varying overlap and varying gap) at different operation frequencies (15 and 45 kHz) by using the advanced MEMS (*aMEMS*) process [40, 41, 44-48]. The *aMEMS* is based on the synergistic combination of M-SOG (modified silicon-on-glass) process [42], which is used to fabricate MEMS resonant structure and wafer-level packaging by selecting SOI cap wafers. In other words, the advanced MEMS process includes the bonding of an SOI cap wafer to a MEMS resonant sensor wafer which is fabricated by modified SOG process.

MEMS sensors are fabricated with anodic bonding of a silicon wafer to a glass wafer by the application of SOG process. In the M-SOG process, after the recesses and electrical connections are performed on the glass wafers; the construction of the device layer is done on the SOI wafer using deep reactive ion etching (DRIE). As the final step, glass wafer and SOI wafer are bonded to each other using the anodic bonding technique [43]. The M-SOG process has various advantages ranging from decreasing the parasitic capacitances by patterning device metallization on the glass wafer, selection of optimum electrical and mechanical properties of the proof mass by selecting the device layer of the SOI wafer, uniform DRIE etch profile, and higher production yield.

SOI cap substrates are preferred for the batch fabricated hermetic encapsulation of the processed chips. In the cap wafer process 300 μm handle, 2 μm buried oxide and 100 μm device layer thick SOI wafer is used. At the beginning of the cap wafer fabrication, first of all, via openings are patterned on the handle layer of SOI cap substrate. After via openings are formed, vertical feedthroughs and sealing walls are simultaneously constructed on the device layer of the wafer. In the *aMEMS* process, "sealing of the sensor wafer with the SOI cap wafer is achieved either by the anodic bonding" [44], [45] process or by the Au-Si [46], [47] or Au-Sn [48] eutectic bonding approaches. It would be better to mention that the process steps for both bonding processes are very similar but difference occurs in the sequence of the steps. In the aMEMS process, the most significant achievement is the integration of vertical feedthroughs that are patterned on an SOI substrate by selecting basic MEMS etching methods [40].

The chapter is as follows, Section 3.1 provides the detailed information of the MEMS sensor wafer fabrication by using M-SOG. Section 3.2 describes the SOI cap wafer fabrication as well as the hermetic encapsulation with the anodic bonding. Section 3.3 presents the fabrication results by analyzing SEM images. At the end, Section 3.4 concludes the chapter.

3.1 Fabrication of Sensor Wafer Applying Modified Silicon-On-Glass (M-SOG) Process

The M-SOG technology includes the processing on both glass and SOI wafers. After processing both glass and SOI wafers separately, then anodic bonding is performed to bond the wafers to the each other. Sensor wafer fabrication is completed with the release of the device structure after the anodic bonding. The remaining paragraphs of this subsection includes the details of the fabrication of the sensor wafer beginning with the processes on the glass and SOI wafers; then, anodic bonding of glass and SOI wafers and ends with the release of the device structure.

The glass wafer process starts with a blank glass wafer (Figure 3.1.a) to pattern anchors and metallic interconnections. The anchor formation is the starting point; which is very significant during bonding; due to the fact that the anchor regions are going to be added

to the device layer of the SOI substrate during the anodic bonding. At the beginning of the anchor formation, the roughening of the glass surface using BHF (buffered hydrofluoric acid) is done. The purpose of this step is to make the glass surface roughed before the metal deposition because metal layers have a better adhesion to roughed surfaces compared to polished surfaces. After roughening, Chromium/Gold (Cr/Au) is coated on the glass substrate with thermal evaporation; for protecting material instead of photoresist (PR) during the anchor formation process in the hydrofluoric acid (HF) since the etch rate of HF to PR is very high. After that, Cr/Au layer is formed using wet etchants in the order of gold etchant and chromium etchant. After that, glass is etched in the pure HF solution to construct the anchors. During etching the glass, undercut should be taken into consideration when designing the anchor areas. Because glass etches process is isotropic. Besides, the etching rate of HF for the glass is dramatically the environment temperature dependent; therefore, etching process ought to be performed by measuring the depth of the anchors in a controlled manner. The ratio of the undercut measured after the glass etching varies from 1 to 1.3. At the end of the anchor formation, Cr/Au is stripped in the wet etchants to prepare the wafer for the next process step (Figure 3.1.b).

The glass wafer process continues with the process of the electrical interconnections. As similar to first step, this step also starts with the roughening of the glass surface in the BHF before the metal deposition. After roughening, Cr/Au is coated by applying evaporation. Then, Cr/Au is used to construct the pad metallization with the help of wet chemical etchants. As a final step glass substrate becomes smooth in the piranha solution which consists of H_2SO_4:H_2O_2 with ratio of 1:1 before the anodic bonding. After the piranha cleaning procedure the glass substrate fabrication is completed and it is ready for anodic bonding (Figure 3.1.c).

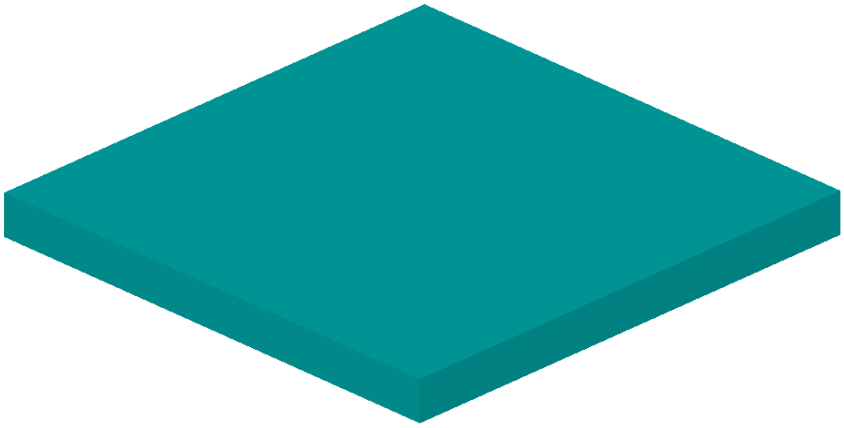

(a) Empty glass wafer which is 500µm thick

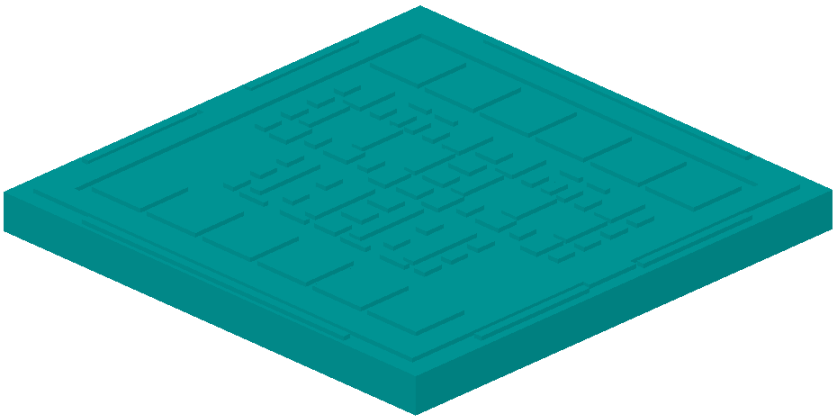

(b) Anchor formation

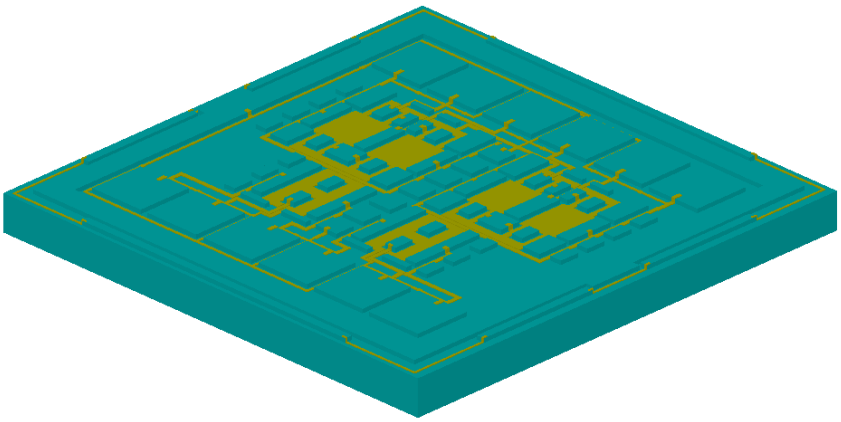

(c) Formation of the electrical interconnects

Figure 3.1: Process grades of the glass wafer with the modified SOG process.

As mentioned previously, SOI wafer fabrication consists of two major classes: shallow etch and structure construction; respectively. The ongoing process is the shallow etch formation on the device layer of SOI substrate. The aim of the shallow etch step is to eliminate the bonding of the undesired silicon region on the glass wafer during the first anodic bonding. In this step, this silicon region on the SOI wafer is etched in the DRIE. Notice that it is a temporary process step to protect the undesired silicon region during the anodic bonding because the etched region is completely separated from the SOI wafer after the sensor wafer fabrication is completed. During the DRIE step, also the PR is stripped by using the oxygen plasma. After completing the DRIE process, the piranha cleaning is performed for the SOI substrate (Figure 3.3.b).

As a second step the resonator structure on the device layer applying the DRIE is formed (Figure 3.3.c). Notice DRIE etches anisotropically; therefore, it is one of the best ways for constructing of the resonating device with critical dimensions. The PR is again stripped by preferring the oxygen plasma in the DRIE. At the end of the DRIE step, the piranha cleaning is come for the SOI substrate to completely get rid of the polymer residuals on the substrate.

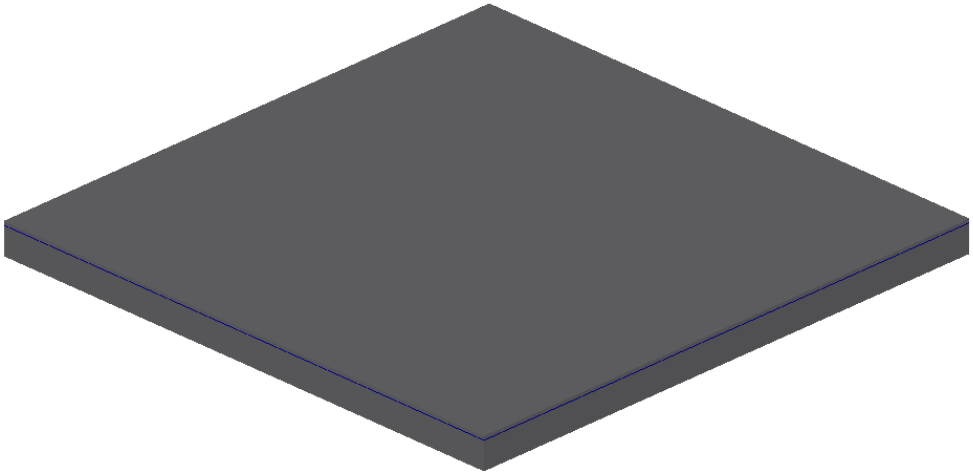

(a) Empty SOI wafer (35µm device layer, 2µm buried oxide, 300µm handle layer thickness)

Figure 3.2: Process path of the SOI sensor wafer with the modified SOG process.

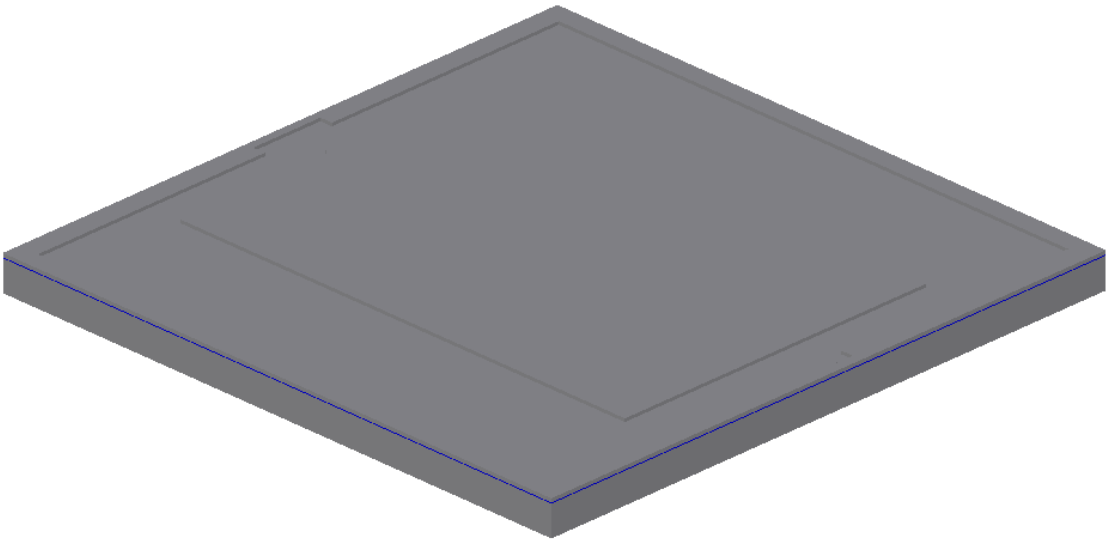

(b) Constructing shallow etches on the device layer

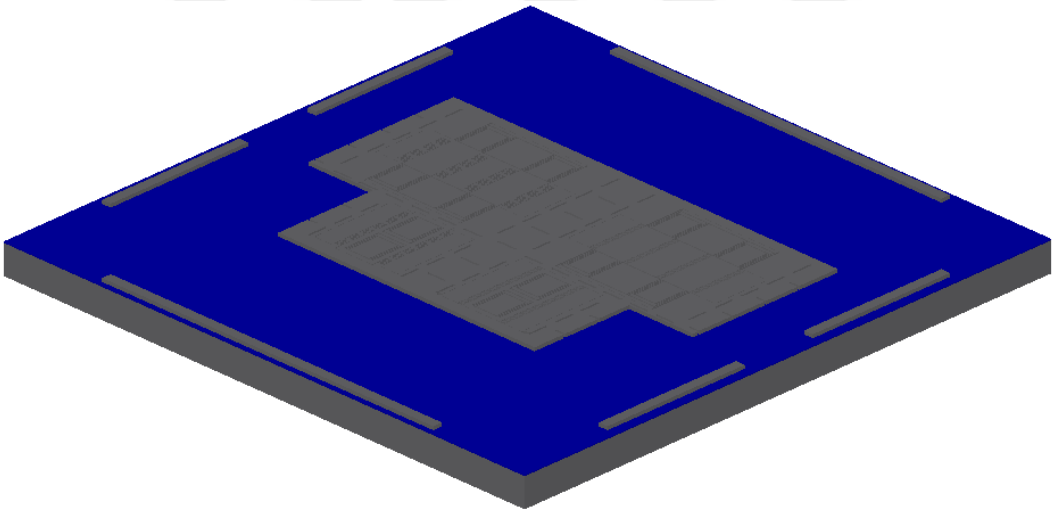

(c) Constructed resonator structure

Figure 3.3: (continued)

At the end of the process of glass and SOI wafers, these wafers are bonded to each other by anodic bonding at 370ºC, 1200V, and 1500N (Figure 3.4) using the method detailed in [43]. Before starting the anodic bonding, the native oxide layer on the silicon wafer ought to be stripped with a short BHF dip for improving the Au-Si ohmic contact quality. At the end of the anodic bonding, the handle layer of the SOI substrate is disappeared by applying the DRIE. As a final step, the device layer attached to the

glass substrate is processed by releasing the buried oxide layer in the BHF solution. Figure 3.5 shows the process steps of the sensor wafer with the modified SOG process.

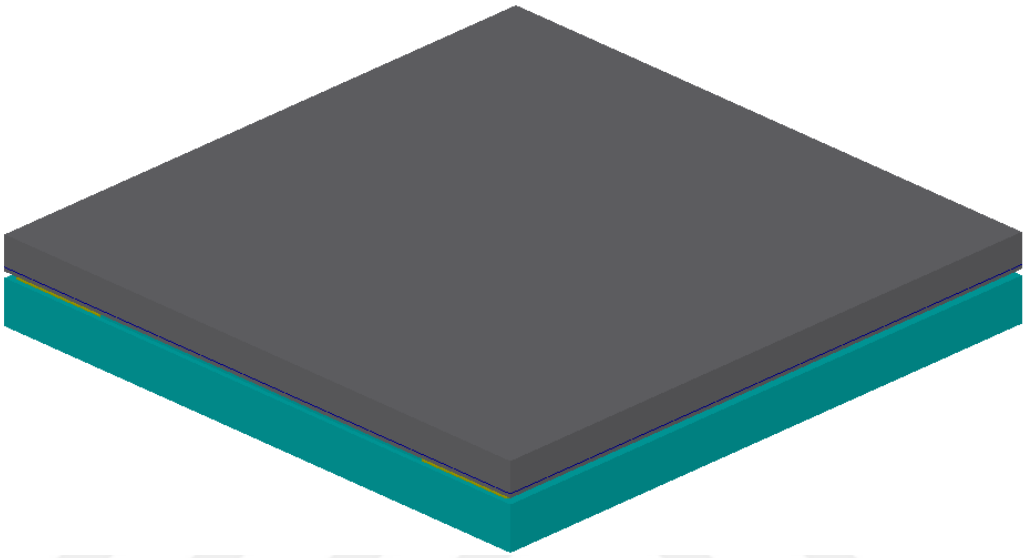

Figure 3.4: After the anodic bonding of glass and SOI substrates.

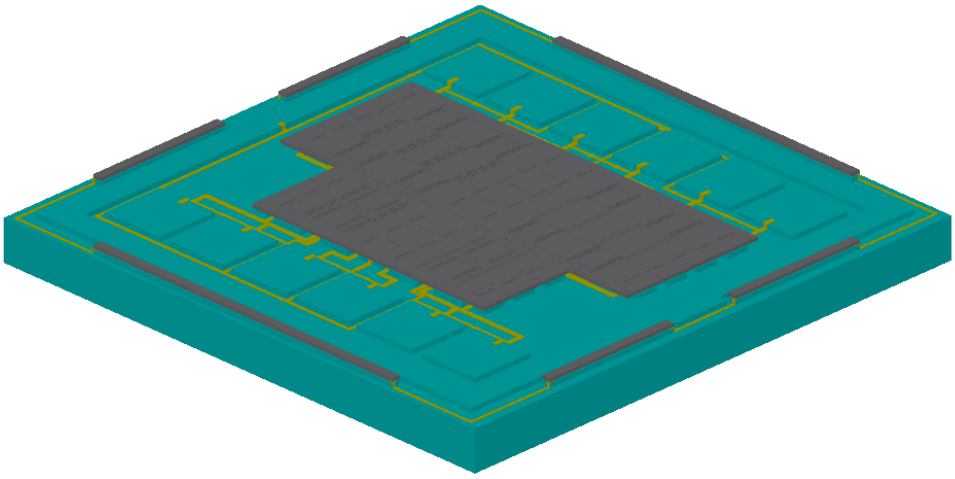

Figure 3.5: Fabricated uncapped resonator sensor wafer with the modified SOG process.

3.2 Wafer Level Packaging of MEMS Sensor Wafers with SOI Cap Wafers

Packaging of the sensor wafer is obtained by selecting an SOI cap substrate, and the pads on the resonating structures are transferred to the outside via the vertical feedthroughs using the advanced MEMS process. SOI cap substrate consists of highly doped handle and device parts, and both sides are deposited with the thermal oxide. The SOI cap substrate processing for the encapsulation is combination of four masks: via openings, formation of the pad metals, formation of the cavities and deposition of thin film getter. The detailed process description can be found in [40]. Figure 3.8 describes the fabrication flow of the cap wafer process using the aMEMS process.

Wafer level hermetic packaging of the resonating structure is performed at the end of the process of the sensor substrate and SOI cap substrate. Anodic bonding technique (Figure 3.8.f) is applied for the hermetic sealing of the sensor wafer. Figure 3.8 presents the production steps of SOI cap wafer and hermetic encapsulation process.

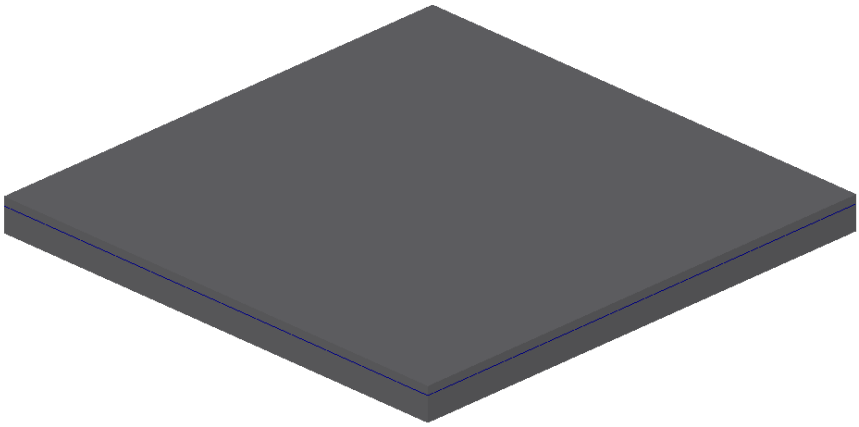

(a) Blanck SOI cap wafer(100µm device layer, 2µm buried oxide, 300µm handle layer thickness)

Figure 3.6: Fabrication steps of packaged resonator.

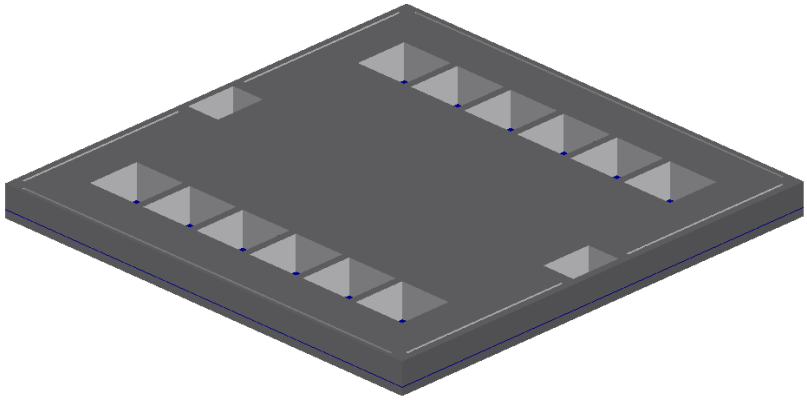

(b) Construction of the via openings on the handle layer

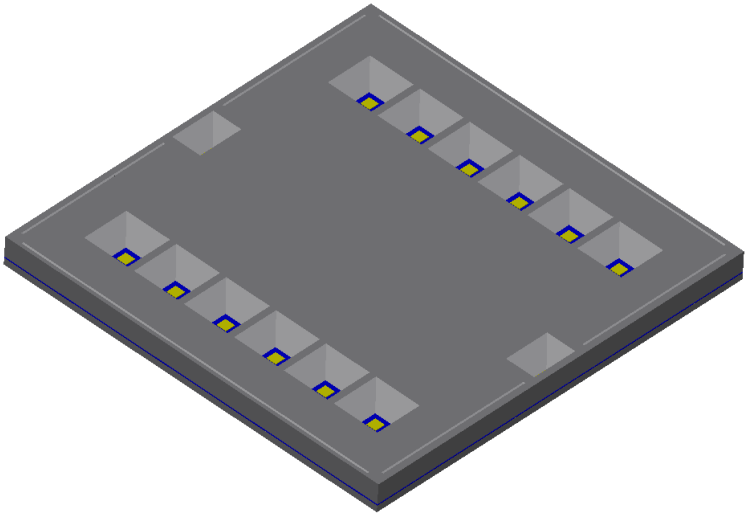

(c) Construction of the wire bonding pads

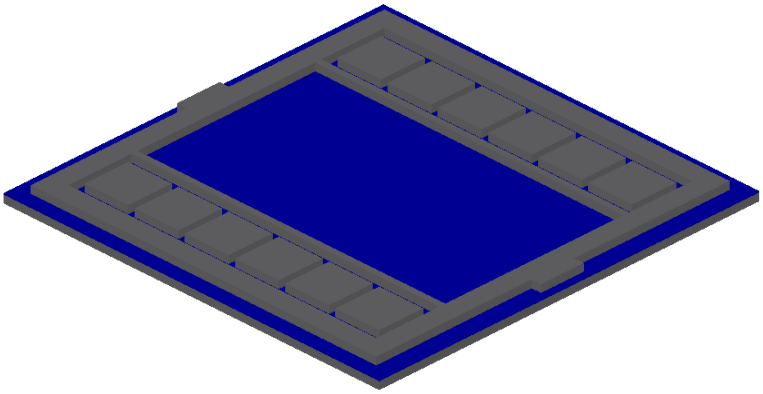

(d) Construction of the cavity, vertical feedthroughs and sealing walls on the device layer

Figure 3.7: (continued)

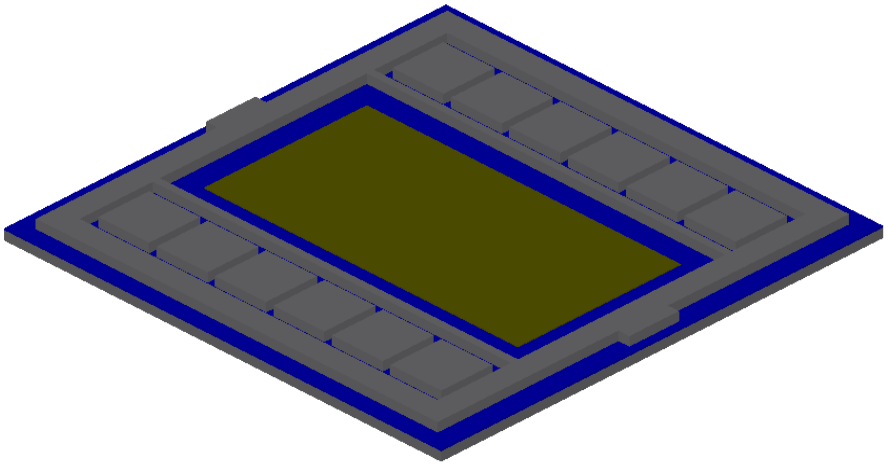

(e) Thin film getter deposition

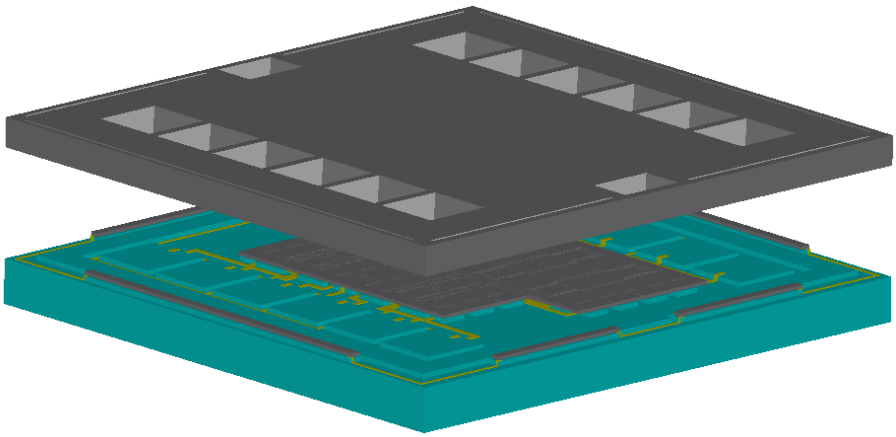

(f) Anodic bonding of cap and sensor wafers for wafer level hermetic packaging

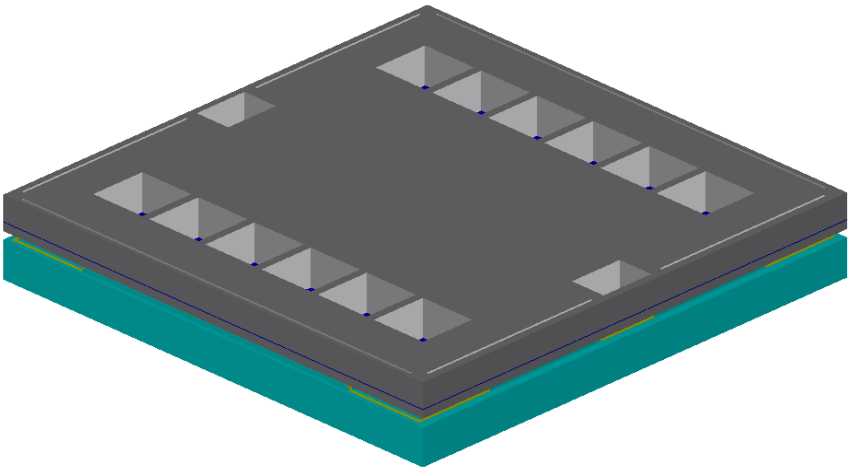

(g) Final view of the wafer level packaged resonator wafer

Figure 3.8: (continued)

3.3 Fabrication Results

There are various fabrication problems coming from mask production, lithography and DRIE etching; respectively even though all the process steps are optimized while the production of the encapsulated sensor wafer. The most significant process fault is the loss in the critical resonating structure dimension. To illustrate, the lithographic tolerances and the undercut during the DRIE step of the structure mask reason an undercut in the widths of the springs and fingers. The undercut in the finger tolerances directly affects the sensitivity. Similarly, the change in spring dimensions directly affects the mechanical resonant frequencies of the resonators. Figure 3.9 presents the SEM results of the different type of springs used in the MEMS resonators. After the fabrication, the widths of the springs are observed to be much thinner than the investigated value as given in Figure 3.9. However, these effects are estimated while designing the 8 different resonators so the mechanical resonance frequencies of the different resonator types are investigated considering the fabrication imperfections. Therefore, the variations in the spring widths do not dramatically affect the characteristics of the resonators. The gap spacing of the capacitive fingers becomes wider at the end of the processing. Figure 3.10 shows the SEM pictures of the varying gap and varying overlap type fingers after the fabrication. Figure 3.11 shows the SEM picture of the fabricated different type of resonators in a die. Figure 3.12 represents the SEM image of the fabricated MEMS resonator die, including the details of the via openings and feedthroughs.

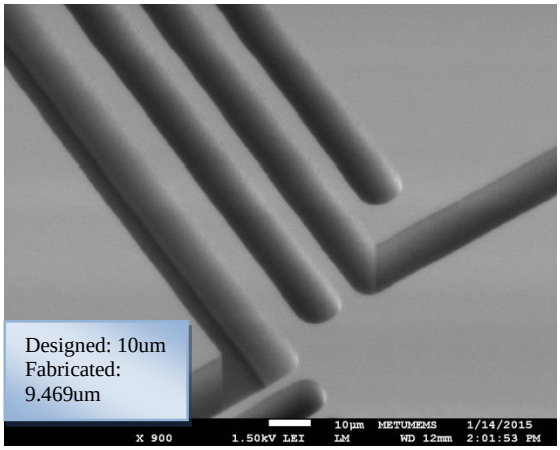

(a)

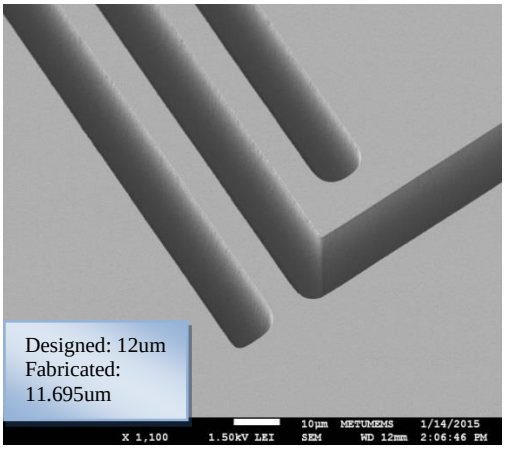

(b)

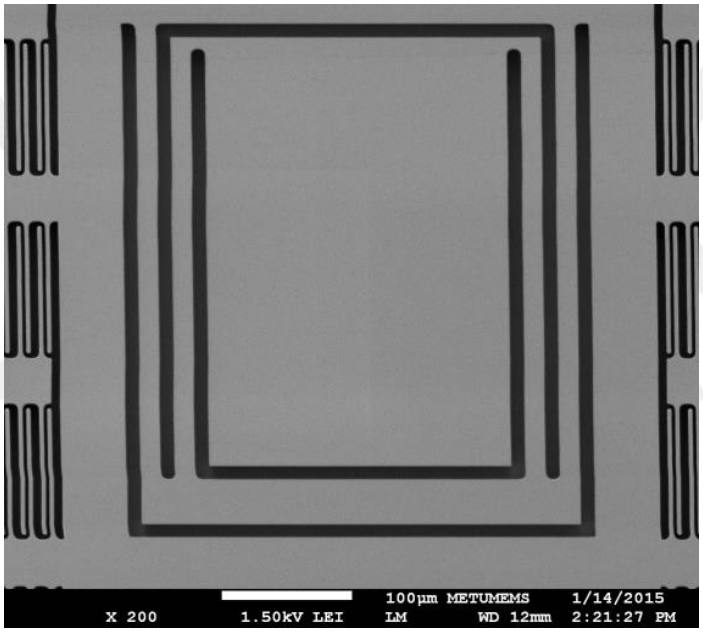

(c)

Figure 3.9: SEM pictures of (a) close-up view of folded spring type for Design-1, (b) close-up view of folded spring type for Design-2, and (c) general view of designed springs after the fabrication.

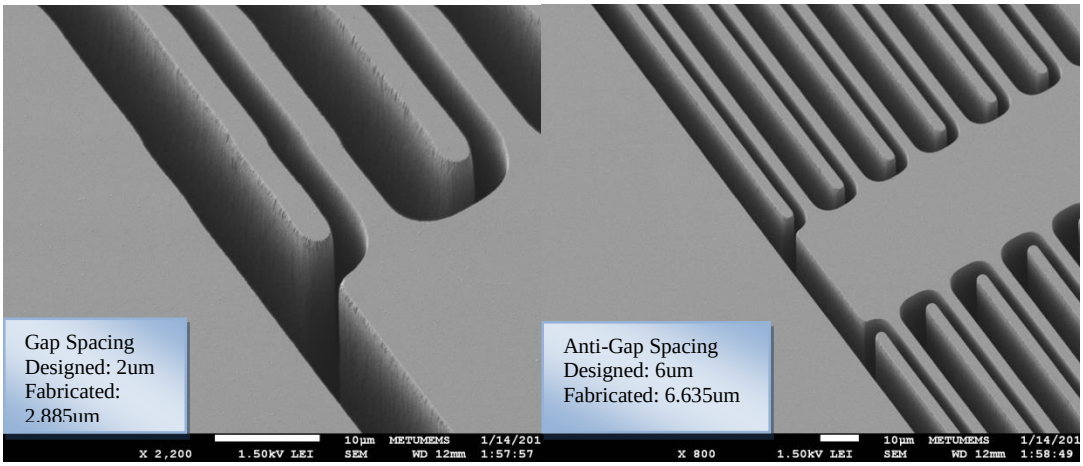

(a)

(b)

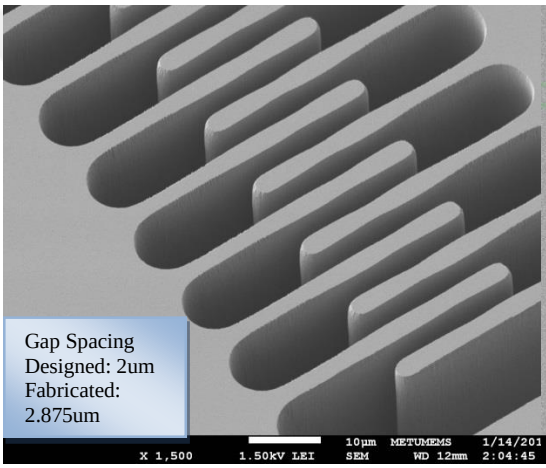

(c)

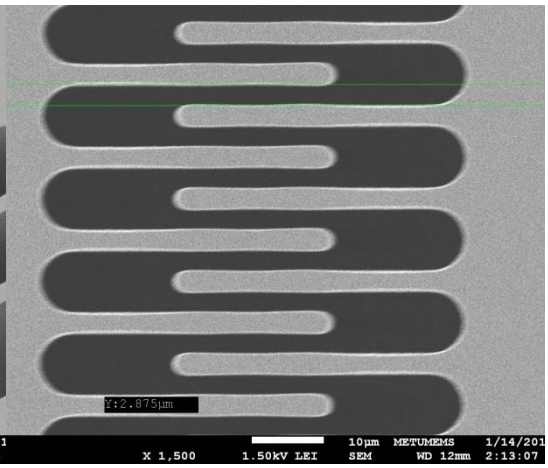

(d)

Figure 3.10: SEM pictures of different type of fingers (a) close-up view of Design-3, (b) general view of Design-3, (c) general view of Design-1, and (d) close-up view of Design-1 after the fabrication.

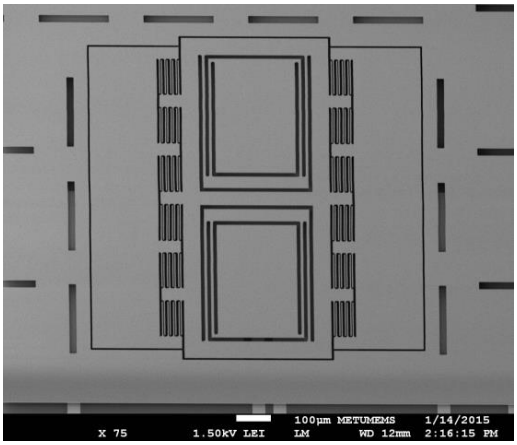

(a)

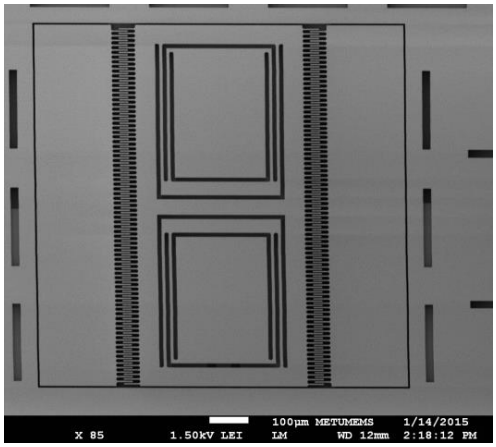

(b)

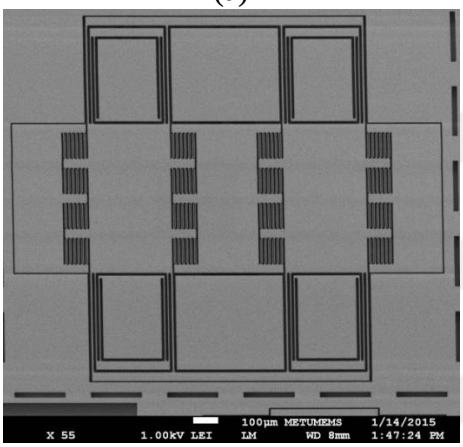

(c)

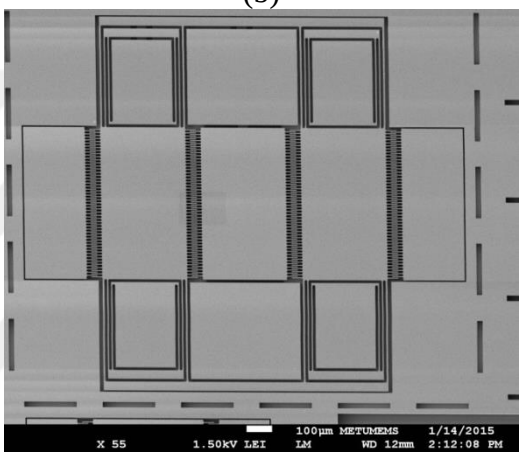

(d)

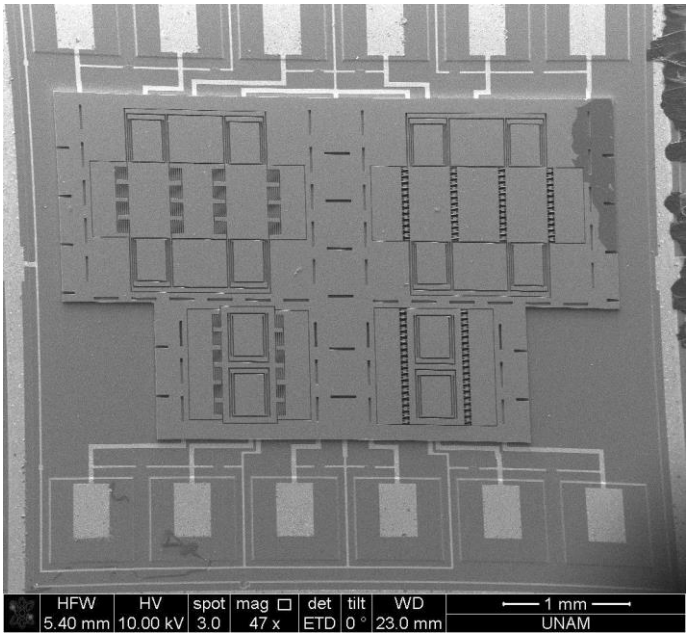

(e)

Figure 3.11: SEM picture of the fabricated sensors (a) Design-3, (b) Design-1, (c) Design-7, (d) Design-6 (e) general view of fabricated sensors in the same die.

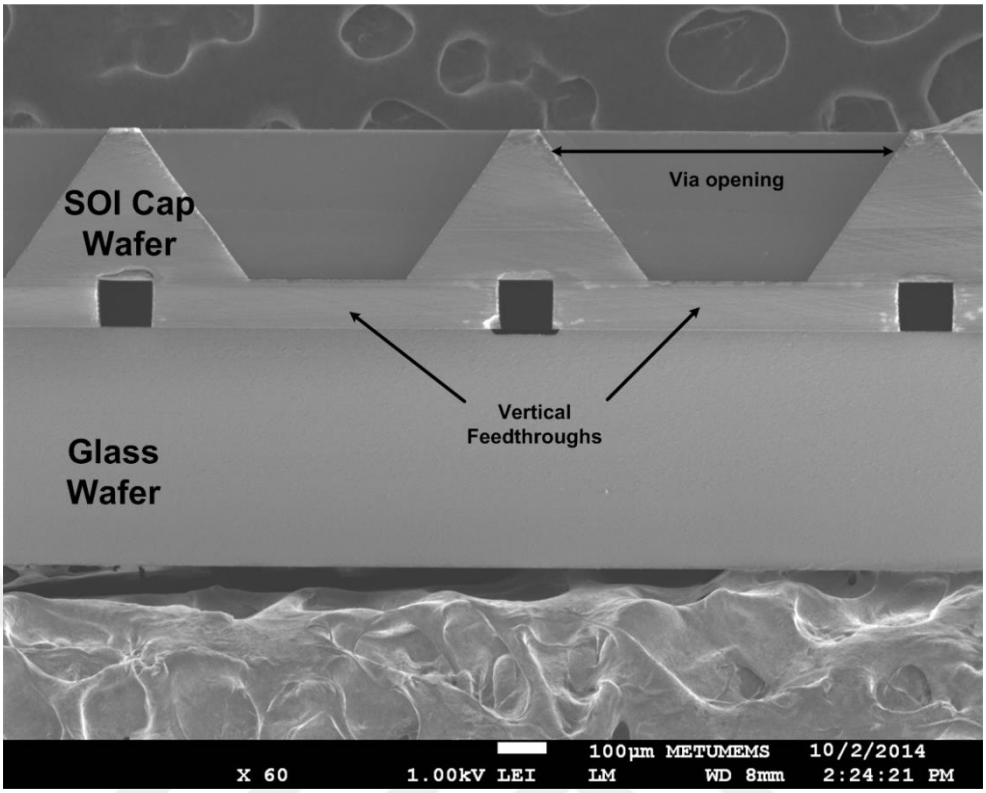

Figure 3.12: SEM picture of the encapsulated die presenting the details of vertical feedthroughs and via openings [40].

3.4 Summary of the Chapter

At the beginning of this chapter, the process of the sensor wafer with applying the M-SOG technique is described. Secondly, the wafer level hermetic encapsulation processes of the sensor wafer are discussed in detail for anodic bonding based on the *aMEMS* process. Finally, the fabrication results are discussed in terms of the comparison of the designed and measured parameters of the resonators.

CHAPTER 4

READOUT ELECTRONICS FOR MEMS RESONATOR SENSORS

This section presents the details of readout electronics for micromechanical resonators studied in the scope of this thesis. The organization of this section is as following; Section 4.1 provides the detailed information of the front-end electronics which transfers the output current of the sensor to the voltage. Section 4.2 provides the detailed information of the controller electronics design. Section 4.3 describes the drive mode controller design for MEMS resonators. Section 4.4 gives information about the constructed SIMULINK model and tabulated form of the controller values. Section 4.5 presents the designed and fabricated glass substrate for readout electronics of MEMS resonators, and their integration. Finally, Section 4.6 concludes briefly the chapter.

4.1 Read-out Electronics

The front-end electronics aims to convert the output current of the resonator to the voltage. Besides, it is amplified to a desired signal level by a preamplifier and instrumentation amplifier. For that purpose, a trans-impedance amplifier (TIA), which shows low input impedance to the output of the sensor and prevents signal loss during the conversion, is used. In addition to that, the TIA is insensitive to parasitic capacitances and contact resistances. Figure 4.1 represents the schematic of the TIA implemented in the scope of the thesis.

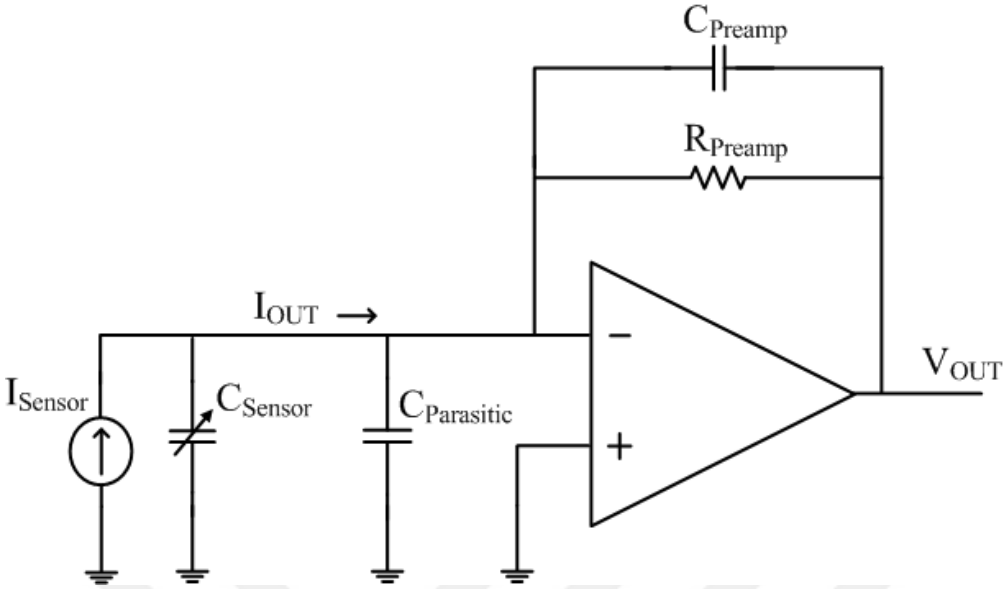

Figure 4.1: "Schematic of the trans-impedance amplifier implemented in this work." [50].

The input-output relation of the TIA can be expressed as in the Equation 4.1,

$$\left|\frac{V_o(s)}{I_o(s)}\right| = Z_{pre} = \frac{R_{pre}}{1 + sC_{pre}R_{pre}} \qquad 4.1$$

In the Equation 4.1, the multiplication of $sC_{pre}R_{pre}$ shows either the TIA is resistive or capacitive.

Resistive type is used in the motor mode considering the design considerations. "In the resistive type preamplifier, the function of the capacitor connected parallel to the resistor is to compensate the parasitic effects coming from the sensor and op-amp, which significantly improves the stability of the drive mode oscillation." [50]. The drawback of the resistive type is to obtain high gain is complex since the noise of the mechanism increases with increasing resistance.

4.2 Read-out Controller Design for MEMS Resonators

A controller is needed for closed loop self-oscillatory resonating system in terms of temperature compensation and carrier generation. The controller for the proposed

system is consisting of a demodulator, a low-pass filter, an instrumentation amplifier, and a PI controller.

4.2.1 Modulator

"The modulator and demodulator used in this work is a simple switching modulator." [51]. All of the details could be found in [52]. The circuit diagram of the modulator block is given in the Figure 4.2.

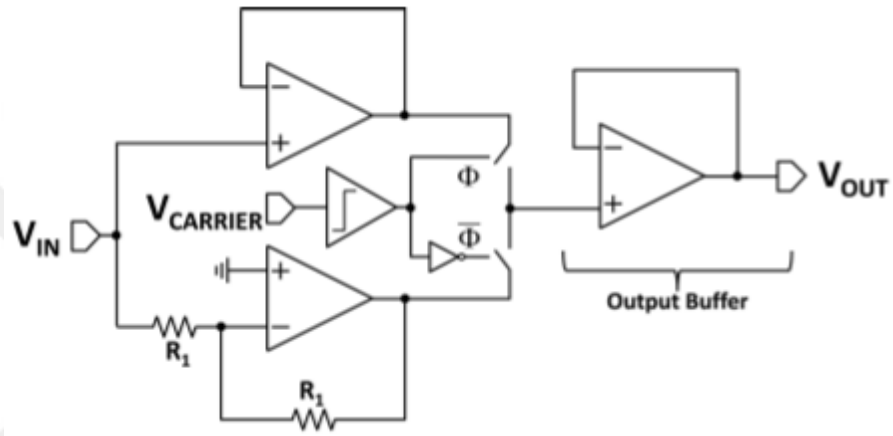

Figure 4.2: The circuit diagram of the modulator used in the thesis [52].

4.2.2 Low-Pass Filter

The usage of the low pass filter is for rejecting higher harmonics caused by the demodulation. Moreover, they could be added with passive elements, but the necessary capacitance and resistance values are quite high. On the other hand, active filters do not need such high values and they could easily give gains. Most popular active filter types are multi feedback topology (MFB) and Sallen Key filters and those have the benefit of component tolerance. In the MEMS resonator, the gain of the low pass filter is critical, since it determines the amount of the deflection. Because of the fact that, low pass filter gain offers changing of the oscillation amplitude of the resonator. However, the low pass filter gain only affects the loop gain, which could be also obtained by the controller gain.

4.2.3. PI Controller

PI controller consists of a single Op-Amp, one capacitor, and two resistors. Figure 4.3 represents the circuit diagram of the PI controller used in the scope of this study; whose parameters are derived in the Equation 4.2 and Equation 4.3, respectively.

$$K_P = -R2/R1 \quad 4.2$$

$$K_I = -1/CR1 \quad 4.3$$

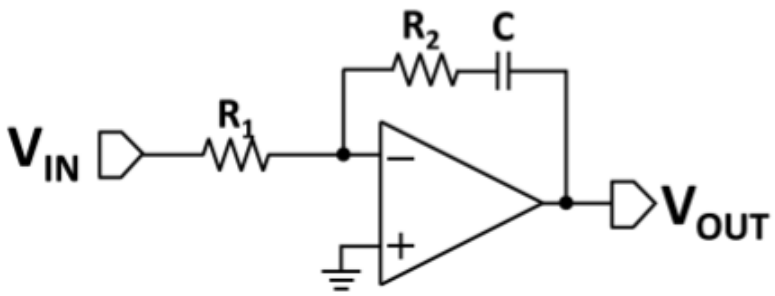

Figure 4.3: The circuit diagram of the PI Controller [52].

4.3 Open Loop and Close Loop Characteristics of MEMS Resonators

Before designing the closed loop drive mode controller, it would be better to analyze the open loop characteristic of the MEMS resonators by the resonant tests in order to achieve the sensor variables ranging from the resonant frequency, quality factor, to gain. Briefly, the open loop test offers the input-output ratio in the frequency domain. Figure 4.4 gives the simplified block diagram of the resonator test schematic. The performance of the resonator could be expressed in three blocks. In the first block, the actuation voltage is transferred to the actuation force by the driving electrodes. That is to say, with the help of Dynamic Signal Analyzer (DSA) a square wave is applied to the fixed electrodes and a force is produced. Then, the actuation force provides the displacement of the sensing electrodes. Finally, the displacement is converted to the

current by the capacitive sensing mechanism. The output of the sensor is the current, and this current is converted to the voltage by the preamplifier and instrumentation amplifier [50].

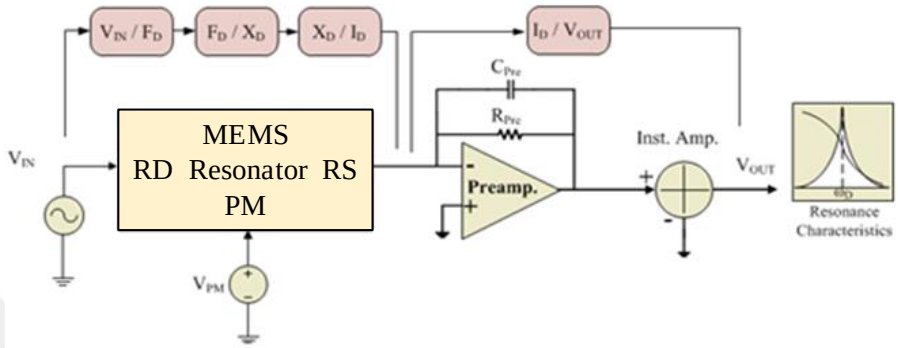

Figure 4.4: Simplified block diagram of the resonance test schematic.

The open loop transfer expression of the resonator could be defined as the multiplication of the conversion blocks as in the Equation 4.4:

$$\frac{V_{out}(s)}{V_{in}(s)} = \frac{F_D(s)}{V_{in}(s)}\frac{X_D(s)}{F_D(s)}\frac{I_D(s)}{X_D(s)}\frac{V_{out}(s)}{I_D(s)} \qquad 4.4$$

The open loop transfer expression of the resonator could be given by using the chip variables as depicted in the Equation 4.5:

$$\frac{V_{out}(s)}{V_{in}(s)} = V_{PM}\frac{\partial C_{RD}}{\partial x}\frac{1/m_R}{\left(s^2 + \frac{w_R}{Q_R}s + w_R^2\right)}V_{PM}\frac{\partial C_{RS}}{\partial x}sZ_{pre}A_{inst} \qquad 4.5$$

In the Equation 4.5, “the multiplication of driving $\frac{\partial C_{RD}}{\partial x}$ and sensing $\frac{\partial C_{RS}}{\partial x}$ sensitivity can be found by equating the resonance gain of the drive mode to the right side of the Equation 4.5. The mass of the motor mode m_R is obtained by the hand calculation using the design parameters of the resonating structure. The proof mass voltage V_{PM},

the preamplifier gain Z_{pre} and the instrumentation amplifier gain A_{inst} are known by the design. The resonance frequency w_D and the quality factor Q_R are obtained from the resonance test. After finding the multiplication of the $\frac{\partial C_{RD}}{\partial x}$ and$\frac{\partial C_{RS}}{\partial x}$, these terms can be calculated individually according to their ratio in the design [50]. Actually, the sensitivities of the resonator motor and resonator sense electrodes are symmetric so they are equal in the scope of thesis.

In the controller, the resonator displacement is set by the amplitude of the sensing signal; since the displacement is directly proportional with the noise. The larger the resonator displacement is the better the noise performance of the resonator; because the mechanical noise of sensor decreases according to the increase in displacement. On the other hand, adjusting the resonator displacement, the overshot in the controller output ought to be also analyzed for a safe operation. Besides, "the frequency variation with temperature is also critical issue while adjusting the displacement" [50]. Because the sensing signal stays constant instead of the displacement in Equation 4.6, any variation in the resonant frequency directly affects the amplitude of the displacement. But, a few Hz frequency shift is ignorable because the resonance frequency of the proposed resonating structures is around 15 kHz for one type and 45 kHz for other type.

$$V_{RS}\,(jw) = V_{PM}\frac{\partial C_{RS}}{\partial x} jw_R X_R Z_{pre} A_{inst} \qquad 4.6$$

"The design variables like the settling time overshoot and phase margin of the motor mode are set by analyzing the open loop response of the motor mode controller. The resonating structure has a second degree model but this model makes the analysis very complicated. Instead, the resonator dynamics between the modulator and demodulator is simplified to a first order system which is the enveloped model of the modulated system" [50] as in the Equation 4.7:

$$H_R\,(s) = \frac{A_R}{1 + s(2Q_R/w_R)} \qquad 4.7$$

where A_R is the resonant gain of the resonating structure including the front-end electronics, Q_R is the quality factor, and w_R is the resonance frequency of the resonator.

The cut-off frequency of the filter is set to 100 Hz for the resonator. The gain of the low pass filter is adjusted considering the resonator displacement. The open loop transfer expression of the controller could be defined as

$$H_{OL}(s) = \frac{A_R}{1 + s(2Q_R/w_R)} K_{Demod} H_{LPF}(s) \frac{K_I(1 + sK_P/K_I)}{s} K_{Mod} \qquad 4.8$$

"where $H_{LPF}(s)$ is the transfer function the low pass filter, K_{Mod} and K_{Demod} are the gain of the modulator and demodulator, respectively. Besides, K_I and K_P are the integral and proportional gain of the PI controller. After the pole-zero cancellation, the open loop transfer function of the resonator becomes a third order system which has totally three poles." [50].

After analyzing the open loop characteristics let's have a look at the closed loop operation of resonator. The operation of the resonator circuitry is relied on an amplitude controlled positive feedback mechanism. Notice that the quality factor of the resonator able to reach to a few tens of thousands in vacuum; therefore, it simply transfers the self-oscillation by locking its resonant frequency with the aid of the positive feedback mechanism. After that, with the help of the amplitude control system, the amplitude of the resonator oscillation is set to a certain level.

In this system, first of all, the signal is collected from the preamplifier and demodulated by again itself. A resistive type preamplifier is preferred in the system for minimizing the phase error coming from the modulator and demodulator. The output of the demodulator goes through a second-degree low pass filter to achieve the DC part of the demodulator signal which presents information about the level of the resonator displacement. The output of the low pass filter is compared with a reference DC voltage to adjust the amplitude of the resonator displacement. In this step, a band gap reference is used as the reference voltage because the output of the band gap reference is quite insensitive to environmental variations; thus, in that way, the resonator oscillation is kept constant over time. Then, the error signal is fed to a PI

controller which stabilizes the circuit by diminishing the error signal. The DC output of the PI controller is modulated with the motor sense signal. The modulated motor signal is a square wave because of the switching type modulator. Since the system is a high-Q system in vacuum, it behaves like a sharp band-pass filter. Thus, all other harmonics except the first harmonic of the square wave is rejected by the circuitry [50]. As a result, the amplitude controlled self-oscillation is achieved at the resonance frequency. The Figure 4.5 summarizes what described in the above.

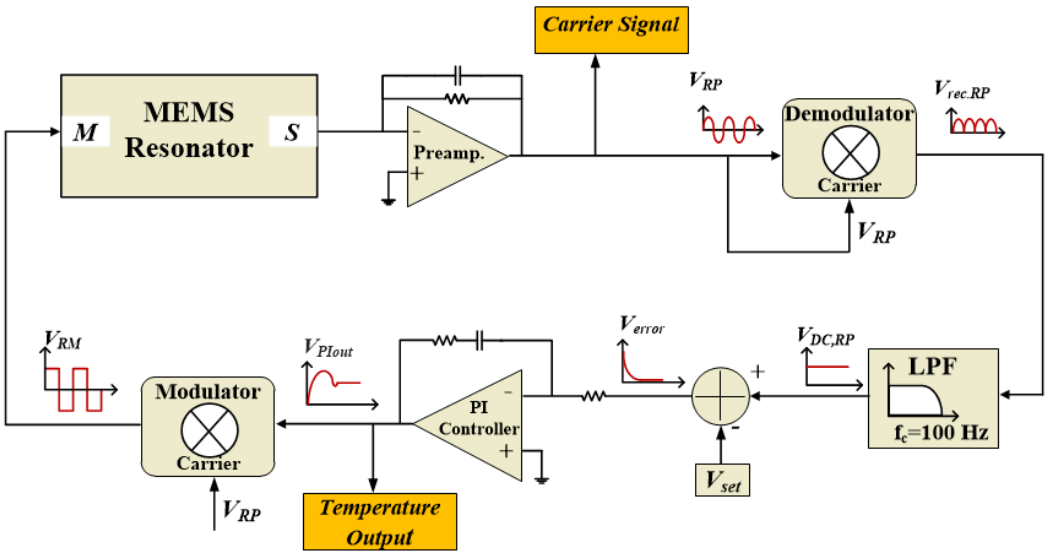

Figure 4.5: The scheme representing the block diagram of the closed loop resonator controller circuitry.

There are significant design considerations which affected the stability of the mechanism at the same time constructing the closed loop resonator read-out circuitry. These design variables are settling time, phase margin, overshoot and steady-state error; respectively. The response time of the system is determined by the settling time so it ought to be decreased for a high performance resonator. Besides, it would be better to have minimum 60° phase margin in the system for reliability and stability purposes. The overshoot amount is also crucial in the closed loop resonator controller design since the resonator displacement ought not to exceed the maximum allowable range; otherwise, it may damage the resonator in permanent manner. The steady-state error in the controller output ought to go to zero after the mechanism is reached to settling time to obtain the desired resonator displacement, which is satisfied by an integral based controller.

4.4 Closed Loop Resonator Simulink Model for Control Electronics

The systems parameters of the Design-1 type resonator are obtained through the open loop resonance test are tabulated in Table 4.1.

Table 4.1: The model parameters of the Design-1 type resonator used during the one of the design of the closed loop controller for 10 V_{PM} .

Model Parameters	Value
Resonance Frequency (f_R)	14262 Hz
Resonance Gain (A_R)	43.4dB (147.27)
Quality Factor (Q_R)	143000

The transfer expression in Equation 4.9 could be derived with the real sensor and controller parameters for Design-5 as,

$$H_{OL}(s) = \frac{54.32}{1 + s(1/0.71)} * \frac{2}{\pi} * \frac{1.625 * 403770}{s^2 + 1274s + 403770} * \frac{K_I(1 + sK_P/K_I)}{s} * \frac{4}{\pi} \quad 4.9$$

As seen in Equation 4.9, “the factors of 2/π and 4/π are the RMS value of the rectified resonator sense signal and the first harmonic of the square wave resonator motor signal, respectively” [50]. After a few iterations in MATLAB, K_P is optimized as 4.22 and K_I is optimized as 1.92 to obtain the sufficient phase margin, minimum settling time and minimum overshoot for the design.

The settling time and overshot of the closed loop resonator system are achieved by verifying the step response of the open loop transfer function in MATLAB. Figure 4.6 shows the closed loop step response of the resonator controller and carrier signal achieved by applying the realistic SIMULINK model of the resonator control electronics.

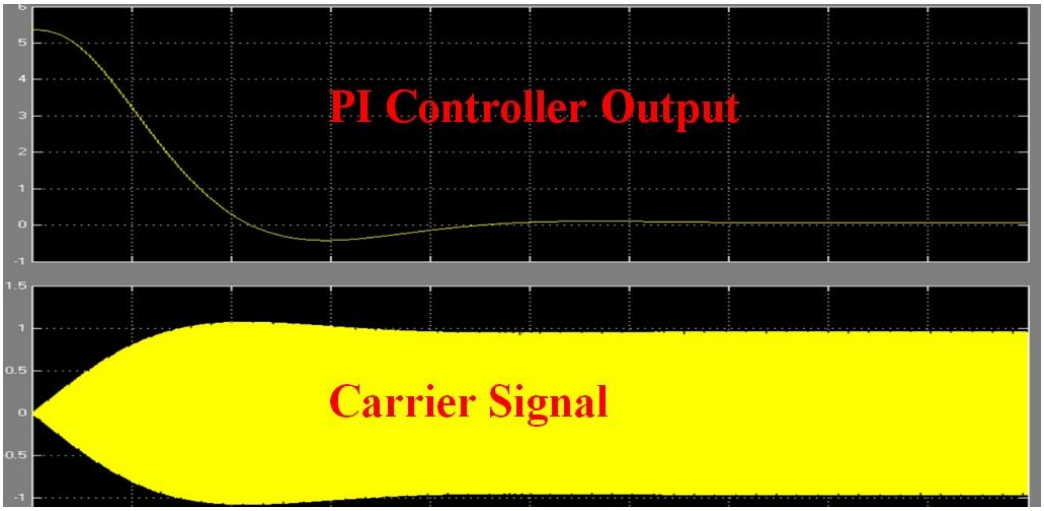

Figure 4.6: The closed loop resonator's step response controller and carrier signal obtained using the realistic SIMULINK model of the resonator control electronics.

The transient characteristics of the closed loop resonator control system are verified in MATLAB SIMULINK by verifying the system with the real sensor and controller values. Figure 4.7 presents the SIMULINK model of the closed loop resonator controller circuitry.

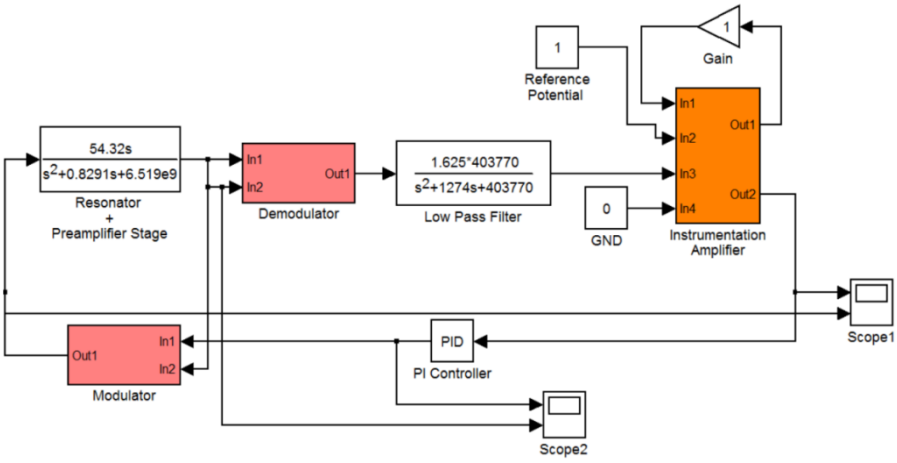

Figure 4.7: SIMULINK model of the closed loop control electronics for the resonator of Design-5.

Table 4.2: The necessary controller values of the resonators for temperature sensing of accelerometers:

Sensor Id	Sensor Type	V_{PM} (V)	Capacitor (μF)	R_1 (kΩ)	R_2 (kΩ)
0306	Design-1	10	2.2	715	931
0406	Design-2	10	1	33.2	340
0909	Design-3	3	1	154	549
1106	Design-4	3	1	56.2	249
1112	Design-5	10	2.2	237	931
0614	Design-6	10	1	44.2	432
0806	Design-7	3	10	249	590
0602	Design-8	1	1	6.65	348

The amplitude controlled self-oscillation loop for all different resonator designs are modelled using real sensor and circuit parameters in SIMULINK as in Figure 4.6. This model is necessary because by using this model, the controller parameters of the system can be easily optimized, and the closed loop system behaviour is analysed. SIMULINK simulations are performed by applying pole zero cancellation method. After making simulations for all 8 different types of sensors, the relative controller values are found. Table 4.2 shows the necessary controller values of the resonators for temperature sensing of accelerometers.

4.5 Integration of MEMS Resonator Sensors with Readout Electronics

There are eight different types of resonator sensor designs used in this study. All are in terms of sensor and readout circuitry designed and fabricated at METU MEMS Research and Application Center. As discussed previously, SIMULINK model is necessary because by using this model, the controller parameters of the system can be easily optimized, and the closed loop system behavior is analyzed. Furthermore, the

consistency between the LT Spice model and SIMULINK model has been achieved. As a result, in the Spice model, the controller parameter was optimized, and the self-oscillation loop was successfully operated. Figure 4.8 presents the constructed Spice model.

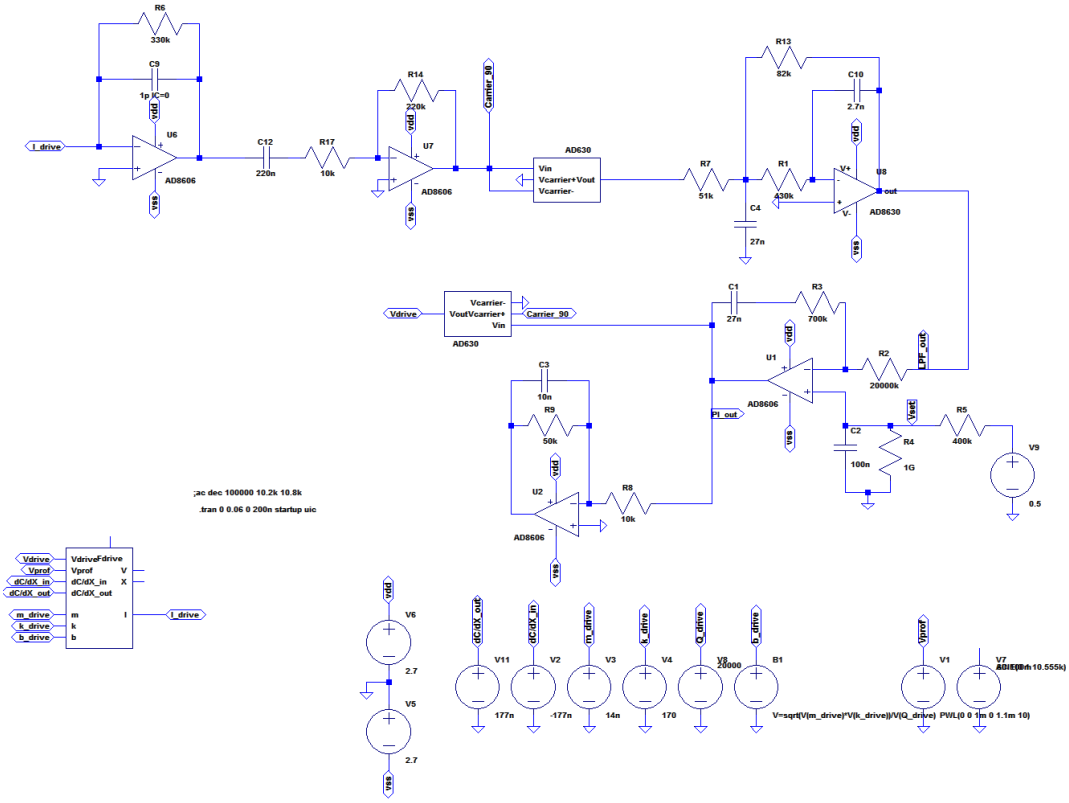

Figure 4.8: The image of the constructed Spice model for readout electronics simulations of resonator designs.

After fabricating the resonator chips and completing the readout simulations, a convenient glass substrate PCB layout is designed in L-Edit Software for testing purposes. Figure 4.9 presents the image of the designed glass substrate PCB layout by using L-Edit software including information about pin out labels and values of passive components (capacitors and resistors). All the passive components and integrated circuits (ICs) constructing resonator readout circuitry are combined a 16-pin, dual in line (DIL) metal package by Schott Corporation with its silver cap which is used as Faraday Cage. The fabrication of the glass substrate PCB layout is also completed at

the METU-MEMS Research and Applications Center using 4” glass wafer as the substrate; chromium and gold as the buffer and conductive material. Figure 4.10 presents the image of the fabricated glass substrates with all the components attached to a commercially available 16-pin hybrid platform package. All the components are mounted on the glass substrate with solder paste as the glue between the gold lines and the component legs by using pick-and-place machine. The glass substrate is placed over the base of the 16- pin package by means of silver epoxy. Finally, after placing the resonator chip to glass substrate by silver epoxy, some additional electrical connections of the components placed on the glass substrate are achieved through the wire-bonds.

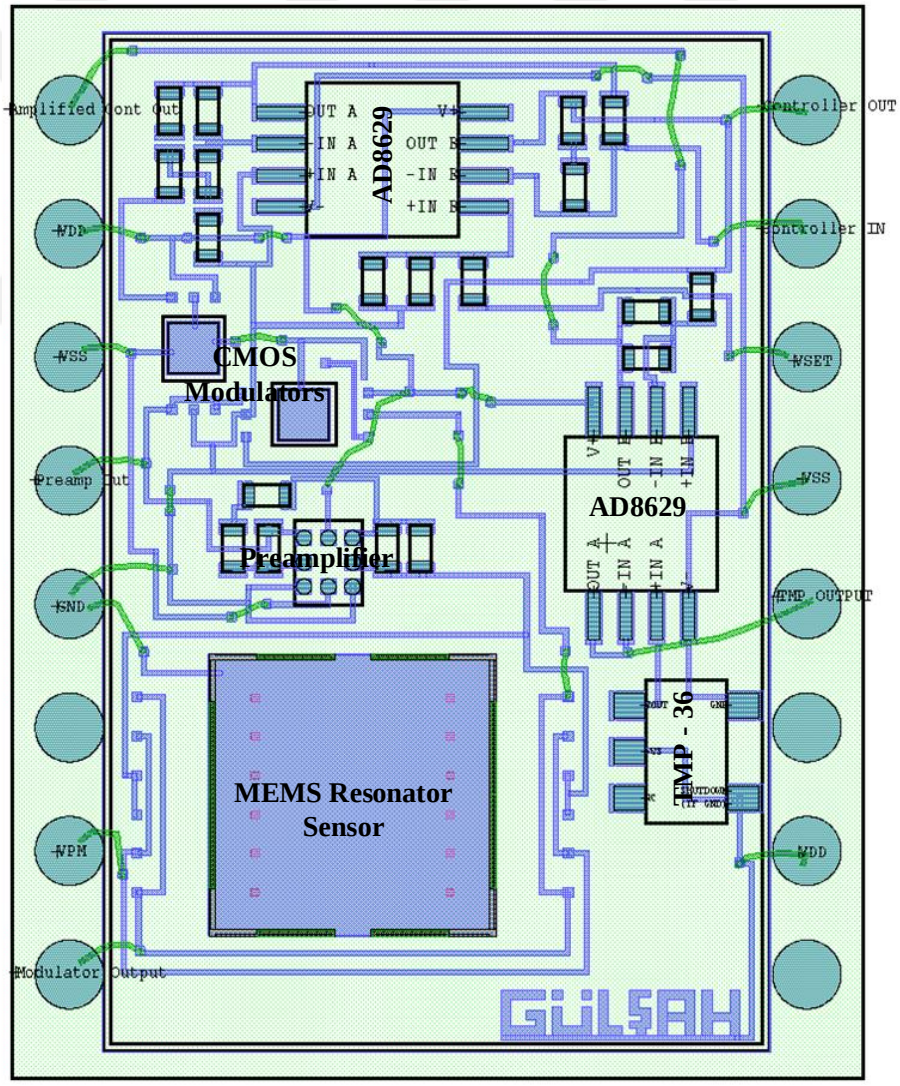

Figure 4.9: The image of the designed glass substrate PCB layout by using L-Edit software, representing the places of the wire bonding (green lines).

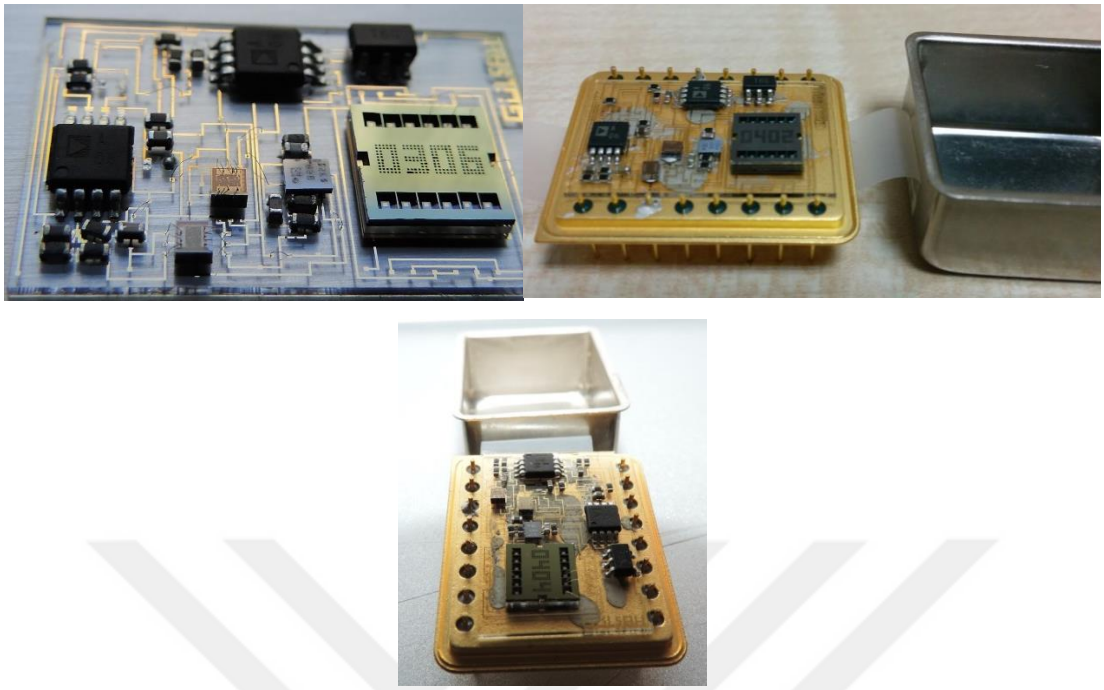

Figure 4.10: The picture of the fabricated glass substrates with all the components attached to 16-pin package.

In the first stage of the tests, a breadboard is used. However, it is observed that the breadboard is not so much reliable and a circuit board is preferred. Therefore, a circuit board for both open loop and closed loop tests is prepared. Figure 4.11 shows the picture of the circuit board prepared for the resonator temperature tests.

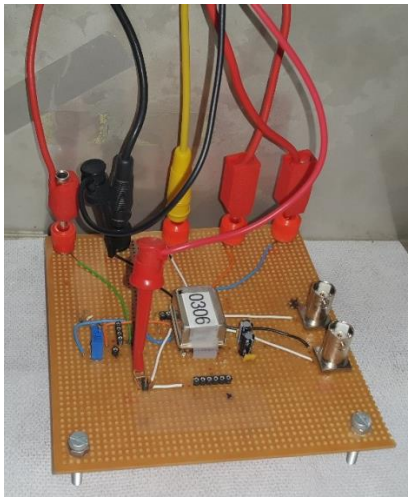

Figure 4.11: The image of the circuit board prepared for the resonator temperature tests including resonator Design-1 package.

4.6 Summary

This chapter summarizes the design of controller electronics for MEMS resonators for the temperature compensation. The chapter starts with the Section 4.1 in which the front-end electronics are described in detail. After describing the front end electronics, Section 4.2 presents the resonator controller electronics ranging from modulator; low pass filter to PI controller is mentioned. In section 4.3, firstly, the resonator controller design is given for MEMS resonators then their working principle and functionality is emphasized. Section 4.4 includes the SIMULINK model and simulation results. Besides, tabulated form of the PI controller values for all 8 different resonator designs are analyzed in this section. Section 4.5 describes the glass substrate PCB layouts which are designed to integrate the resonators with the readout electronics. Finally, Section 4.6 summarizes the chapter.

CHAPTER 5

COLLECTED DATA AND TEST RESULTS

This section shows the details of collected data and test results from resonators and accelerometers in the scope of this thesis. The organization of this section is as following; Section 5.1 provides the detailed information of data collection procedures applied in this thesis. Section 5.2 mentions the used techniques for compensation of temperature and acceleration effects ranging from moving average filtering, polynomial curve fitting to compensation of hysteresis and integration of compensation by applying polynomial curve fitting to resonators and accelerometers. Section 5.3 describes the detailed test results of resonators which consists of functionality tests, resonance test, correction of open loop temperature versus resonance tests with front end electronics and TCF values; and closed loop temperature versus controller output tests with front end electronics. Section 5.4 gives the detailed test results of accelerometers including interface circuitry and auxiliary tools; functionality tests, C-V Measurement tests and test results ranging from scale factor, offset and range, velocity random walk, bias instability, bias repeatability and temperature tests. Section 5.5 presents the detailed test results of integration of resonator and accelerometer packages including raw and compensated results. Finally, Section 5.6 gives a brief summary and concluding points of the chapter.

5.1 Data Collection Methodologies

"In order to observe the effects of temperature on a MEMS accelerometer g output, it is very significant to follow a set of rules for data collection, and maintain them for all the tests for convenient results." [7]. Notice that all the collected data is based on this thesis study, limitations related by the setup, and specifications of the chips.

5.1.1 Range of Temperature

Ideally in the literature for any temperature test range is from -40°C to 85°C and back to -40°C (for mostly industrial applications). For all type of resonators and accelerometer sensor packages tests are done from -20°C to 80°C range which is a suitable range for the Tenney Temperature Oven used during the tests and also, is a similar range to the standard commercial electronics operation range (0°C to+80°C).

5.1.2 Acceleration Range

There is a limitation for the acceleration range which could be measured with the available resources. This is mainly due to the lack of the defined equipment which could be applied to get large amounts of acceleration. In this work it is based on the natural range of +1g and -1g because of the gravitational force of the Earth.

5.1.3 Test Duration

One of the most important parameters is the duration of any sample for temperature and acceleration tests. The duration of data collection is not really significant; and the actual goal is to sample the data in the given range of temperature or acceleration. Notice that the similar range of temperature or acceleration could be obtained by applying varied time durations with various conditions. In this study the duration of these data collections varies from 5 minutes to 2 hours. It would be better to mention that the effect of duration of data collection is not affecting any compensation.

5.1.4 Number of Samples

To generalize the compensation methods, the data sets taken from each sensor are very significant. For those purposes more than 10 sets of data (for making sure they are repeatable) are collected from each sensor to verify the concept of this study.

5.2 Used Techniques for Compensation of Temperature and Acceleration Effects

In this thesis study for compensation of temperature and acceleration effects different techniques are used and this section discusses these techniques.

5.2.1 Moving Average Filter

The aim of using moving average filter in this study is to understand a relationship between resonator's controller output and other parameters such as temperature and acceleration. Just moving average filter itself cannot be used for temperature compensation purposes. It is one of the low pass filter types which removes high frequency noise and helps to visualize the trends of data. Figure 5.1 shows the raw data collected from both the temperature sensor and the controller output of the resonator. Most probably due to the high-impedance nodes occurring as a result of using controller passives out of the package, a strong 50 Hz coupling occurs on the raw controller output data. It can be seen that no relation can be established between controller output of the resonator and temperature because of high frequency noise. Figure 5.2 shows the digitally filtered and scaled controller and controller output data plotted over a 2-hour-long period. Correlation between the temperature and the controller output is obvious.

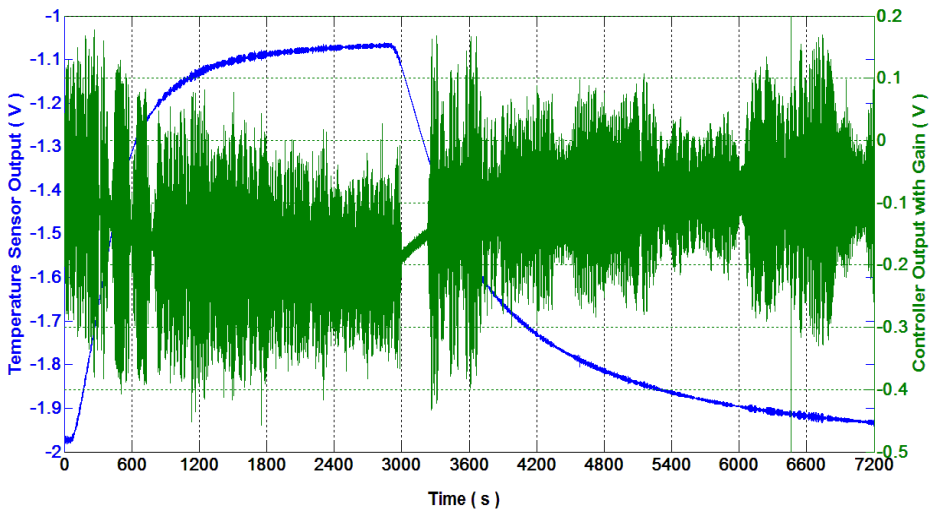

Figure 5.1: The raw data collected from both the temperature sensor and controller output of the resonator Design-5.

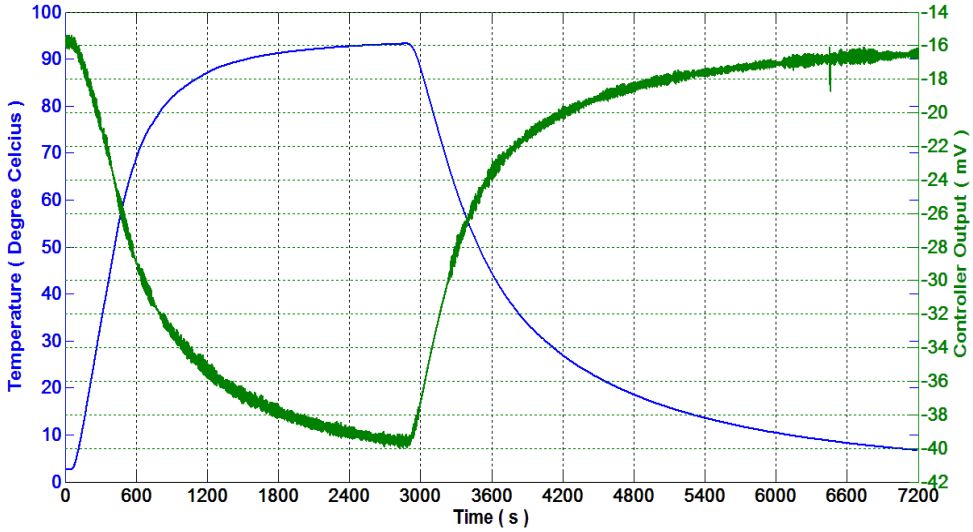

Figure 5.2: The digitally filtered and scaled temperature and controller output data collected from resonator Design-5 plotted over a 2-hour long period.

5.2.2 Polynomial Curve Fitting

Under the scope of study for compensation of temperature effects polynomial curve fitting is preferred. This technique is the fastest and easiest method. The procedure is like that just the temperature is varied among the other environmental variables are kept constant with assuming that the controller output of the resonator just change with the temperature changes. It is important to mention that only temperature dependence is modelled by using this technique. For repeatability purposes equation is validated on different data sets and similar results are collected.

Besides, with different degrees of order equations same data can be modelled; just the difference is accuracy. That is to say, when the degree of polynomial is higher, the fitting accuracy of data is higher. Figure 5.3 represents the modelled data with different order polynomials (Design-8 (0602 ID, 50 kHz tuning fork varying gap type) resonator sensor's polynomial curve fitting results). When figure is analyzed first degree polynomial represents generalized behavior of temperature dependency whereas second degree fit shows estimated trend more precisely. Increasing the order of fits increases the accuracy and at the end of fifth order fit data is completely modeled.

The bias offset and turn on bias are other factors that can be considered about polynomial curve fitting. The turn on bias is measured when sensor is turned on and observed as a constant in a polynomial expression and its value is a bit changeable when each time the sensor is turned on. Figure 5.4 summarizes the concept.

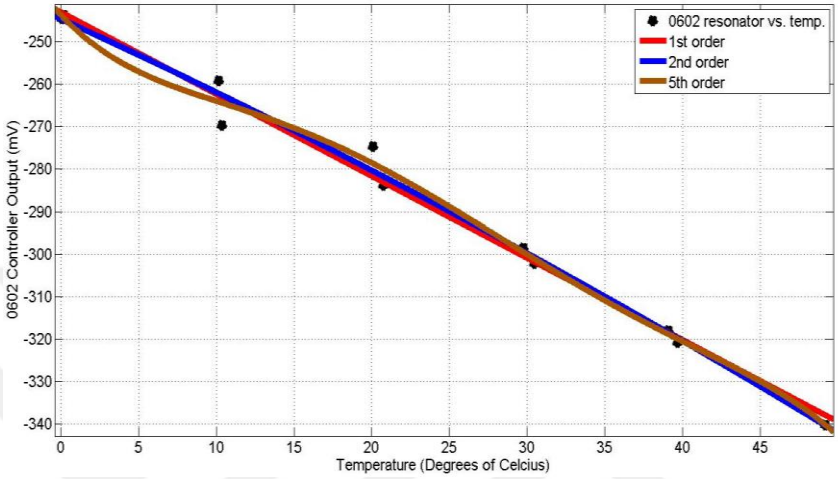

Figure 5.3: The graph showing the Design-8 (0602 ID, 50 kHz tuning fork varying gap type) resonator sensor's polynomial curve fitting temperature versus controller output result. Higher the accuracy of curve fitting, higher the degree of polynomial and designer can decide the accuracy and speed.

$$Offset = -0.005606t^2 - 1.673t - 244.6$$

Temperature dependent part Turn ON Bias

Figure 5.4: The turn on bias is changed when each time a sensor is started up, whereas the relation between the temperature and the resonator's controller output remains constant.

5.2.3 Observation of Hysteresis

In this study hysteresis in a resonator's controller output data caused by temperature cycles analyzed. Notice that for the output to be more accurate hysteresis has to be removed from the resonator's controller output data. Again for hysteresis observation

polynomial curve fitting is preferred. Figure 5.5 represents occurred hysteresis in the resonator sensor's controller output, when the temperature is varied between -20°C to +80°C; in which the filtered and scaled data is divided into two parts in order to observe the correlation between the temperature and the controller output during heat-up and cool-down distinctly. Ideally in an environment where there are no hysteresis or phase considerations, the two plots should have overlapped. It must be noted that the two ends of the plots, where the temperature stability is high, coincide; but the transient period is not. In accordance with that, the reason for the non-linearity and different heat-up and cool-down behaviors might be a result of high settling time of the controller output (the oven heats up faster). The two curves shown in the plot are firstly modelled by CF technique and the two polynomials are obtained; then their difference is taken to get a difference polynomial function; as a result, a function related with temperature is obtained. In the second closed loop tests, again the DAQ to sample data is used at 250Hz for 5 minutes and during this duration the oven is heated to +80 ˚C then it is cooled to -20 ˚C; then again it is heated to +80˚C. Similar to previous test, the raw data is filtered and Figure 5.6 indicates the comparison of cooling down and heating up characteristics of the sampling conditions of 250 Hz 5 minutes for each points.

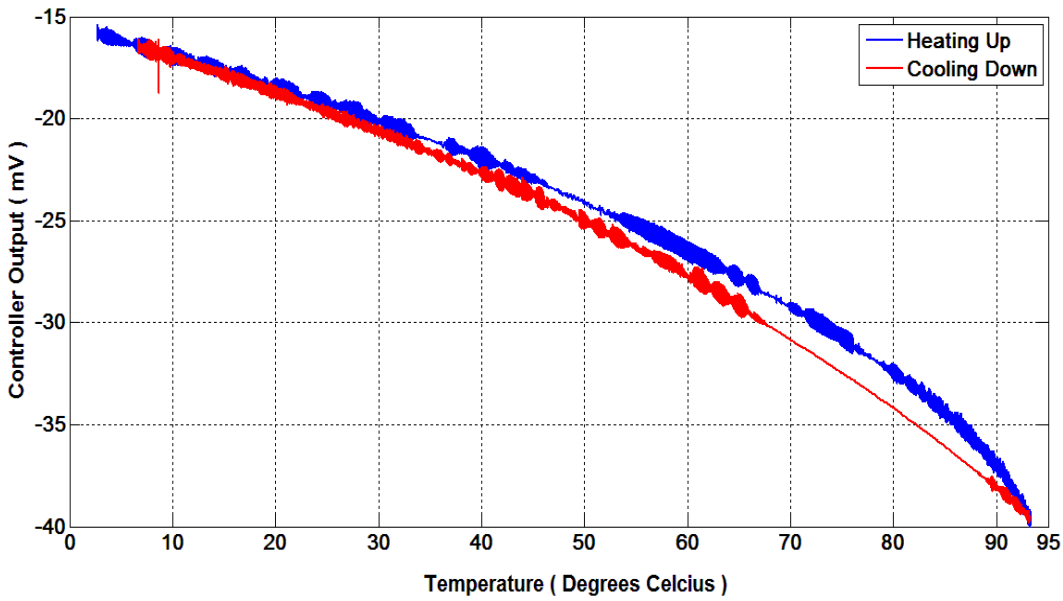

Figure 5.5: The comparison of heating up and cooling down characteristics of the sampling conditions of 100 Hz 2 hours.

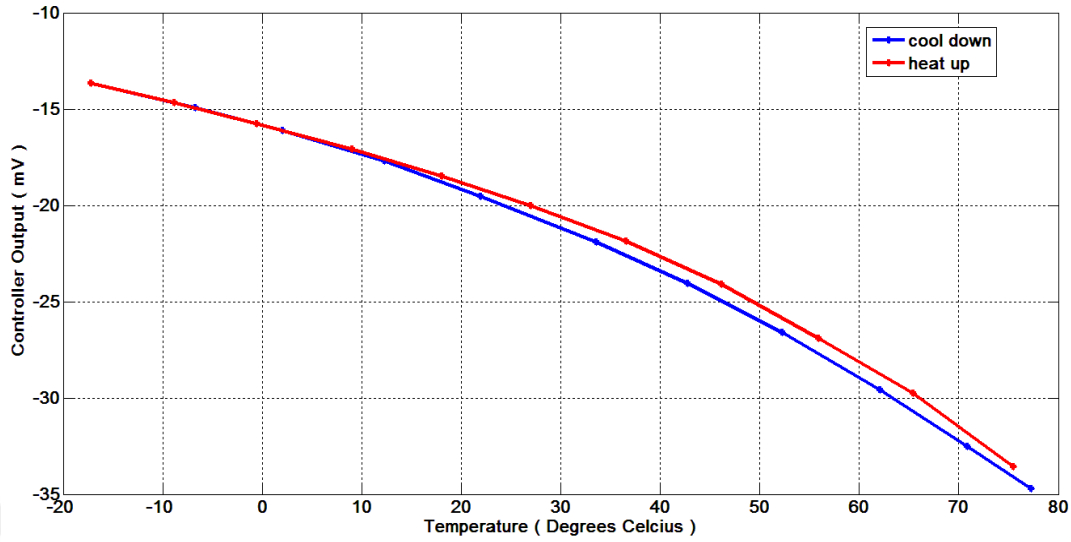

Figure 5.6: The comparison of cooling down and heating up characteristics of the sampling conditions of 250 Hz 5 minutes for each points.

As it can be analyzed from the figures controller output changes with temperature as 20mV/˚C.

5.2.4 Integration of Compensation by Applying Polynomial Curve Fitting

Under the heading of this part, the integration of temperature sensing compensation effects is discussed. Notice that previously discussed compensation methods could "be integrated in different orders to overcome the errors at the same time" [7]. Notice that the hysteresis compensation is integrated to the compensation of temperature in the following study.

By applying polynomial curve fitting for both acceleration output and temperature the data is filtered twice. In other words, the first filtering eliminates the offset because of the temperature and the second filtering remove the offset due to acceleration. Some advantages of this technique is varying from the simple expressions to product of various constants. Besides, this technique is appropriate for rapid processing the only thing that limits the speed is the computing power.

5.3 MEMS Resonator Sensors Used in the Study and Their Results

The eight different types of resonator designs are used in this study. Their theory and modeling is given in detail in Chapter 2. The fabrication criteria and process details are given in Chapter 3 and all the circuitry details are given in Chapter 4. Following heading gives the details of how the resonator circuitry is tested before performing the temperature tests.

5.3.1 Functionality Tests of the Designed Resonator Packages

Before starting to temperature tests it is significant to be sure that the resonator package which consists of produced resonator sensor and its circuitry is functional. To be sure that circuitry has to be tested block by block. Step by step preamplifier, gain stage, demodulator, low pass filter, modulator and temperature sensor are analysed and functionalities of all are checked. During the tests, in amplitude control due to high noise a problem is faced; Design-5 resonator sensor is locked another electronic mode which has 35 kHz resonance frequency. To solve this problem a capacitor is added to the 2nd gain stage is preventing to lock in an undesired electronic mode. For performing the functionality tests oscilloscope, power supply and function generator is needed. Following sub-headings describes how the functionality tests of blocks are performed.

5.3.1.1 Preamplifier Block:

In the functionality test, the voltage is given through the resistance so the current is given to the input of the preamplifier by using a resistor and signal generator (for a resistive preamplifier). Then, the output of the preamplifier stage is monitored to check the functionality of the preamplifier and gain op-amps. In this step, sine wave should be observed with the help of oscilloscope by observing the amplitude change we easily analyze whether it is working correctly or not.

5.3.1.2 Demodulator Block:

After monitoring the preamplifier block, the output of the demodulator is monitored. If the demodulator is functional, a rectified sinusoidal signal is observed at its output could be observed by oscilloscope.

5.3.1.3 The Low Pass Filter Output Block:

The low pass filter output should give a DC voltage which is multiplication ($\frac{2}{\pi}$), the gain of the low pass filter and the amplitude of the preamplifier output. The error signal on the device should be analyzed by the help of multimeter.

5.3.1.4 Controller Op-Amp Block:

To test the controller op-amp, it is configured in the inverting amplifier, and the output of it is checked in this configuration. For this test, the two resistors are selected with the same value and the set voltage is set to zero volt. By checking with the multimeter it is observed the same values with the negative signs.

5.3.1.5 Modulator Block:

The modulator should give a square wave if it is functional. Because it is proportional with the voltage of the inverting amplifier; again it is controlled by the help of oscilloscope.

In conclusion, above all steps verify that without integrating the resonator sensor package to the circuitry all the blocks are functional.

5.3.2 Resonance Tests

Before testing the closed loop drive mode controller, it would be better to analyze the open loop characteristic by the resonance tests to achieve the sensor characteristics in terms of the natural resonance frequency, quality factor and gain. Also for finding out the resonator controller values these test results are necessary.

After completing the functionality tests, the circuit is set according to resonator pads. In experiments one of the probes is for ground, one is for proof mass voltage, one for resonator sense pad and similarly one other for resonator drive pad. Notice that in experiments for varying overlap type sensors set voltage is 1Vpk and for varying gap type sensors set voltage is 250mVpk.

Figure 5.7 shows one of the resonance test result of designs named as Design-4 (1106 ID varying gap type sensor) sensor for being an example to the desired resonance characteristic.

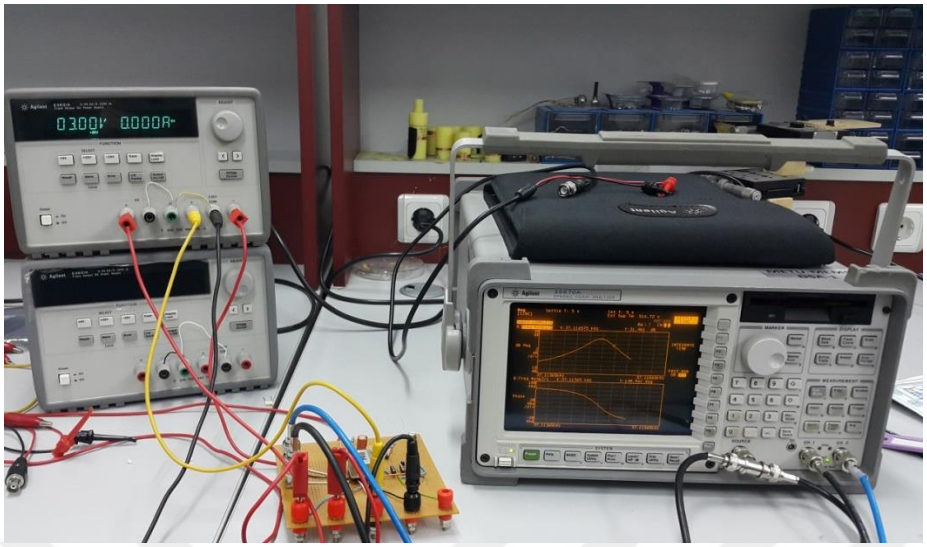

Figure 5.7: The picture showing the resonance test result of the Design-4 (1106 ID, varying gap type sensor in Table 5.1).

Table 5.1 shows the tested different type of sensors' resonance test results. Notice that the resonance tests were done in 5 Hz span, 1mV peak voltage and 5 seconds settle and integration times.

Table 5.1: The resonance test results of the designed resonators for temperature sensing of accelerometers:

Sensor Id	Sensor Type	V_{PM} (V)	Res. Freq. (KHz)	Gain (dB)	Q_R(/1000)
0306	Design-1	10	14.3	43.4	142,6
0406	Design-2	10	37.6	27.9	40,6
0909	Design-3	3	13.8	36.9	23,9
1106	Design-4	3	37.2	34.5	34,5
1112	Design-5	10	12.9	34.7	102,5
0614	Design-6	10	40.3	30.1	54,7
0806	Design-7	3	12.3	41.7	36,5
0602	Design-8	1	39.3	16.4	43,1

5.3.3 Resonance frequency vs temperature test results:

The effect of temperature is the first condition which needs to be tested. This section includes the details and comparison of resonance frequency vs temperature tests performed on hot plate and inside Tenney Oven; respectively.

5.3.3.1 Temperature Tests on Hot Plate:

After the wire bonding of the packages are completed, tests of the package with front end electronics at different temperatures are started from 20°C to 90°C with 10 degrees of Celsius increments. Hot plate is used for temperature settings and to settle the temperature to its exact value duration is nearly 20 minutes. The package is directly put on the hot plate and with the help of wires the connections through the breadboard is constructed; so the position of the package is never changed or moved. The real preamplifier values for the resonance tests are used. Table 5.2 shows the result of the Design-5 type resonator sensor on hot plate. After the calculation according to the Equation 5.1 the average TCF value is calculated as -85ppm/°K.

$$f = f0 + f * TCF * \Delta T \qquad 5.1$$

Table 5.2: The resonance test results of the Design-5 (ID#1112) resonator with front end electronics for temperature sensing of accelerometers with temperature variations: (Notice tests are constructed at 5Hz span, 1mV peak voltage and 5 second of integration and settling time).

Sensor Id	Temperature (˚C)	V_{PM} (V)	Res. Freq. (kHz)	Gain (dB)	Q_R
Design-5	20	10	12.874	35.4	114,432
Design-5	30	10	12.871	35.1	104,636
Design-5	40	10	12.860	33.7	257,198
Design-5	50	10	12.849	33.3	171,332
Design-5	60	10	12.836	34.4	114,101
Design-5	70	10	12.824	34.2	146,555
Design-5	80	10	12.808	33.9	102,464
Design-5	90	10	12.795	33.2	127,958

5.3.3.2 Temperature Tests inside Tenney Oven:

Alternatively, instead of bread board after completing the preparation of the test circuitry, tests of the resonator with its preamplifier at the range -25 ˚C to 120 ˚C is done at a temperature chamber which is named Tenney Temperature Oven. Needless to say, these observed effects can be studied on that sensor. The temperature controlled oven's location is in EE Department of METU. Figure 5.8 represents the temperature controlled oven which is used in the scope of this study.

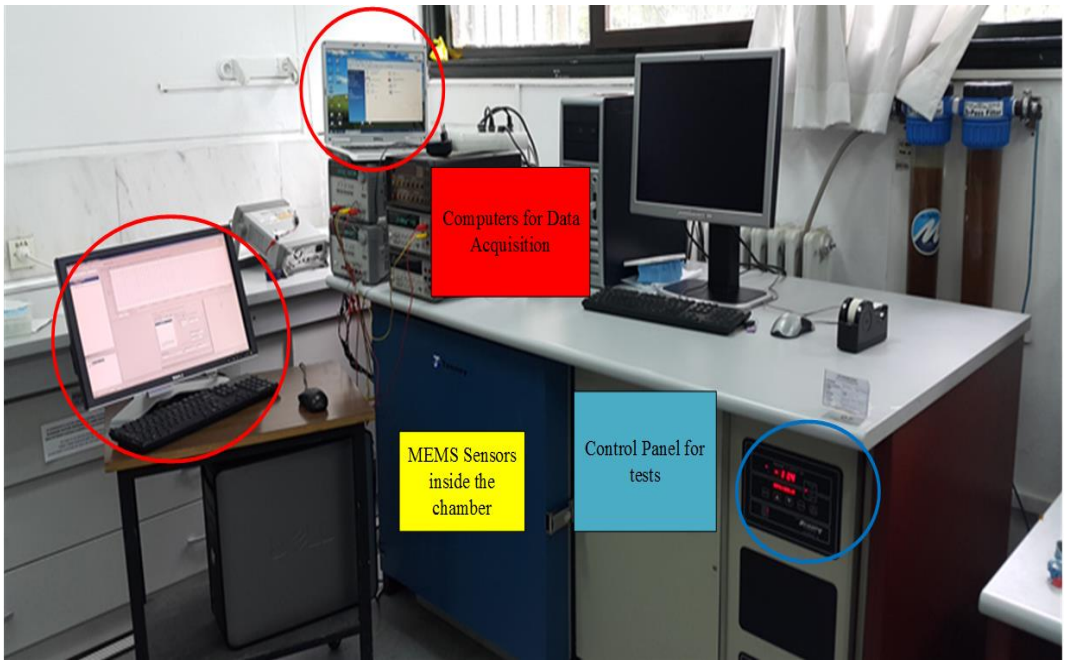

Figure 5.8: The Tenney Oven in which all the tests are conducted with data acquisition interface, placement of the MEMS sensor inside the temperature controlled oven and control module for controlling the test conditions.

The testing procedure is like that first of all, related with designed and fabricated resonator packages conventional readout circuitry is placed inside the Tenney oven; and the wires which contain the data come out of the hole which is placed left side of the oven and these wires are connected to the computers and power supplies as shown in the Figure 5.9.

Figure 5.9: The image showing the wires which contain the data come out of the hole which is placed left side of the oven and these wires are connected to the computers and power supplies.

Although the chamber is able to produce the temperature range from -80°C to 150°C for tests -25°C to 120°C range is preferred. While the oven is turned on the vibration problem is faced which causes a lot of noise while collecting the data. For those reasons different type of testing procedures are performed.

By using this oven hysteresis also checked by using the cycles of temperature from -20°C to 80°C and again to -20°C. Note that the higher temperature limit is set to the 80°C to prevent damage to the electronics and the connecters.

Compared with hot plate tests circuitry is improved and it is possible to check the package temperature with temperature sensor so these tests are more reliable. The average TCF value is found -130ppm/K. Table 5.3 shows the result of the Design-5 type resonator sensor on Tenney oven. After the calculation according to the Equation 5.1 the average TCF value is calculated as -85ppm/K.

Table 5.3: The resonance test results of the Design-5 (ID#1112) type resonator with front end electronics for temperature sensing of accelerometers with temperature variations on Tenney Oven: (Notice tests are constructed at 5Hz span, 1mV peak voltage and 5 second of integration and settling time).

Sensor Id	Temperature (C˚)	V_{PM} (V)	Res. Freq. (Hz)	Gain (dB)	Q_R
Design-5	-25	10	12887	35.8	103,097
Design-5	-15	10	12872	33.7	93,621
Design-5	-3	10	12862	33.4	171,503
Design-5	0	10	12855	34.1	93,491
Design-5	20	10	12830	34.9	102,642
Design-5	40	10	12814	35.2	170,862
Design-5	53	10	12799	35.8	341,306
Design-5	60	10	12787	36.1	204,599
Design-5	70	10	12767	37.7	340,456
Design-5	80	10	12751	32.8	255,020
Design-5	90	10	12725	36.0	339,349
Design-5	100	10	12705	34.3	203,288
Design-5	110	10	12688	34.7	253,763
Design-5	120	10	12671	37.1	144,820

The TCF values are found by averaging each two points' TCF value and this was a bit wrong. That is why; a line is fit and found the correct TCF values which can be found in Figure 5.10. As it can be easily analyzed the slope of the hot plate is -1.1641 (Hz/˚C) and the slope of the Tenney oven is -1.4603 (Hz/˚C). At room temperature the resonance frequency of the resonator is 12.830 kHz. If each slope is divided to this resonance frequency and then multiplied with 10^6; the TCF values in ppm/K is obtained. For these tests average TCF value is calculated on hot plate with narrow range as -128 ppm/K; and the average TCF value is calculated on Tenney with broader range as -114 ppm/K.

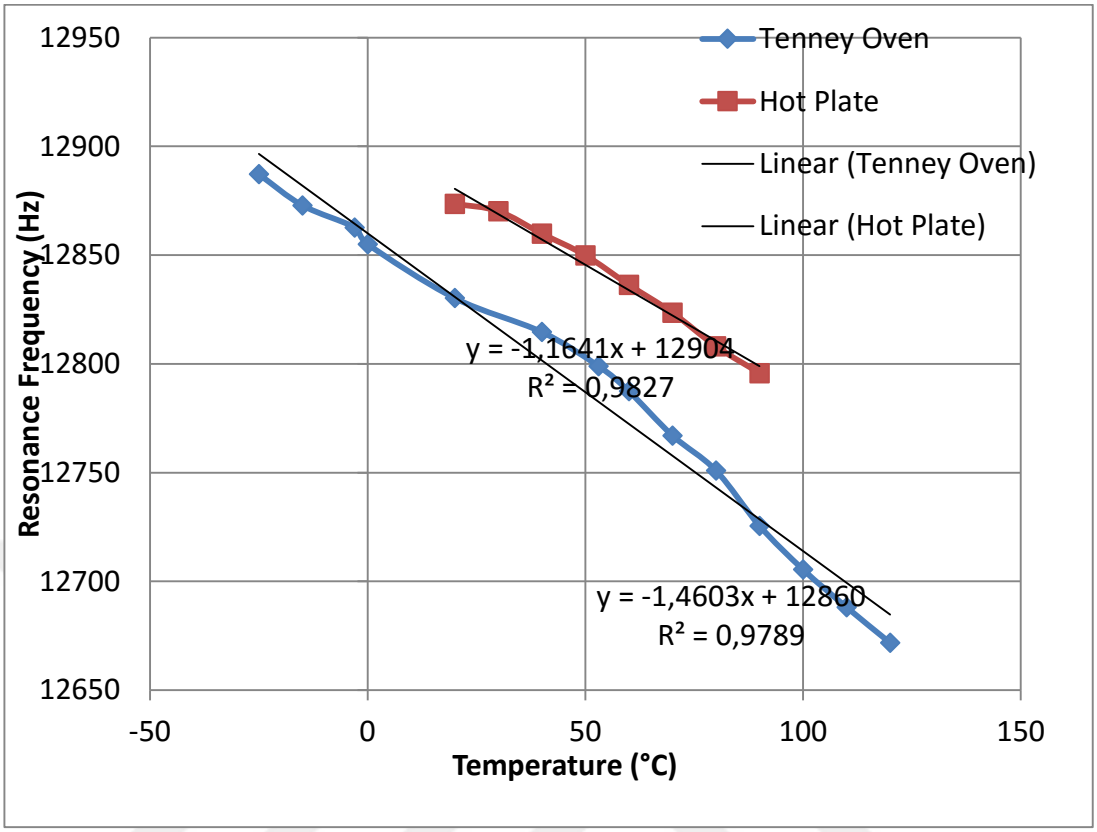

Figure 5.10: The resonance frequency versus temperature graph results of the Hot Plate and the Tenney Oven for resonator Design-5. For these tests average TCF value is calculated on the hot plate with narrow range as -128 ppm/K. The average TCF value is calculated on the Tenney with broader range as -114 ppm/K.

5.3.4 Closed Loop Temperature versus Controller Output Tests with Front End Electronics

The idea of this study is using the resonator structure as a temperature sensor together with controller circuitry. In other words, this thesis study consists of two branches; one is PI controller output which would be used as a temperature sensor and the other is preamplifier output which would generate carrier and that would be feed to the accelerometer readout circuitry.

After the open loop tests on Tenney oven are completed, the necessary wire bonding are done to convert the system to closed loop. Related with thesis study first of all,

from all different types of resonator sensors data are collected with the help of Data Acquisition (DAQ) Card in the temperature ranges from -20°C to +80°C. The DAQ board has two analog input channels which are used in different configurations for different tests. In this case, one input channel is used for collecting data from controller output whereas the other input channel is used for a commercial temperature sensor, TMP-36 for calibration purposes. Even though, it is known that this sensor does not provide the exact temperature of the sensor die, it is used to have an idea about the approximate temperature inside the package. The DAQ is picked and the necessary connections are set. The DAQ is preferred to sample data at 100 Hz for 2 hours and during this duration first the oven is cooled then heated and again cooled at the end to analyse hysteresis.

Note that the further tests are conducted only using Design-7 because its temperature and resonance characteristics are just as desired for the work in this thesis. The resonator test results of Design-7 for closed loop operation is presented as PI controller output versus temperature graphs prepared by using MATLAB Software. Figure 5.11 shows the test results of resonator Design-7. As can be analyzed from the figure the temperature sensitivity of the resonator Design-7 is 0.08 mV/°C. Similarly, Figure 5.12 represents the performance of the resonator Design-7 demonstrated with an ideal line fit.

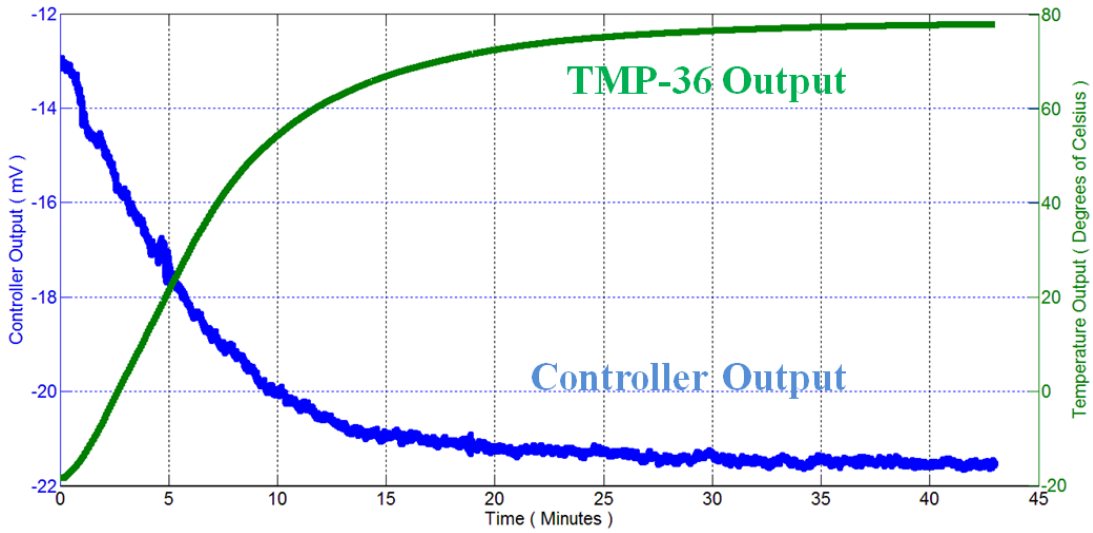

(a)

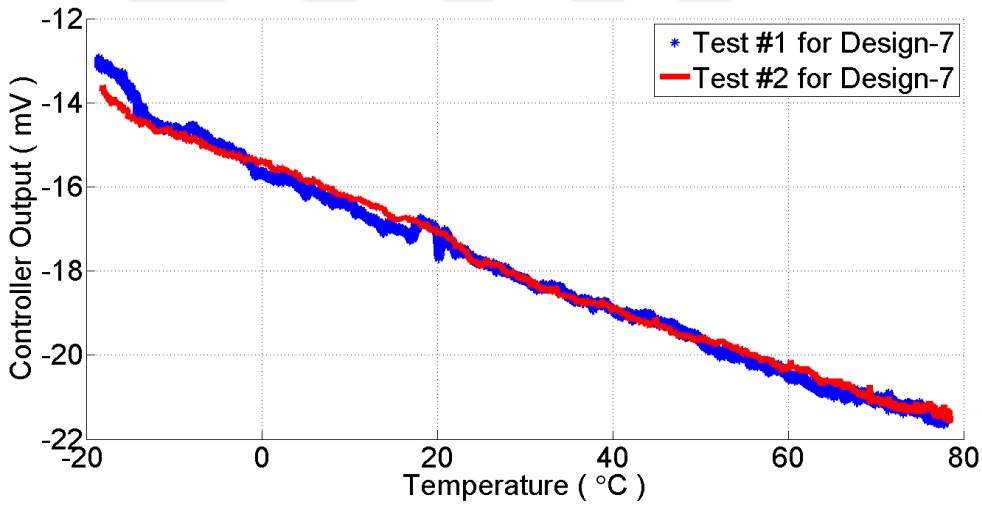

(b)

Figure 5.11: The test results of resonator package including Design-7 with its readout circuitry put into the Tenney Oven: (a) Design-7 resonator controller output and TMP-36 sensor output changes at the same plot for 45-minutes data collection; (b) Design-7 resonator controller output vs TMP36 sensors output results in the range minus 20°C to +80°C for different day tests with the same conditions.

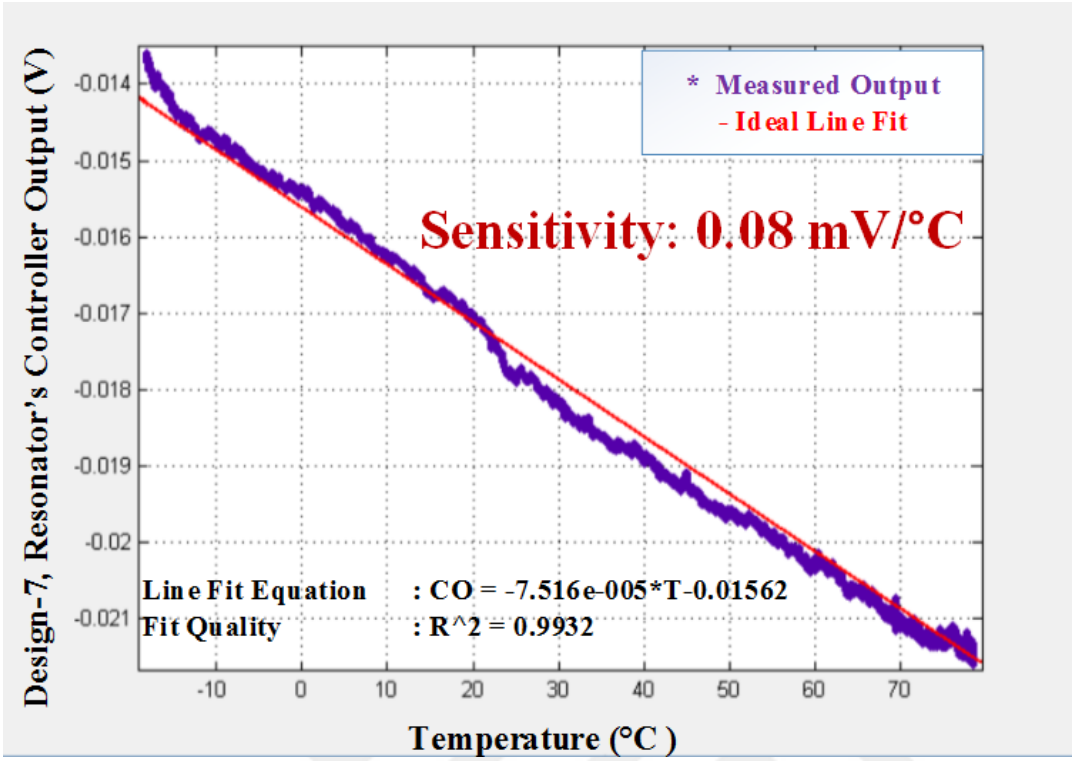

Figure 5.12: The performance of the resonator Design-7 with temperature range from -20°C to +80°C with an ideal line fit.

5.3.5 White Noise Calculation of Functional Resonator Packages

First of all, the data from the resonator packages are collected at 250 Hz for 5 minutes. Then, these data are processed for collecting the White noise and following Figure 5.13 shows one of the resonator design's Allan Variance analysis result. Table 5.4 shows the tabulated form of the scale factor, random walk and white noise of the functional resonator packages that is available.

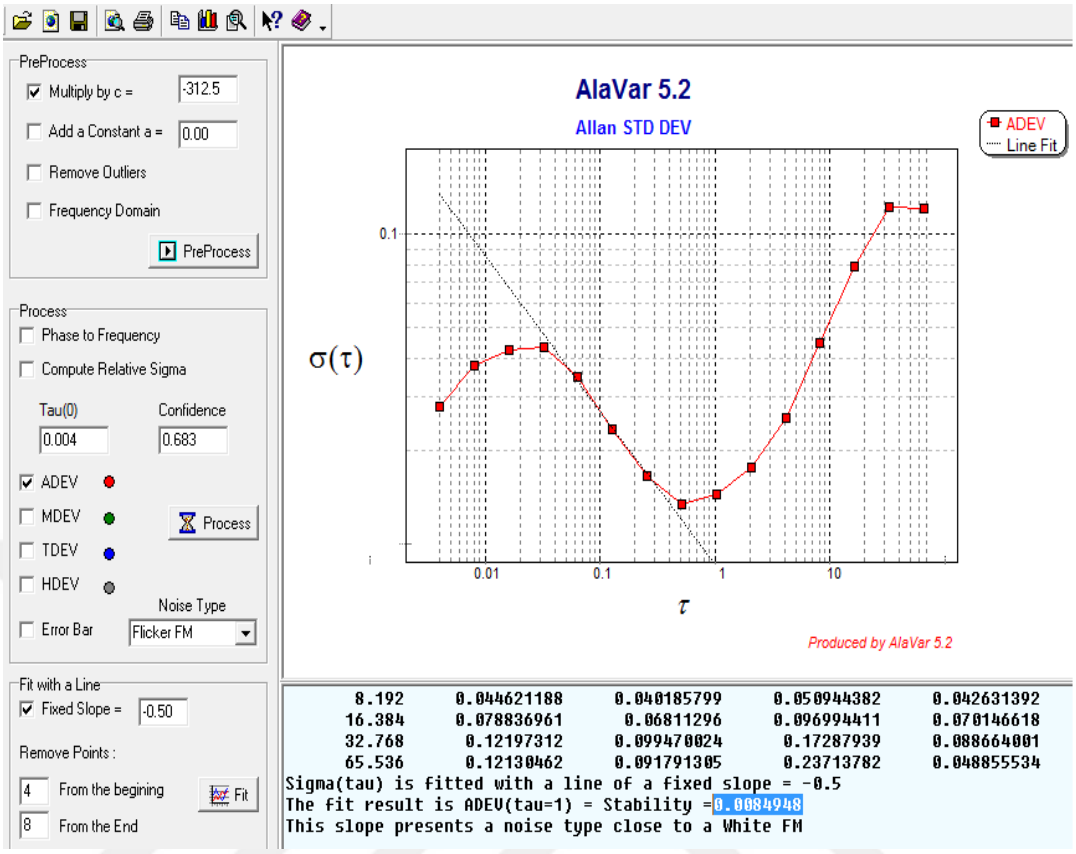

Figure 5.13: The sample Alavar output for Design-1; 15 kHz varying overlap type resonator sensors and these output is given for 75000 data collected from DAQ.

Table 5.4: The tabulated form of the functional sensors' scale factor, random walk and white noise values:

Sensor ID	Scale Factor (mV/°C)	Random Walk (°C/$\sqrt{Hz}$)	White Noise (°C/$\sqrt{Hz}$)
Design-1	-3.200	0.00849	12.00e-3
Design-3	-3.217	0.00044	6.14e-4
Design-6	-2.073	0.01181	16.50e-3
Design-7	-0.080	0.01015	14.20e-3
Design-8	-2.940	0.07528	105.39e-3

5.4 MEMS Accelerometer Sensor Used in the Study and Its Results

In the scope of this study period, various accelerometer types which are designed and fabricated at METU MEMS Research and Application Centre are investigated and at the end the accelerometer dies without a cap are eliminated because they are affected by the all possible environmental conditions like air, vibration and humidity.

Related with this thesis study single axis capped capacitive accelerometer sensor is preferred and in terms of sensor and readout circuitry they are designed at METU MEMS Research and Application Centre and it is significant to briefly define its characteristics. For convenience of this study single axis accelerometer is named as ACCE which has analog force-feedback readout circuitry designed by Yunus Terzioğlu, for the detailed information refer to [53], and Table 5.5 describes the basic specifications of this sensor.

Table 5.5: Features of the ACCE accelerometer sensor package.

Range	**±30 g**
Bias Instability	7 µg
Operating Range	-20 to +80 ˚C
Interface	Analog
Power Supply	12 V
Sampling Rate Accelerometer	125 Hz
Sampling Rate of Temperature	50 Hz
On-chip Temperature Sensor	Separate arrangement
Scale Factor	100mV/g
Offset	0.5 g
Dynamic Range	121 dB
Velocity Random Walk	37 µg/$\sqrt{Hz}$

5.4.1 Characterization of MEMS Accelerometer Sensor

For MEMS capacitive accelerometer sensor characterization C-V measurement tests are performed. C-V tests indicate how the capacitances of the electrodes of the accelerometer change with the applied DC voltages. Notice that C-V test results also give the idea about rest capacitance of the electrodes from which the parasitic capacitances can be estimated by comparing theoretical calculations with the C-V tests. Figure 5.14 represents the C-V measurement results of the single axis capped accelerometer sensor used for temperature compensation issue.

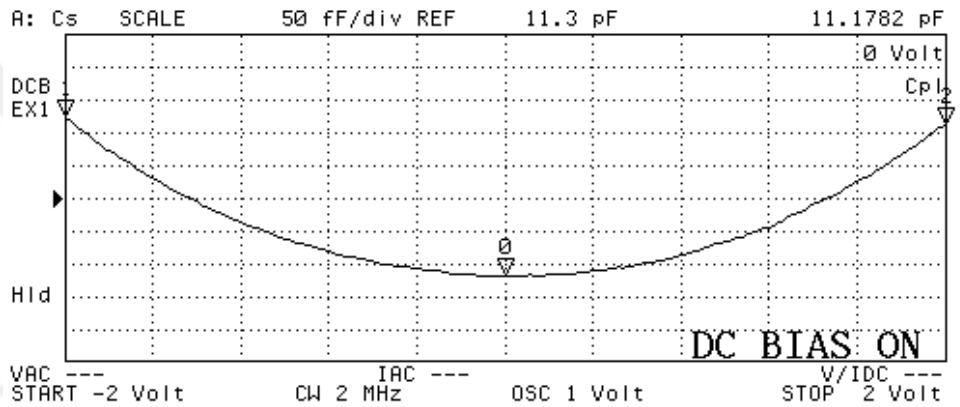

Marker	STIMULUS	VAL
0	0 Volt	11.1782 pF
1	-2 Volt	11.4219 pF
2	2 Volt	11.4095 pF

(a)

Figure 5.14: The C-V characterization results of ACCE sensor which is showing the functional responce: (a) The positive electrode measurement as it can be analyzed the smooth curve and parasitic capacitance of positive electrode (PE) is measured as 109.718 fF; (b)The negative electrode measurement as it can be analyzed from the smooth curve and changes are in logical manner and parasitic capacitance of negative electrode (NE) is measured as 49.795 fF.

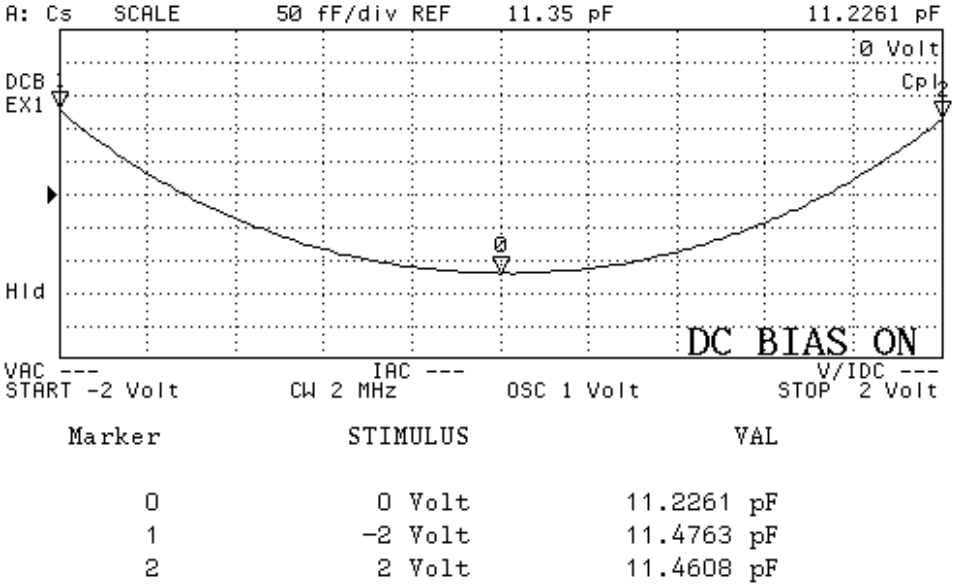

(b)

Figure 5.14: (continued)

Normally, it is expected to have a symmetric plot of capacitance change with respect to positive and negative DC voltages, a bit asymmetric plots are observed in Figure 5.14 and most probable reason for that are the charging effects of the glass substrate.

5.4.2 Hybrid-Package Preparation, Test PCB and Functionality Tests

The analog force-feedback readout circuit (AFFRO v1.2) introduced in [53], is used for the single axis MEMS accelerometer for this thesis study. For the detailed information about hybrid package and test PCB, the necessary references are given to [53].

Firstly, the accelerometer package is prepared (Figure 5.15) and after placing the packages to its convenient circuitry functionality tests are performed (Figure 5.16).

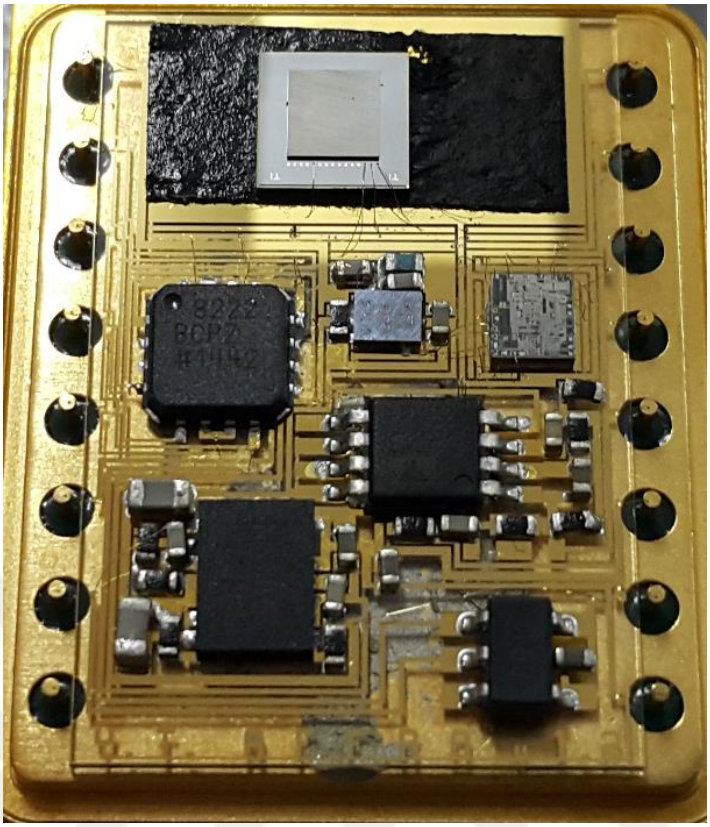

Figure 5.15: The final view of the prepared AFFRO v1.2 accelerometer package including ACCE sensor.

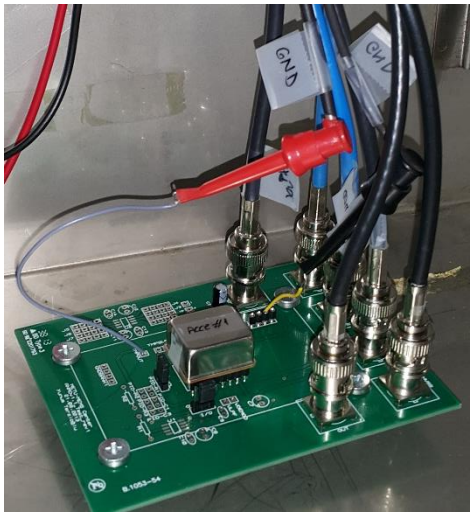

Figure 5.16: The ACCE single axis accelerometer sensor with the combination of AFFRO v1.2 readout circuitry to perform functionality tests.

5.4.3 Temperature Tests of Accelerometer Package

After being sure all the packages are functional temperature tests are started in Tenney Temperature Oven which is available in EE Department of METU. In tests, function generator is set to output a 20 kHz sinus at 5 Vpp amplitude. The power supply used in the tests has three outputs: +25, -25, and +6. These outputs are used in the following configuration: +6 Output: 3 V and 10 mA current limit; +25 Output: 12 V and 20 mA current limit; and -25 Outputs: -12 V and 20mA current limit. Figure 5.17 represents the temperature response of the packages in the range from -20°C to +80°C. In Figure 5.18 reliability of the accelerometer is tried to be shown by applying the temperature tests different days with the same conditions.

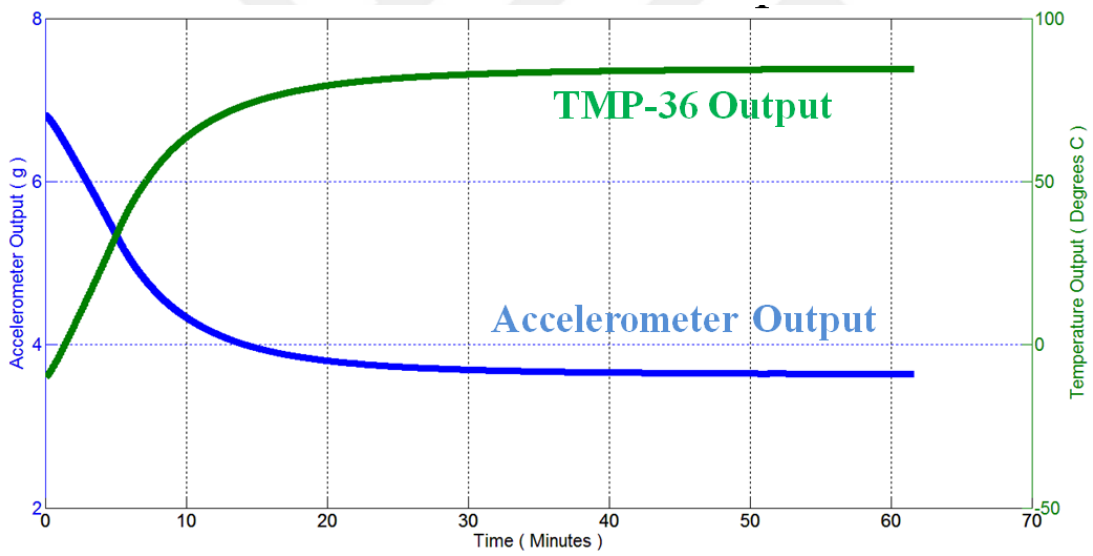

Figure 5.17: The ACCE single axis accelerometer sensor output results with temperature change from -20°C to +80°C for collected data set green color represents TMP36 temperature sensor output and blue color represents accelerometer output.

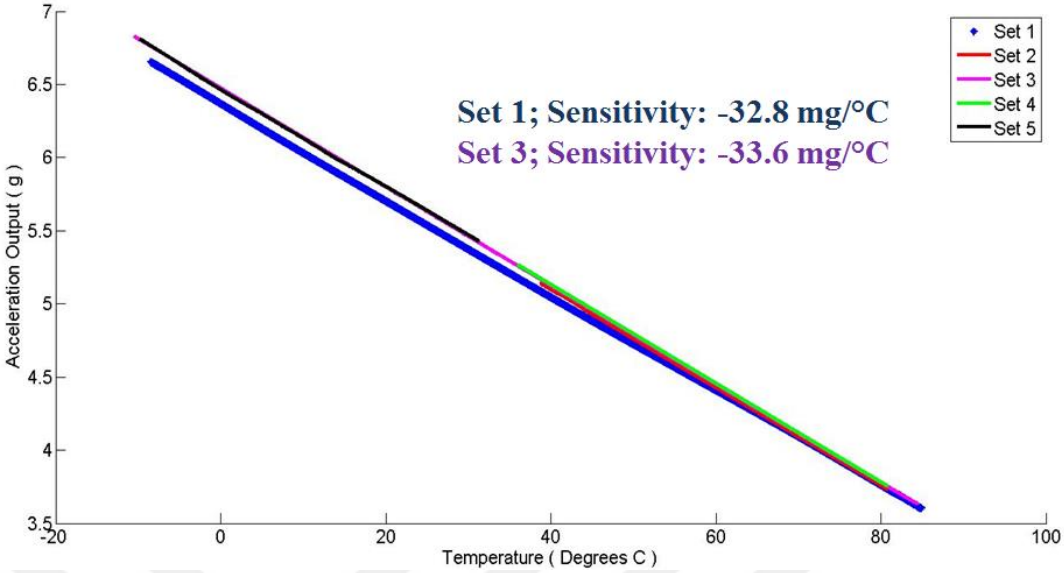

Figure 5.18: The ACCE single axis accelerometer sensor output results with temperature change for different test conditions. Set1 is detailed as from -20°C to +80°C with oven open; Set 2 is detailed as from +80°C to room temperature with oven closed; Set 3 is detailed as from -20°C to +80°C with oven open; Set 4 is detailed as from +80°C to room temperature with oven closed; and finally Set 5 is detailed as from -20°C to room temperature with oven closed.

For Set 1 temperature sensitivity is calculated as -32.8mg/°C and for set 3 temperature sensitivity is calculated as -33.6mg/°C. Similarly, sensitivity is -2.5 mV/°C (for 74mV/g scale factor). In conclusion repeatability is good in terms of temperature sensitivity.

Figure 5.19 represents the performance of the single axis MEMS capacitive accelerometer demonstrated with an ideal line fit.

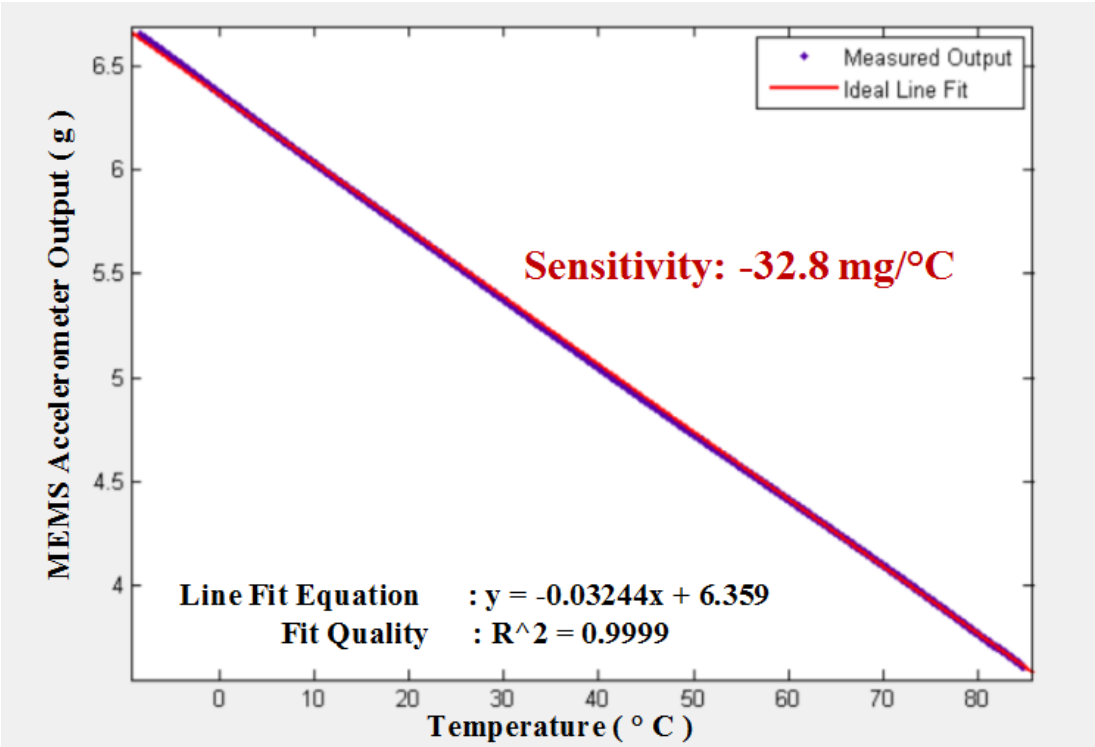

Figure 5.19: The performance of the accelerometer sensor with temperature range from -20°C to +80°C including an ideal line fit.

5.5 Implementation of Test Setup for the System Level Tests and Results

The testing procedure is similar to separate tests of resonator and accelerometer packages, first of all, related packages with their conventional readout circuitry is placed inside the Tenney oven; and the wires which contain the data come out of the hole which is placed left side of the oven and these wires are connected to the computers, power supplies and multimeters as shown in the Figure 5.20. Notice that for the resonator package testing procedure and used test equipment are same whereas for the accelerometer circuitry this time function generator is unnecessary because carrier is generated from the preamplifier output of the resonator package as shown in Figure 5.20-b.

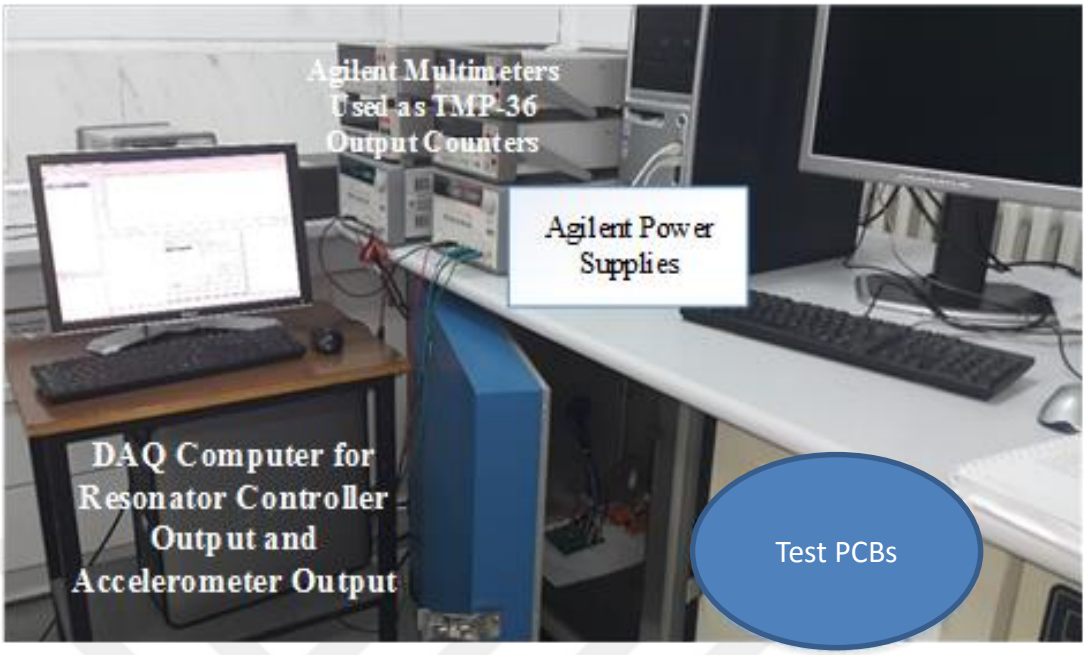

(a)

Figure 5.20: The image representing (a) The Tenney Oven in which the system level tests are conducted with data acquisition interface and control module for controlling the test conditions, (b) closure view of the placement of the MEMS sensors inside the chamber.

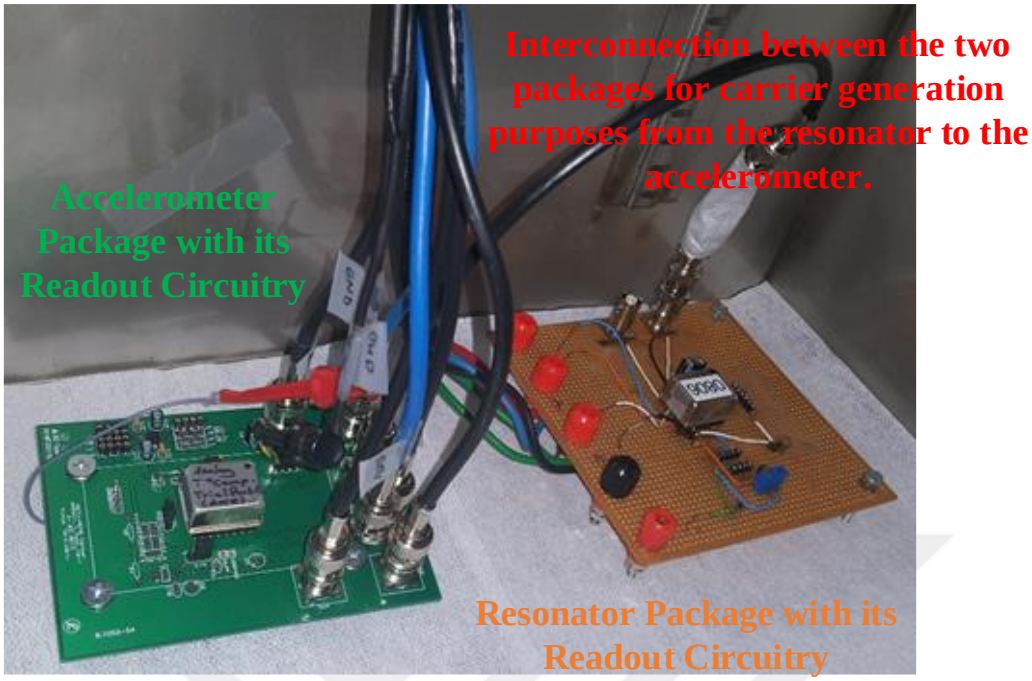

(b)

Figure 5.20: (continued)

5.5.1 Temperature Compensation of Accelerometer Output by Using Resonator's PI Controller Output Data

The temperature compensation of the accelerometer output is handled by using the resonator's controller output information in the same oven. Accelerometer and controller output data are processed in MATLAB Software where the collected data are imported. The detailed information is previously given in Section 5.2.

To sum up, the accelerometer output consists of acceleration, offset and temperature terms; and for this study temperature is expressed in terms of resonator's PI controller output. By removing the constants and after normalizing the accelerometer output value at room temperature; simplified compensation expression is obtained. Finally, by subtracting this simplified compensation equation from the raw accelerometer data compensated accelerometer data is found. Therefore, according to expressed methodology, the compensation is started with obtaining the relation between resonator controller output and accelerometer output (Figure 5.21). This relation is then normalized around the accelerometer output at room temperature. Final point is

using the normalized data in the accelerometer output compensation by either subtraction or addition. Figure 5.22 shows the compensated and uncompensated accelerometer data together with fitted line results.

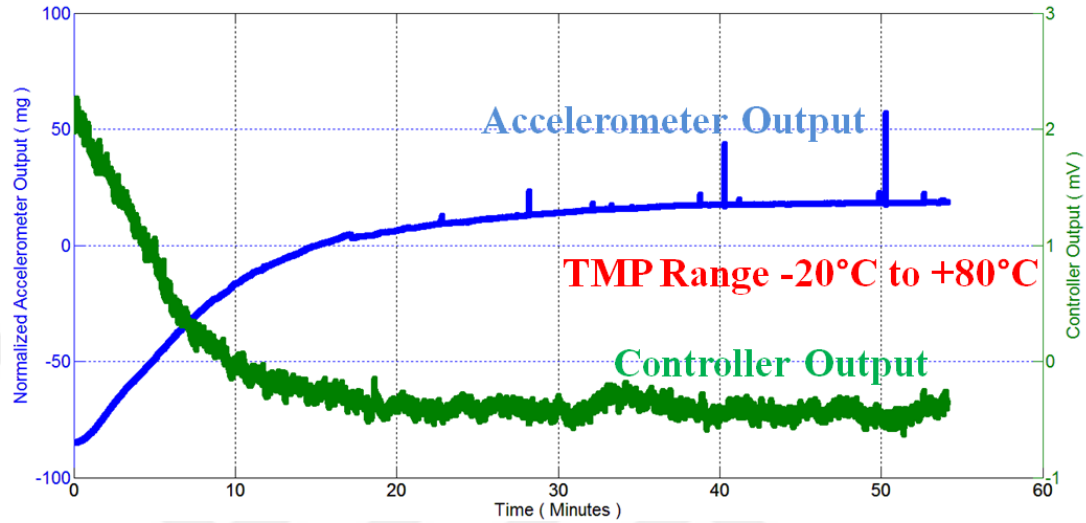

Figure 5.21: The relation between resonator controller output and accelerometer output including the test duration inside the temperature oven with the range -20°C to +80°C.

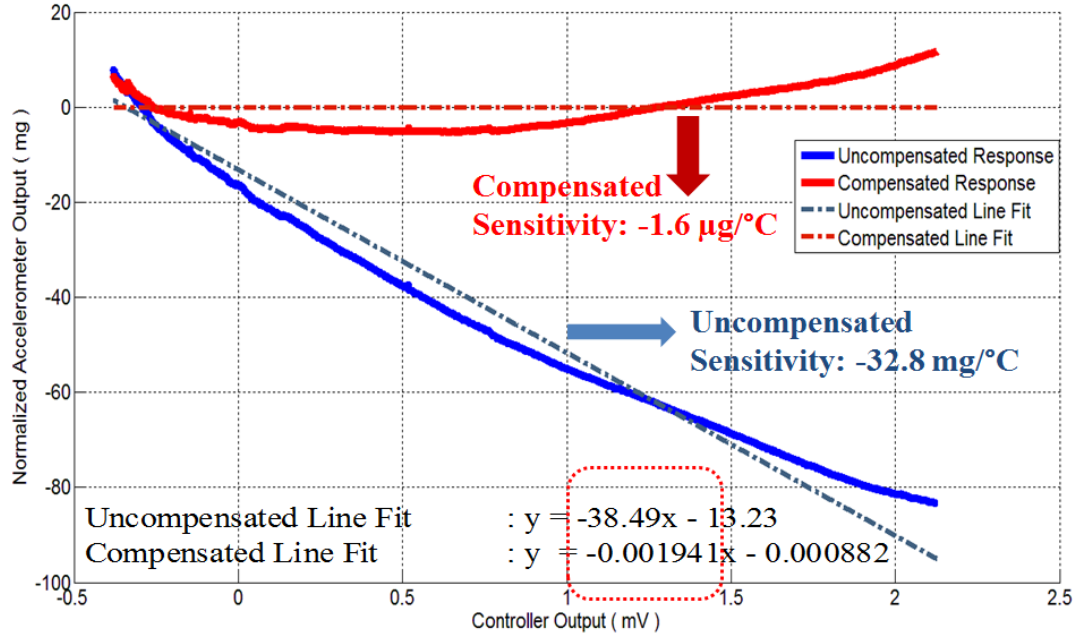

Figure 5.22: Temperature compensation plot of the MEMS accelerometer including both compensated and uncompensated outputs with line fit equations.

Note that a second or even third order curve fitting would result in a much more precise compensation work. However, since this work is ultimately intended for a real-time compensation practice, and this real-time compensation is intended to be based on a first order fit, the data processing was also conducted using a first order curve fitting.

Table 5.6 presents the comparison results of the accelerometer package feeding with resonator and feeding with function generator.

Table 5.6: The comparison results of the ACCE sensor obtained from two different tests in this study.

Accelerometer Package	**Together With Design-7 Resonator Package**	**Alone**
Interface	Analog	Analog
Scale Factor	100mV/g	100mV/g
Operating Range	Room Temperature	Room Temperature
Offset	0.5 g	0.5 g
Range	±30g	±30g
Velocity Random Walk	35 μg/$\sqrt{Hz}$	37 μg/$\sqrt{Hz}$
Bias Instability	16 μg	16 μg
Dynamic Range	122 dB	121 dB
Power Supply	12 V	12 V
Applied Resonance Frequency	12.25 kHz	12.25 kHz
Peak to peak voltage	1.46	1.46

The noise performance of the accelerometer presented in this study is also examined by collecting the output data under zero-g condition out of the temperature-controlled Tenney Oven for two conditions: carrier generation of accelerometer from function generator and carrier generation of accelerometer from the preamplifier output of the designed resonator sensor; respectively. The collected noise data are then processed by using the Alavar 5.2 software which utilizes the Allan Variance analysis for

determining the velocity random walk (VRW) and bias instability performances of the accelerometers. The obtained results can be examined in Allan deviation plots for two different conditions in Figure 5.23.

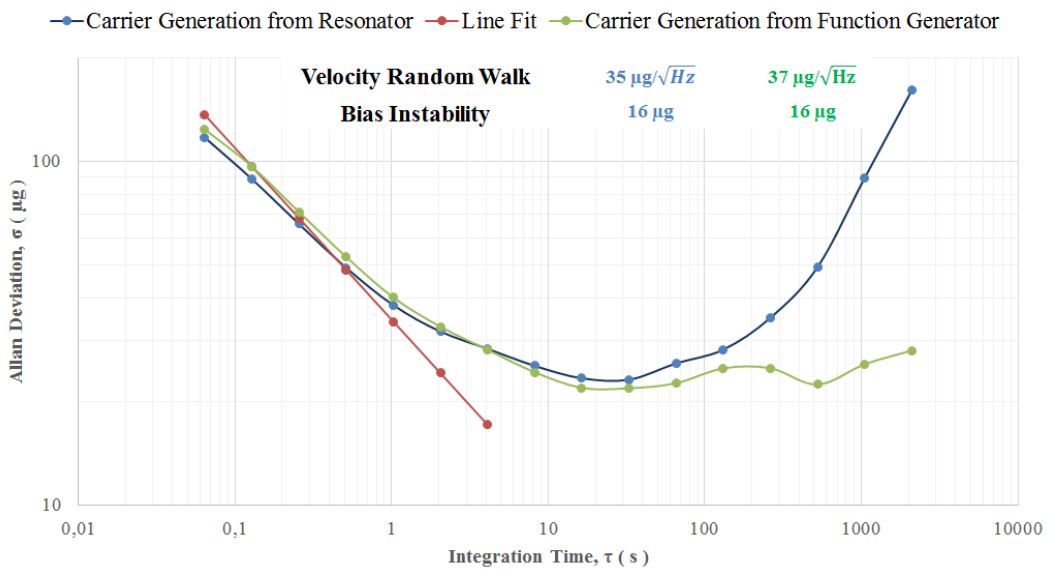

Figure 5.23: Allan deviation plots for the accelerometer used in the scope of thesis study.

5.6 Summary

At the beginning of this chapter, first of all, the detailed information of data collection procedures are analyzed. Then, the compensation of temperature and acceleration effects are investigated in detail. As a third step, the detailed test results of resonators ranging from functionality tests, resonance test, correction of open loop temperature versus resonance tests with front end electronics and TCF values to closed loop temperature versus controller output tests with front end electronics discussed. After that similar to resonators, the detailed test results of accelerometers are given. As a fifth step, the detailed test results of integration of resonator and accelerometer packages including raw and compensated results are given.

As it can be analyzed from Table 5.6 and Figure 5.23 if carrier generation of accelerometer package is from function generator it lasts more stable. Compared to alone case, together with resonator package performance is low. This may be caused

low bias stability of resonator package. Also drift, warm up and instability of resonator package is added to accelerometer package when together system level tests are performed. On the other hand, it can be seen that other parameters such as the scale factor or the velocity random walk are not affected dramatically by the addition of the resonator to the accelerometer. Thus, it can be concluded that using a MEMS resonator for the generation of a carrier signal for an accelerometer does not degrade any performance parameter of the accelerometer but the long term stability.

CHAPTER 6

CONCLUSIONS AND FUTURE WORK

The resonance-based MEMS temperature sensor for temperature compensation of MEMS capacitive accelerometer is presented in this thesis study. After giving the detailed information of compensation requirements, literature review, detailed problem review and why capacitive MEMS accelerometers is used; the detailed operation principles, mechanical design criterions and FEM simulations for proposed resonance-based MEMS temperature sensor is given in Chapter 2. Then, Chapter 3 summarizes the fabrication details while the design of controller electronics for MEMS resonators for the temperature compensation including the SIMULINK model and simulation results and describing the glass substrates which is designed to integrate the resonators with the readout electronics are mentioned in Chapter 4. Finally, the sensor characterization and system level integrated temperature tests are presented in Chapter 5. About the accomplishments and results of this research the following conclusions can be drawn:

- After analyzing the literature, to solve the drift error in MEMS capacitive accelerometers relied on experimental data rather than the theoretical error sources, resonance-based MEMS temperature sensors are proposed.
- The resonator theory in terms of dynamics are verified and the effects of electrostatic forces on mechanical structures including spring, mass, damping factor estimation, electrostatic actuation, and capacitive sensing are presented.
- The different types of micro-resonator designs developed in the scope of this study. Mainly two types of resonators are designed. First one is, single-mass H-shaped resonators which include two different actuation mechanism types called varying gap and varying overlap and each of these including resonance

frequency of 15 kHz and 45 kHz. Another one is tuning fork (double mass) resonator to obtain a high quality factor resonating structure. Similarly, in this type there were two different types of actuation mechanisms called varying gap and varying overlap and each of these including resonance frequencies of 15 kHz and 45 kHz. To sum up, in this thesis study there are totally 8 different types of designs.

- The verification of modal analysis is then carried out in finite element modelling (FEM) simulations for all different type of resonators by using CoventorWare Software.
- After the verification of designed micro-resonators with FEM simulations the implementation of single mass and tuning fork type resonators in the same die is performed.
- The fabrication details of proposed resonance-based temperature sensors is described with process flows; and fabrication results of the real devices are illustrated by SEM images.
- The readout electronics for micromechanical resonators studied in the scope of this thesis are proposed with schematics and the simulations in LT Spice environment. After the verification of the constructed SIMULINK model is functional and PI controller values are found properly; the glass substrate PCB layout is designed and fabricated for readout electronics of MEMS resonators at METU MEMS Center.
- After the integration of the resonator sensors and glass substrate PCB's the real time data acquisition from the resonator as temperature sensor is achieved as offered at the beginning of this study.
- In the scope of this study MEMS capacitive accelerometer sensor is used for compensation purposes with analog force-feedback readout circuitry and for the detailed information, the necessary references are given to [53].
- The resonator and accelerometer sensors characterized separately and their temperature dependencies are investigated. For resonators it is seen that tuning fork types show better performance compared with single mass ones. For accelerometer sensors capped ones show better performance compared with uncapped ones (Chapter 5 section 5.4); so packaging is a significant issue. In

test results part just the best ones for both resonators and accelerometers are given.

- The temperature look-up graphs are created to be able to express the temperature by the means of resonator's PI controller output voltage. This relation is given because of the fact that to be able to calculate the temperature for the associated controller output voltage.
- Then, the characterization and system level test procedures are introduced together with the preparation test setup. The temperature dependencies of the accelerometer outputs obtained from that tests. The temperature compensation is handled by using the controller output information of the resonance-based MEMS temperature sensor and also instead of function generator accelerometer sensor is fed by preamplifier output of the resonator package; so the scope of the thesis is verified successfully in both manners.
- The highlight of this work is the proof of the concept of using a MEMS resonator to generate a carrier signal for a capacitive MEMS accelerometer. The importance of this proof is that a resonator can be fabricated on the same chip with an accelerometer for an accurate reading of the accelerometer chip's temperature, and the resonator can be used to drive the accelerometer simultaneously.

The reported resonance-based MEMS temperature sensor for temperature compensation of MEMS capacitive accelerometer and feeding the accelerometer with self-oscillatory closed loop system instead of external sources are the major achievements in this study. The performance and applications of the system can be improved with further research as given below:

- The resonant sensor structure is made of silicon wafer whereas the glass substrate is used for metallization and connection purposes and anodic bonding applied between them. The material selection is significant on the performance of a resonance-based MEMS temperature sensor.

- The predrilled circuit board used in this thesis is the just prototype and sometimes it caused unexpected failures during the tests. For easier data

collection and improvement in data quality, a real test PCB can be designed, fabricated and used for further research on this topic.

- In the future applications proposed temperature sensor could be integrated with accelerometer or other sensors in the same die. By doing this temperature sensitivity could be improved.
- The minimum detectable temperature of micro-resonators presented in the scope of this study is dominated by the noise on the PI controller output voltage. The improvement on the noise signal will significantly improve the minimum detectable temperature achieved by the current topologies.
- The temperature compensation of the accelerometer output is handled by means of software by processing the acquired data from the resonator and accelerometer separately. The compensation can be adapted to closed-loop operation of the accelerometer as the future work to achieve the instant or real time temperature compensation of the accelerometer output.

REFERENCES

[1] M. G. Hak "The MEMS Handbook," CRC Press. 2002.

[2] S. Tez "A Three Axis Capacitive MEMS Accelerometer on a Multi-Stack Substrate," *Ph. D. Dissertation, Middle East Technical University,* January, 2014.

[3] R. Bogue, "MEMS Sensors: Past, Present and Future," *Sensor Review*, Vol. 27, no.1, pp. 7-13, 2007.

[4] S. Y. Yurish, N.V. Kirianaki, I. L. Myshkin, "World Sensors and MEMS Market: Analysis and Trends," *Sensors and Transducers Magazine*, Vol. 62, no. 12, pp. 456-461, December 2005.

[5] Yunhan Huang, Arind Sai Sarathi Vasan, Ravi Doraiswami, Michael Osterman and Michael Petch, "MEMS Reliability Review," *IEEE Transactions on Device and Materials Reliability*, Vol. 12, no. 2, pp. 482-492, June 2012.

[6] http://www.eetimes.com/document.asp?doc_id=1320035 [Last visited on January 2015.]

[7] M. Ali "Correction of Temperature and Acceleration Effects on MEMS Gyro Output Signals," *M.S. Thesis, Middle East Technical University,* December, 2014.

[8] Patrick L. Walter, "The History of MEMS Accelerometer: 1920s-1996 – Prolouqe and Epiloque," *Sound and Vibration, Acoustical Publications*, Inc., 2007.

[9] Terahz, http://terahz.org/_html/22SensorChronology.html, [Last visited on January 2014.]

[10] N. Yazdi, F. Ayazi, K. Najafi, "Micromachined Inertial Sensors," *Proceedings of the IEEE*, Vol. 86, no.8, pp. 1640-1659, August 1998.

[11] A. Walther, C. Le Blanc, N. Delorme, Y. Deimerly, R. Anciant, and J. Willemin, "Bias Contributions in a MEMS Tuning Fork Gyroscope," *Journal of Microelectromechanical Systems*, vol. 22, no. 2, pp. 303-308, April 2013.

[12] X. Wu, L. Duan and W. Chen, "A Kalman filter approach based on random drift data of Fiber Optic Gyro," *6th IEEE Conference on Industrial Electronics and Applications (ICIEA)*, pp. 1933–1937, June 2011.

[13] D. Xia, S. Chen, S. Wang, and H. Li, "Microgyroscope temperature effects and compensation-control methods," *International Journal of Sensors 9,* no. 10, pp. 8349-8376, 2009.

[14] V. Kaajakari, "Theory and analysis of MEMS resonators," *Validation Technologies Incorporateed,* 2011. *http://www.ieee-uffc.org/frequency-control/learning/pdf/kaajakari-MEMSResonators v2b.pdf* [Last visited on July 2015.]

[15] S. Feng, G. Quifen, G. Yuansheng, and L. Junshan, "Research on Thermal Characteristic in Slow- Small Temperature Changing for MEMS Linear Vibration Gyroscope," *Proceedings of 2006 IEEE Conference on Mechatronics and Automation,* pp. 475-479, June 2006.

[16] M. A. Hopcroft, B. Kim, S. Chandorkar, R. Melamuıd, M. Agarwal, C. M. Jha, G. Bahl, J. Salvia, H. Mehta, H. K. Lee, R. N. Candler, and T. W. Kenny, "Using the temperature dependence of resonator quality factor as a thermometer," *Applied Physics Letters,* 2007.

[17] "Theory and Analysis of MEMS Resonators," *VTI Technologies.*

[18] G. Stemme, "Resonant silicon sensors," *Micromech. Microeng.,*1990.

[19] K. Ren, M. B. Pisani, P. Kao, and S. Tadigadapa, "Micromachined Quartz Resonator Based High Performance Thermal Sensors," *IEEE,* 2010.

[20] J. H. Seo, K. S. Demirci, A. Byun, S. Truax, and O. Brand, " Temperature compensation method for resonant microsensors based on a controlled stiffness modulation," *Applied Physics,* 2008.

[21] C. Zhang, Q. Wu, T. Yin and H. Yang, "A MEMS gyroscope readout circuit with temperature compensation," *5th IEEE International Conference on Nano/Micro Engineered and Molecular Systems (NEMS),* pp. 458-462, January 2010.

[22] S. S. Schodowski, "Resonator Self-Temperature_sensing Using A Dal-Harmonic_mode Crystal Oscillator," *43rd Annual Symposium on Frequency Control,* 1989.

[23] A. Duwel, M. Weinstein, J. Gorman, J. Borenstein, and P. Ward, "Quality Factors of MEMS Gyros and the Role of the Thermoelastic Damping," *IEEE,* 2002.

[24] S. Humad, R. Abdolvand, G. K. Ho, G. Piazza; and F. Ayazi, "High Frequency Micromechanical Piezo-on_Silicon Block Resonators," *IEEE,* 2003.

[25] T. Yin, H. Wu, Q. Wu, H. Yang, "A TIA-based readout circuit with temperature compensation for MEMS capacitive gyroscope," *IEEE International Conference on Nano/Micro Engineered and Molecular Systems (NEMS),* pp. 401-405, February 2011.

[26] H. Sun, K. Jia, X. Liu, G. Yan, Y. Hsu, R. M. Fox, and H. Xie, "A CMOS-MEMS Gyroscope Interface Circuit Design with High Gain and Low temperature Dependence," *IEEE International Sensors Journal,* vol. 11, no. 11, pp. 2740-2748, November 2011.

[27] I. P. Prinkhodko, A. A. Trusov and A. M. Shkel, "Compensation of drifts in high-Q MEMS gyroscopes using temperature self-sensing," *Sensors and Actuators A: Physical 201,* pp. 517-524, 2013.

[28] S-R. Chiu, C-Y. Sue, C-H. Lin, L-T. Teng, L-P. Liao, Y-W. Hsu and Y-K. Su, "Active thermal compensation of MEMS based gyroscope," *2012 IEEE Sensors,* pp. 1-4, October 2012.

[29] X. Ji, S. Wang, Y. Xu, Q. Shi, and D. Xia, "Application of the Digital Signal Procession in the MEMS Gyroscope De-drift," *1st IEEE International Conference on Nano/Micro Engineered and Molecular Systems, NEMS'06,* pp. 218-221, January 2006.

[30] I. P. Prinkhodko, S. A. Zotov, A. A. Trusov and A. M. Shkel, "Thermal Calibration of Silicon MEMS Gyroscopes," *IMAPS International Conference* and *Exhibition on MEMS packaging,* Fountain Hills AZ US, March 2012.

[31] J. K. Bekkeng, "Calibration of a Novel MEMS Inertial Reference Unit," *IEEE Transaction and Instrumentation and Measurement,* vol. 58, no. 6, pp. 1967-1974, June 2009.

[32] C. Patel, P. McCluskey and D. Lemus, "Performance and reliability of MEMS gyroscopes at high temperatures," *12th IEEE Intersociety Conference on Thermal and Thermomechanical Phenomena in Electronic Systems (ITherm),* pp.1-5, June 2010

[33] J. K. Shiau, C. X. Huang, and M. Y. Chang, "Noise characteristics of MEMS gyro's null drift and temperature compensation," *Journal of Applied Science and Engineering,* vol. 15, no. 3, pp. 239-246, 2012.

[34] Q. Zhang, Z. Tan and L. Guo, "Compensation of Temperature Drift of MEMS Gyroscope Using BP Neural Network," *International Conference on Information Engineering and Computer Science, ICIECS 2009,* pp. 1-4, December 2009.

[35] K. Wang, L. Yong and R. Chris, “The effect of the temperature-correlated error of inertial MEMS sensors on the integration of GPS/INS,” *Proceedings of International Global Navigational Satellite Systems (IGNSS 2009) Symposium,* 2009.

[36] D. Keymeulen, C. Peay, K. Yee, and D.L. Li, “Effect of Temperature on MEMS Vibratory Rate Gyroscope," *IEEE Aerospace Conference,* pp. 1-6, March 2005.

[37] K. Shcheglov, C. Evans, R. Gutierrez and T. K. Tang, “Temperature dependent characteristics of the JPL silicon MEMS gyroscope,” *IEEE Aerospace Conference Proceedings,* vol. 1, pp. 403-411, 2000.

[38] S. E. Alper, “MEMS Gyroscopes of Tactical Grade Inertial Measurement Applications,” *Ph.D. Thesis, Middle East Technical University,* September 2005.

[39] I. E. Ocak, “A Tactical Grade MEMS Accelerometer,” *Ph. D. Dissertation, Middle East Technical University,* September 2010.

[40] M. M. Torunbalci, “Development of New, Simple, and Robust Wafer Level Hermetic Packaging Methods for MEMS Sensors,” *Ph.D. Thesis, Middle East Technical University,* February, 2016.

[41] S. E. Alper, M. M. Torunbalci, and T. Akin, “Method of wafer level hermetic packaging with vertical feedthroughs”, PCT/TR2013/000298, September, 2013.

[42] M. M. Torunbalci, E. Tatar, S.E. Alper, and T. Akin, “Comparison of two alternative silicon-on-glass microfabrication processes for MEMS inertial sensors,” Proc. Eurosensors XXV, pp. 900–903, September, 2013.

[43] E. Tatar, M. M. Torunbalci, S.E. Alper, and T. Akin, “A method and electrical model for the anodic bonding of SOI and glass wafers,” IEEE MEMS’12, pp.68-71, January, 2012.

[44] M. M. Torunbalci, S. E. Alper, and T. Akin, “A Method of Fabricating Vacuum Packages with Vertical Feedthroughs in a Wafer Level Anodic Bonding Process,” Eurosensors XXVIII, pp. 887-890, Brescia, Italy, September 2014.

[45] M. M. Torunbalci, S. E. Alper, and T. Akin, “Wafer Level Hermetic Sealing of MEMS Devices with Vertical Feedthroughs using Anodic Bonding,” Sensors and Actuators A, Vol. 224, pp. 169-176, April 2015.

[46] M. M. Torunbalci, S. E. Alper, and T. Akin, “Wafer Level Hermetic Encapsulation of MEMS Inertial Sensors using SOI Cap Wafers with Vertical Feedthroughs,” IEEE Int. Symposium on Inertial Sensors and Systems (ISISS’14), pp. 1-2, Laguna Beach, California, USA, February 2014.

[47] M. M. Torunbalci, S. E. Alper, and T. Akin, “Advanced MEMS (aMEMS) Process for Wafer Level Hermetic Encapsulation of MEMS Devices using SOI Cap Wafers with Vertical Feedthroughs,” IEEE/ASME Journal of Microelectromechanical Systems, Vol. 24, pp. 556-564, March, 2015.

[48] M. M. Torunbalci, E. C. Demir, I. Donmez, S. E. Alper, and T. Akin, “Gold-Tin Eutectic Bonding for Hermetic Packaging of MEMS Devices with Vertical Feedthroughs,” IEEE Sensors 2014, pp. 2187-2190, Valencia, Spain, November 2014.

[49] Mark W. Weber, Robert B. Smith, “Quadrature Reduction in MEMS Gyro Devices Using Quad Steering Voltages,” *US Patent*, 7213458 B2, May 8, 2007.

[50] H. D. Gavcar “Compensation Methods for Quasi-Static Acceleration Sensitivity of MEMS Gyroscopes,” *M.S. Thesis, Middle East Technical University*, October, 2014.

[51] Y. Temiz, “Advanced Readout and Control Electronics for MEMS Gyroscopes,” *M.S. Thesis, Middle East Technical University*, August 2007.

[52] B. Eminoğlu, “Control Electronics for MEMS Gyroscopes and its Implementation in a CMOS Technology,” *M.S. Thesis, Middle East Technical University*, February 2011.

[53] Y. Terzioğlu, “A High Performance Closed-Loop Analog Readout Circuit for Capacitive MEMS Accelerometers,” *M.S. Thesis, Middle East Technical University*, September 2015.

[54] M. A. Hopcroft, “Temperature-Stabilized Silicon Resonators for Frequency References,” *Ph.D. Thesis, Stanford University*, September 2007.